5-2006

Analysis of tensioner induced coupling in serpentine belt drive systems

Ryan Neward

ANALYSIS OF TENSIONER INDUCED COUPLING IN SERPENTINE BELT DRIVE SYSTEMS

By

RYAN NEWARD

A Thesis Submitted in Partial Fulfillment of the Requirements for the Degree of

MASTER OF SCIENCE
IN
MECHANICAL ENGINEERING

Approved by:

Dr. Stephen Boedo
Department of Mechanical Engineering
Stephen Boedo
(Thesis Advisor)

Dr. Agamemnon Crassidis
Department of Mechanical Engineering
Agamemnon Crassidis

Dr. Kevin Kochersberger
Department of Mechanical Engineering
Kevin Kochersberger

Dr. Edward Hensel
Department Head of Mechanical Engineering
Edward Hensel

DEPARTMENT OF MECHANICAL ENGINEERING
ROCHESTER INSTITUTE OF TECHNOLOGY
MAY 2006

ANALYSIS OF TENSIONER INDUCED COUPLING IN SERPENTINE BELT DRIVE SYSTEMS

I, Ryan Neward, hereby grant permission to the Wallace Library of Rochester Institute of Technology to reproduce my thesis in whole or part. Any reproduction will not be for commercial use or profit.

Ryan Neward

Ryan Neward
May 2006

Acknowledgements

I would like to thank my faculty advisor Dr. Stephen Boedo for allowing me the opportunity to work with him in a field so close to my interests. His guidance and support have been critical to my success throughout my research and writing. I express my thanks to my committee members Dr. Agamemnon Crassidis and Dr. Kevin Kochersberger for taking the time to review my thesis. Their inputs have contributed greatly to the strength of my results.

My sincere gratitude goes out to all those at LMS CADSI who initially supported my research and provided me the opportunity to learn their software. Despite the change in direction of my research, the motivation for my work was derived from their interest in the field. In addition, the skills I learned through working with their software were valuable to my understanding of belt drive systems. I would especially like to thank Joe Zamora, at LMS CADSI, for all of his time and effort in helping me understand the software.

My appreciation goes out to Dr. Robert Parker at Ohio State University for his correspondence and support of my work. His extensive list of papers was invaluable in my research. I thank the Mechanical Engineering Department faculty and staff, especially Mrs. Selleck, for all of their help in my engineering studies.

I would like to express my deepest appreciation to my parents. Without their support (both financial and motivational) this thesis would have never had a chance of success. In addition, my brother and sister deserve special thanks; as they provided a few needed breaks from my research. I am glad to be able to thank the special woman in my life, Erin, for it was her support that made all the long days worth while.

Finally, I would like to dedicate my thesis to all the people mentioned above; without their help this thesis would never have been completed as it is today.

Abstract

Serpentine belt drive systems are widely used in automobiles due to their compactness and long life. These systems are composed of a belt, a driving pulley, driven pulleys, and a spring-loaded tensioner. The driven pulleys may include such accessories as the alternator, air conditioner, or power steering pump. Serpentine belt drives experience many different types of steady state motions and transient vibrations due to the different parameters in the system. As a result of this, it is important to create a mathematical model that allows the designer to extract information about the system such as the natural frequency and the mode shapes. The accuracy of the model will depend primarily on the assumptions used. In particular, a key assumption is whether transverse and rotational motions of the belt are coupled due to the motion of the automatic belt tensioner. This coupling is often neglected by authors who model only longitudinal belt response and in effect decouple the transverse and rotational motions. Using a solution based upon coupled motion as well as a solution employing rotational motion only, the importance of this coupling will be assessed. Both solution results will be compared against published experimental data. In addition, a parametric study will be performed to determine the ability of the coupled and decoupled models to accurately predict changes in system natural frequencies and mode shapes due to changes in system parameters.

Contents

List of Figures

List of Tables

Nomenclature

c	Propagation speed of transverse waves relative to the belt
C_t	Damping of the tensioner arm about the tensioner arm pivot
EA	Longitudinal belt stiffness
g	Gravitational acceleration
J_j	Moment of inertia of the j^{th} pulley
J_t	Moment of inertia of the tensioner arm (decoupled analysis); Moment of inertia of the tensioner assembly (coupled analysis)
$J_{\gamma t}$	Moment of inertia of the tensioner pulley about the tensioner arm pivot
K_j	Stiffness of the j^{th} belt span
K_{pj}	Belt stiffness around the contact arc of the j^{th} pulley
K_t	Rotational spring stiffness of the tensioner spring
$K.E.$	Kinetic energy
L_{belt}	Length of the entire belt; $L_{belt} = \sum L_j + R_j \phi_j$
L_{eff}	Distance between tensioner arm pivot and the mass center of the tensioner arm and pulley
L_j	Length of the j^{th} belt span
L_t	Length of the tensioner arm
m_{eff}	Total mass of tensioner arm and pulley
P_c	Centrifugal tension
P_j	Tension in the j^{th} belt span
P_0	Initial static tension at zero operating speed and zero accessory torques
P_{rj}	Reference tension in the j^{th} belt span
P_{tj}	Tractive tension
Q_j	Steady accessory torque on the j^{th} pulley

Q_t	Initial torque on the tensioner arm
R_j	Radius of the j^{th} pulley
RPM	Crankshaft rotations per minute
$S.E.$	Strain energy
t	Time
V	Steady belt speed
$W_j(X,T)$	Transverse displacement of the j^{th} belt span
(X_j, Y_j)	j^{th} pulley center location
x_s	Coordinate along span length
α_r, γ_r	Non-dimensional basis functions
$\beta_{1,2}$	Orientation angle of belt (see Fig. 2.3); $\beta_{1,2} = \theta_t - \zeta_{1,2}$
Δ_j	Belt deflection in the longitudinal direction
δ_j	Belt laid out during stretching along the j^{th} contact arc
δ_{rs}	Kronecker delta
ε	Small perturbation form equilibrium
$\zeta_{1,2}$	Belt span inclination angle from the horizontal to the exterior of the belt (see Fig. 2.3)
η	Pulley support constant
Θ_j	Absolute rotation of the j^{th} pulley; $\Theta_j = \omega_j t + \theta_j$
θ_j	Phase angle of the j^{th} pulley
θ_t	Tensioner arm angle
θ_0	Installed angular position of the tensioner arm
κ	$\kappa = 1 - \eta$
ρ	Belt mass per unit length
ϕ_j	Contact arc of the belt on the j^{th} pulley
ω_j	Angular velocity of the j^{th} pulley
ω_n	Natural frequency

CHAPTER 1

INTRODUCTION

A belt drive is used to transfer power from a driving pulley, powered by some external source such as an electric motor or internal combustion engine, to one or more driven pulleys. Belt drives are employed extensively by machine designers in such applications as power tools, vacuum cleaners, automobiles, or any other piece of powered rotating equipment. This chapter gives an introduction to the application of belt drives within an automotive front end accessory drive utilizing a V-ribbed belt to transfer power between the engine crankshaft and multiple accessory pulleys. Recent work that has been done to model belt drives and analyze these models will be reviewed in section 1.2. Goals and contributions of this thesis will be presented and described in section 1.3.

1.1 SERPENTINE BELT DRIVES

In recent times, front end accessory drive designers have evolved from utilizing a multiple V-belt setup to employing a single V-ribbed belt (poly-grooved belt). Such a system, shown in Figure 1.1, is known as serpentine belt drive due to the elaborate path it must follow to reach all of the accessory pulleys and provide a sufficient wrap angle. The advantages of using a serpentine belt drive setup over multiple V-belts include compactness, ease of belt replacement, length of belt life, and the ability to maintain strand tension using a single tensioner mechanism.

Serpentine belt drives consist of a driving pulley, driven pulleys, belt, and an automatic tensioner. The driving pulley is attached to the engine crankshaft which provides the torque necessary to drive the system. Typically, in front end accessory drive applications, the number of driven pulleys ranges from 2 to 6 and may power such components as the air conditioner compressor, water pump, alternator, and power steering pump. An idler pulley is often used simply as a "dummy" pulley to increase the wrap angle around adjacent pulleys experiencing high torque demands.

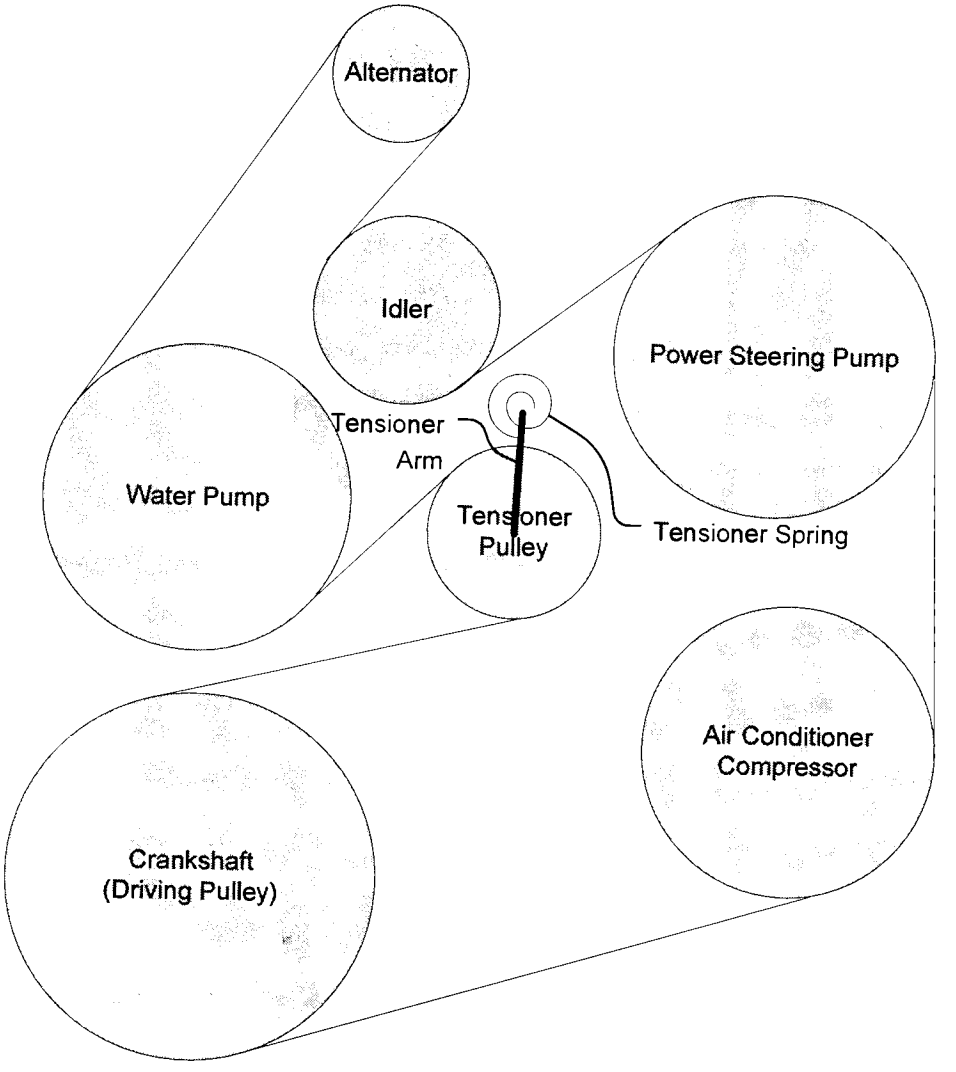

Figure 1.1 Serpentine belt drive system

Belts used within a serpentine drive are referred to as multi-rib belts, V-ribbed belt, or poly-grooved belt. They will be referred to as V-ribbed belts throughout the rest of this thesis. V-ribbed belts experience longer life compared to thicker cross section V-belts as a result of their smaller bending stiffness and reduced structural damping. Low bending stiffness and increased width allow these belts to transmit power using the back side, or flat side, of the belt. V-belts are unable to accommodate this task due to the fact that their increased thickness is not suitable for bending in both directions.

An automatic tensioner acts to maintain constant tractive tension throughout the entire belt drive system despite belt wear, assembly variation, and deviation in belt length due to changes in accessory torques, belt speed, and belt temperature. There exist two types of tensioner setups: pivot and slider. The pivot tensioner is composed of an idler pulley pinned to a rigid moment arm which pivots about a fixed point. At the pivot point, a coil spring and dry friction or viscous damper are attached to the rigid arm. The second arrangement for the tensioner is the slider type tensioner. This setup has the idler pulley slide within a straight groove. A linear spring and a dry friction or viscous damper are attached to the idler pulley. The effectiveness of the tensioner is dependent upon the design and integration into the belt drive system. Ideally, the tensioner should maintain constant tension in the two belt spans adjacent to it.

The core source of belt malfunction is vibrations within the system. There exist two different types of vibrations that a belt may experience. The first type is referred to as rotational vibration (some authors may refer to this as torsional vibration, but this is an incorrect label as torsional motion is taken to be belt twist about an axis pointing in the direction of belt travel). Rotational vibration occurs when the pulleys oscillate about their spin axes and in turn induce longitudinal belt deformations. In this case, the belt acts as an axial spring between the pulleys. The second type of vibration is referred to as transverse vibration which is the motion of the belt normal to belt travel. This is generated by the motion of the tensioner or the rotational vibration of the system.

Belt vibrations can be the result of variation in the applied torque at the crankshaft due to the ignition cycle of the engine, torque from the pulleys, pulley eccentricities, irregular belt properties, or motion of the pulley supports. Dynamic stresses in the belt as a result of vibrations are detrimental to the effective operation of the belt drive as they may cause premature wear and may lead to loss of sufficient tension. Rotational vibrations also create dynamic stresses in the bearings which lead to bearing fatigue and noise. Belt slip around the pulley takes place when the tension drop across a pulley exceeds the friction force between the pulley and the belt. As the belt creeps against the pulley during tension transitions, the belt will experience early wear.

1.2 LITERATURE REVIEW

The basis for the work that has been done in the field of serpentine belt drives is research on the vibration characteristics of axially moving material. Mote [1] formulated a procedure to determine band saw natural frequencies. He found that the natural frequencies decrease from a maximum at zero velocity at a rate which depends upon the band pulley axis relative motion. If the axes are fixed, the natural frequency decreases most rapidly with increasing velocity. However if the axis are allowed to move relative to each other thereby allowing the band to extend, the natural frequency decreases less rapidly with increasing velocity. In a later work, Mote and Wickert [2] presented an additional method of modeling axially moving continua in which the orthogonality properties of the gyroscopic system are used to simplify the formulation of the complex eigenfunctions.

Modeling and analyzing serpentine belt drive systems with a dynamic tensioner was first accomplished by Ulsoy et al. [3] in which they used a mathematical model to examine the transverse vibration and stability of coupled belt-tensioner systems. Experimental results were used to locate instability regions and to validate the numerical solutions of the mathematical models.

Gasper and Hawker [4] developed a system of governing equations for a serpentine belt drive system that include damping, accessory load variations, and fluctuations in input torque. Despite the absence of a dynamic tensioner, they introduced a solution technique that resulted in the eigenvalues and eigenvectors of the complete system, which was proven useful in future works.

Hawker [5] developed a mathematical model for the angular motion of an automotive accessory drive system including an automatic tensioner. He developed the model with the objective of determining the natural frequencies and mode shapes by using the approach of assuming harmonic motion and solving for the eigenvalues and eigenvectors. The forced responses and dynamic belt tension are found using superposition once the equations are put in linear form. Experimentation was used to validate the numerical results.

Barker et al. [6] developed a model for a complete serpentine belt drive system including a tensioner and multiple pulleys. The objectives of the model were to simulate the response of each pulley and belt span to known input motion of the crankshaft. In addition, simulations of various combinations of accessories being turned on or off are compared against experimental results. Experimental testing was used to define characteristics of the components which are then modeled using polynomial curve fitting and numerical solution of differential equations.

Hwang et al. [7] derived a nonlinear model that governs the longitudinal response of the belt spans in correlation with the rotational response of the crankshaft and accessory pulleys. Solution of the equilibrium equations leads to the tension-speed relationship for the serpentine belt drive system. The overall equations of motion are then linearized about the equilibrium state allowing the rotational mode characteristics to be obtained from the associated eigenvalue problem. Through integration of the nonlinear equations of motion, belt tension fluctuations are obtained that are used to predict the onset of belt slip around each accessory pulley.

Kraver et al. [8] extended the modal vibration analysis to include a viscous belt span and coulomb tensioner arm damping. It is claimed that the complex modal procedure provides a solution over a range of driver pulley frequencies at a speed of over 100 times faster than the 4^{th} order Runge-Kutta numerical integration method. In order to validate the model, results were compared against Hwang et al. [7] and found be in good agreement.

Using dry friction damping within their model, as opposed to the more commonly used viscous damping, Leamy and Perkins [9] were able to capture the primary and secondary resonances within the belt drive system. This was accomplished using an incremental harmonic balance method generalized for use with multi-degree of freedom linear subsystem coupled to a single degree of freedom nonlinear subsystem with Coulomb damping.

Balaji and Mockensturm [10] used a one-way clutch to mitigate tension fluctuations in the belt caused by the high inertia accessory pulleys. The system is modeled considering only longitudinal vibration of the belt spans and incorporates a decoupler and/or isolator within the high inertia accessory pulley. This model is linearized about the equilibrium configuration in both engaged and disengaged states to obtain analytical solutions. Numerical integration of the equation of motion is used to determine the effect of non-linear terms.

Previous works on serpentine belt drives have used linear strain measure to predict transient belt tensions. Schulz [11] instead used logarithmic strain measure to describe elastic creep. It was shown using numerical examples that the logarithmic strain measure provides more accurate results than the linear strain measure due to the condition for the existence of steady state motions with constant belt tensions, as a solution of the mass conservation law.

Nouri and Zu [12] described an approach for optimizing the design of the automatic tensioner within the belt drive system. Using sequential quadratic programming for the

multi-degree of freedom system and the Kuhn-Tucker method for the single-degree of freedom system, the authors were able to obtain the optimal design. The optimal design minimizes tension variation in the belt spans and pulley responses due to the harmonic excitation from the crankshaft.

All of the works mentioned previously assume that the linear response of belt drives is composed of the superposition of independent transverse and longitudinal modes. However, as shown by Beikmann [13], there exists a linear coupling between the transverse and rotational modes in the spans adjacent to the automatic tensioner. This linear coupling is created by the rotational degree of freedom of the tensioner arm. In addition, there exists a nonlinear coupling mechanism between rotational and transverse modes arising from the finite stretching of the belt. This coupling can become greatly magnified under conditions leading to internal or autoparametric resonance. Beikmann also introduced a tensioner support constant η which is an indicator of 1) the systems ability to maintain tractive tension (despite load and speed variations), and 2) stability of the reference equilibrium state.

Beikmann et al. [14] examined further the linear free response of serpentine belt drives involving coupling between the transverse and rotational modes. They provide an exact solution procedure to calculate the natural frequencies and mode shapes of a prototypical three pulley system which may be extended to any system with n number pulleys. In [15] Beikmann et al. examined the nonlinear coupling in the serpentine belt drive system. To obtain a low-order discrete model for nonlinear forced response a modal expansion is used which captures the two-way coupling between all mode-pairs. It is found that in the presence of 1:2 internal resonance, rotationally dominant modes generate dynamic tension fluctuation which may excite large transverse belt vibrations. This is due to the strong nonlinear mechanism that couples the rotational dominant (longitudinal belt) modes and transversely dominant modes. Beikmann et al. [16] continued work on serpentine belt drive systems by examining the effectiveness of the automatic tensioner. Using a closed form solution to the nonlinear equation, the key parameters are

determined which affect the tensioner performance as characterized by the tensioner constant η.

Zhang and Zu [17] used the prototypical three pulley model developed by Beikmann to formulate an explicit characteristic equation for the natural frequencies which allows the belt drive designer to examine how system characteristics affect the system eigenvalues. The exact closed-form solution to the dynamic response due to arbitrary excitations and initial conditions is given using eigenfunction expansion. Zhang and Zu continued the analysis of serpentine belt drives in [18] using the method of multiple scales to examine the continuous governing partial differential equations.

Belt bending stiffness, which is assumed to be negligible in the previous works, was studied extensively by Wasfy and Leamy [19]. A finite element technique is extended to include the effect of belt bending stiffness and is used to examine its effect on normal and tangential contact forces on the pulleys, belt wrap angle, belt creep around the pulleys, belt-span tensions, and transverse vibrations. Whereas Wasfy and Leamy's model did not include a tensioner, Kong and Parker [20] studied the effects of belt bending stiffness on natural frequencies and vibration modes in a typical serpentine belt drive system including an automatic tensioner. To incorporate bending stiffness into the model, the belt is modeled as a moving beam as opposed to the moving string model used in previous works. A spatial discretization to solve the eigenvalue problem is developed and the relationship between belt-pulley coupling and bending stiffness is studied. Kong and Parker [21] continued the study of belt bending stiffness by examining their effect on transverse vibrations in belt spans between fixed pulleys. The span equilibrium deflections are determined from a set of nonlinear equations that are solved using ordinary differential equation conversion techniques to reformulate the governing equations into standard boundary value problems to be solved using general purpose BVP code. The results are used to examine the effects of major design variables on equilibrium deflections and coupling indicators.

Parker [22] formulated an efficient method for calculating the eigensolutions and dynamic responses of coupled serpentine belt drive systems. The speed of solution is drastically reduced and the numerical problems that hinder other published methods are eliminated by the use of Lagrange multipliers to enforce geometric boundary conditions at the belt-tensioner interface. However, by coupling the rotational and transverse motions in the spans adjacent to the tensioner, the system of equations becomes significantly more complex than modeling the motions as uncoupled. As a result, the solution techniques required to solve these models demand considerably more computational power. It is therefore important to know what effect coupling has on the responses of the system in order to know the accuracy to which the solutions are limited by using such an assumption.

1.3 THESIS OBJECTIVE

Previous studies in the area of serpentine belt drives have aimed to find more accurate and more efficient ways of modeling the systems. For this reason, it has become common practice for authors to couple the transverse and rotational motions of the belt. However, as a consequence, the models become more complicated and in turn require additional effort to solve. The advantage of coupling the motions has been assumed to be necessary in past works; however the authors have neglected to prove whether it is beneficial to do so. It will be analyzed here whether coupling the motions is indeed necessary.

This thesis aims to quantify the coupling/decoupling effect by 1) modeling serpentine belt drive systems using only rotational motion, 2) modeling these systems by coupling transverse and rotational motion as a result of the action of the tensioner.

Rotational motion permits only longitudinal deflection of the belt. Using rotational motion as the only source of belt displacement effectively decouples the transverse motion from the tensioner arm rotation. With this assumption, the natural frequencies and mode shapes may be found through the nonlinear equations of motion of the system

by linearizing the equations about the steady operating state. Transverse vibration characteristics may be found by applying additional techniques that are decoupled from the rotational characteristics of the system.

Coupling the transverse and rotational motions of the belt spans allows natural frequencies and mode shapes to be revealed that otherwise would be lost by assuming only longitudinal deflection of the belt. The solution corresponding to the coupled equations of motion requires the use of Lagrange multipliers imposing geometric boundary conditions on the belt spans adjacent to the tensioner.

The techniques for modeling and solving the serpentine belt drive systems will be taken from published works. The uncoupled analysis will be borrowed from Hwang et al. [7], and the coupled analysis will be borrowed from Parker [22]. These works were chosen based on the fact that they utilize roughly the same modeling assumptions and dimensional specifications. In addition, both techniques are used to solve a large system of seven pulleys, yet they can each be easily adjusted for an arbitrary number of pulleys. Finally, both works include a case study where the system information is provided along with a presentation of the results. This is beneficial, as the results presented here can be compared to those given by the authors of the original work.

The original contribution of this thesis is the comparison of the two methods through the analysis of their results based on the different system configurations. In addition, experimental results from another work will be used to confirm the accuracy of both techniques.

The impact of coupling on the natural frequency and mode shapes of the system will be analyzed in a parametric engine speed study.

CHAPTER 2

DECOUPLED FORMULATION

This chapter presents the equations of motion of a serpentine belt drive system where transverse motion of the belt is decoupled from the rotational motion. A prototypical model of a serpentine belt drive for rotational motion is first presented and used to formulate the nonlinear equations of motion. An equilibrium analysis is performed to determine steady state characteristics of the system. The equations are then linearized about the steady-state operating point in order to calculate the rotational natural frequencies and mode shapes. A separate model for the transverse motion of the belt tensioner spans is then developed.

2.1 ROTATIONAL MOTION MODEL

The following model and theoretical formulation for the decoupled rotational motion of the serpentine belt drive system is taken directly from Hwang et al. [7] with additional elaboration of computations for completeness.

2.1.1 Problem Formulation

A schematic of the serpentine belt drive setup is shown in Fig. 2.1. This configuration will be used to derive the equations of motion that describe the rotational response of all pulleys due to belt stretching and change in belt tensions. The methodology used herein can be applied to any system of n pulleys. The assumptions used in developing the governing equations are based on the work of Hwang et al. [7], and they include:

1. The belt does not slip on the pulleys.
2. The belt is uniform, perfectly flexible, and stretches in a quasi-static manner.
3. Transverse belt response decouples from longitudinal belt response.
4. The crankshaft motion and any torque inputs from accessories are prescribed (either zero or determined from experiments).

5. The tensioner executes small motions about some steady state position. Moreover the tensioner mechanism is designed to be dissipative and is the dominant source of dissipation. This dissipation is assumed to be linear viscous damping, and dissipation in the belt and fixed pulleys is assumed to be negligible small.

Assumption (3) in effect completely removes any consideration of transverse motion of the belt.

Viewed from the front of the engine as shown in Fig. 2.1, Θ_j is the absolute rotation of the j^{th} pulley taken positive for the rotation caused by the assumed clockwise motion of the belt. It follows that Θ_j is positive in the clockwise direction if the j^{th} pulley is on the interior of the belt loop and positive counter-clockwise if on the exterior of the belt loop. The absolute rotation of the j^{th} pulley is defined as

$$\Theta_j = \omega_j t + \theta_j \tag{2.1}$$

where, t is time and θ_j is the phase angle. The phase angle term represents deviation, under a specified operating speed and accessory loading, from the static equilibrium position of the j^{th} pulley observed at a frequency corresponding to ω_j. The angular velocity of the j^{th} pulley is determined by

$$\omega_j = \frac{V}{R_j} \tag{2.2}$$

where R_j is the radius of the j^{th} pulley, and V is the steady belt transport speed. V is constant and dependent upon the imposed steady state operating speed (RPM) of the crankshaft according to the relationship:

$$V = R_1 * RPM \frac{2\pi}{60} \tag{2.3}$$

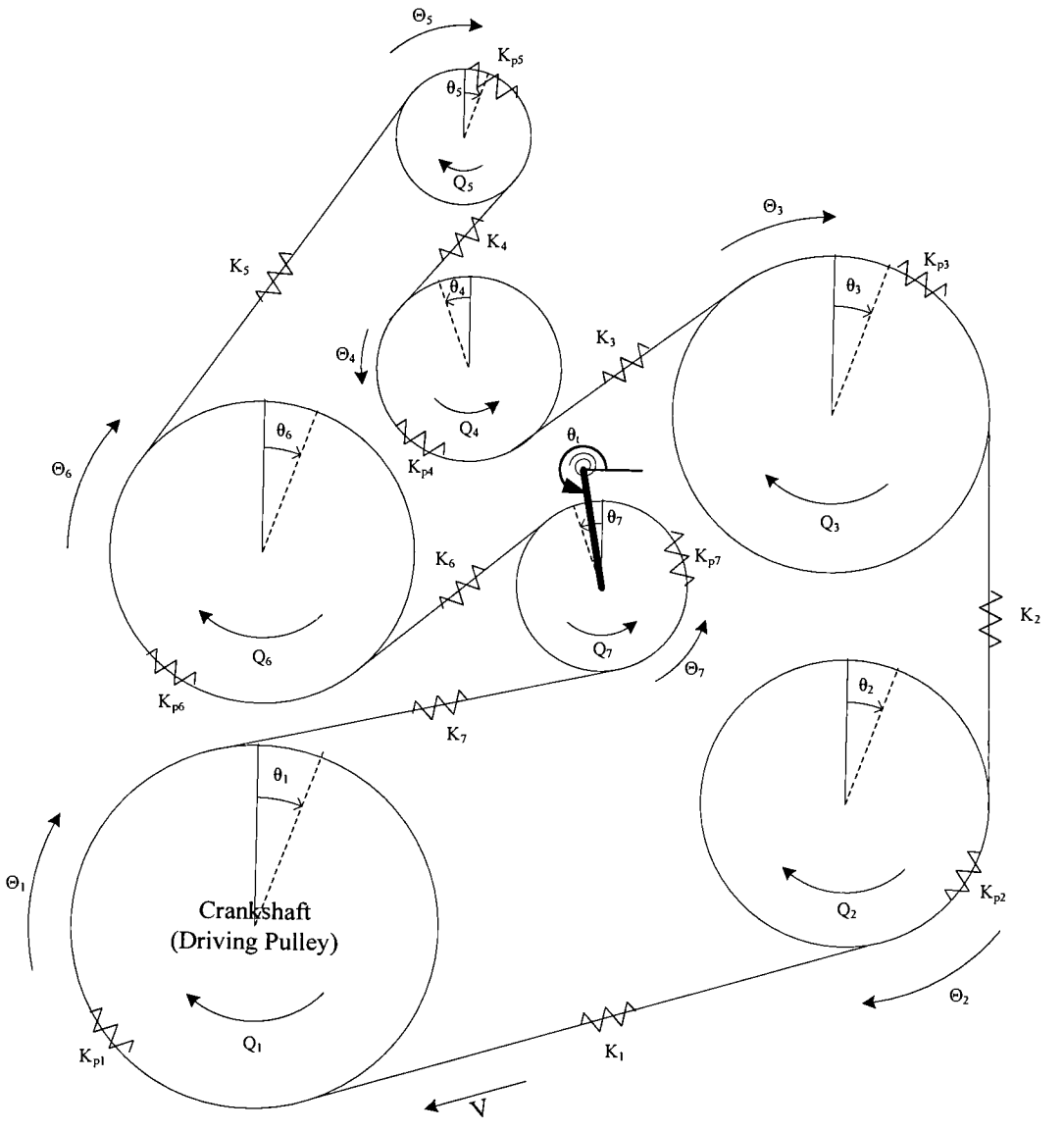

Figure 2.1 Prototypical serpentine belt drive system

Taking the first and second derivatives with respect to time of equation (2.1) yields the angular velocity and angular acceleration respectively

$$\dot{\Theta}_j = \omega_j + \dot{\theta}_j \tag{2.4}$$

$$\ddot{\Theta}_j = \ddot{\theta}_j \tag{2.5}$$

where, $\dot{\theta}_j$ and $\ddot{\theta}_j$ are the velocity and acceleration of the phase angle respectively.

The tensioner arm angle (θ_t) is used to define the location of the tensioner pulley. It is measured between the horizontal and the tensioner arm, taken positive counter-clockwise, as shown in Fig. 2.2. The quantities Q_j and J_j represent the applied external torques and the moment of inertias for each pulley respectively. Due to how Q_j is defined in Fig. 2.1, it must be assigned a negative value to produce a torque resisting the motion of the pulley.

The linear spring constant of each free belt span and arc of contact are represented by K_j and K_{pj} respectively. Based on the assumption that the belt is uniform and stretches in a quasi-static manner, they are calculated by dividing the longitudinal stiffness of the belt (EA) by the length of each portion. The length of the free belt span is described by L_j, and the arc of contact is described by $R_j\phi_j$; where ϕ_j is the wrap angle of the belt around the j^{th} pulley. Length (L_j) and angle (ϕ_j) are calculated from the geometries of the system.

The equation of motion for each fixed center pulley is given by

$$\ddot{\Theta}_j J_j = Q_j + R_j(P_{j-1} - P_j)\,, j=2,3,\ldots,6 \tag{2.6}$$

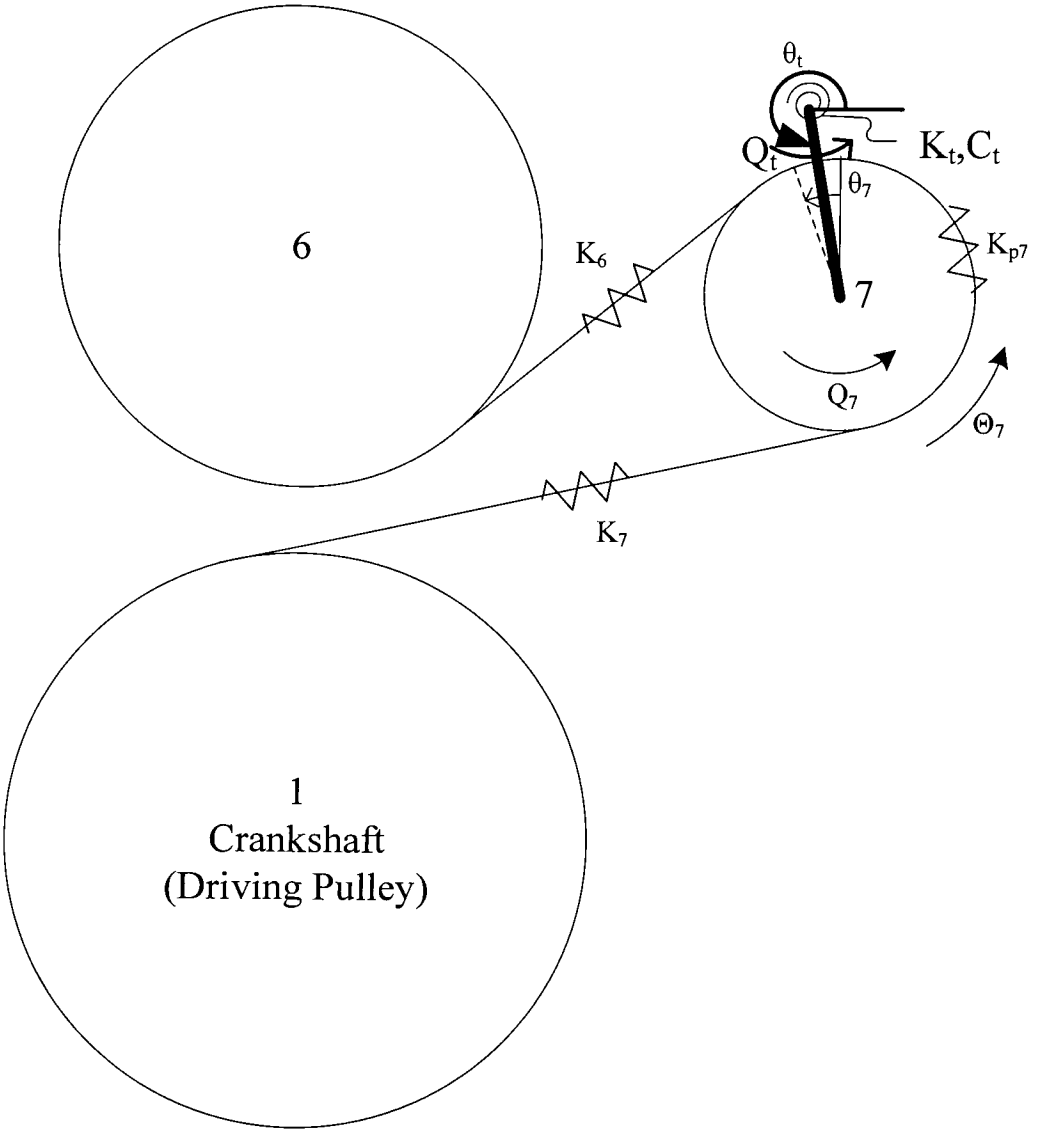

Figure 2.2 Tensioner assembly

where, P_j is the total tension in j^{th} span. Substitution of equation (2.5) into the above equation yields

$$\ddot{\theta}_j J_j = Q_j + R_j(P_{j-1} - P_j), j=2,3,\ldots,6 \tag{2.7}$$

which represents the equation of motion in terms of the phase angle instead of the absolute angle of rotation. The equation will be utilized in this form throughout the rest of the analysis.

The tensioner subsystem consists of pulley 7 at the end the tensioner arm which rotates about the fixed pivot point at the hub. The motion of the tensioner arm is resisted by the hub mounted rotational spring and a viscous damping element at the pivot point. The equations of motion of this system (derived in Appendix A) are given by

$$(\ddot{\theta}_7 + \ddot{\theta}_t)J_7 = Q_7 + R_7(P_6 - P_7) \tag{2.8}$$

$$\begin{aligned} &\ddot{\theta}_t(J_t + J_{7t}) + \ddot{\theta}_7 J_7 + C_t\dot{\theta}_t - K_t(\theta_0 - \theta_t) = \\ &R_7(P_6 - P_7) + L_t \sin(\beta_1)[P_6 - \rho(V + R_7\dot{\theta}_7)^2] \\ &- L_t \sin(\beta_2)[P_7 - \rho(V + R_7\dot{\theta}_7)^2] - m_{eff} L_{eff} g \cos(\theta_t) + Q_t \end{aligned} \tag{2.9}$$

where J_t is the moment of inertia of the tensioner arm about the pivot, J_{7t} is the moment of inertia of the tensioner pulley about the tensioner arm pivot, C_t is damping of the tensioner arm about the pivot, K_t is tensioner arm stiffness, θ_0 is the position of the tensioner arm with the belt installed at zero speed and zero accessory torques, L_t is the length of the tensioner arm, $\beta_{1,2}$ are the orientation angles of the spans adjacent to the tensioner as defined in Fig. 2.3, ρ is the belt mass per unit length, m_{eff} is the total mass of the tensioner assembly, L_{eff} is the distance between the pivot and mass center of the

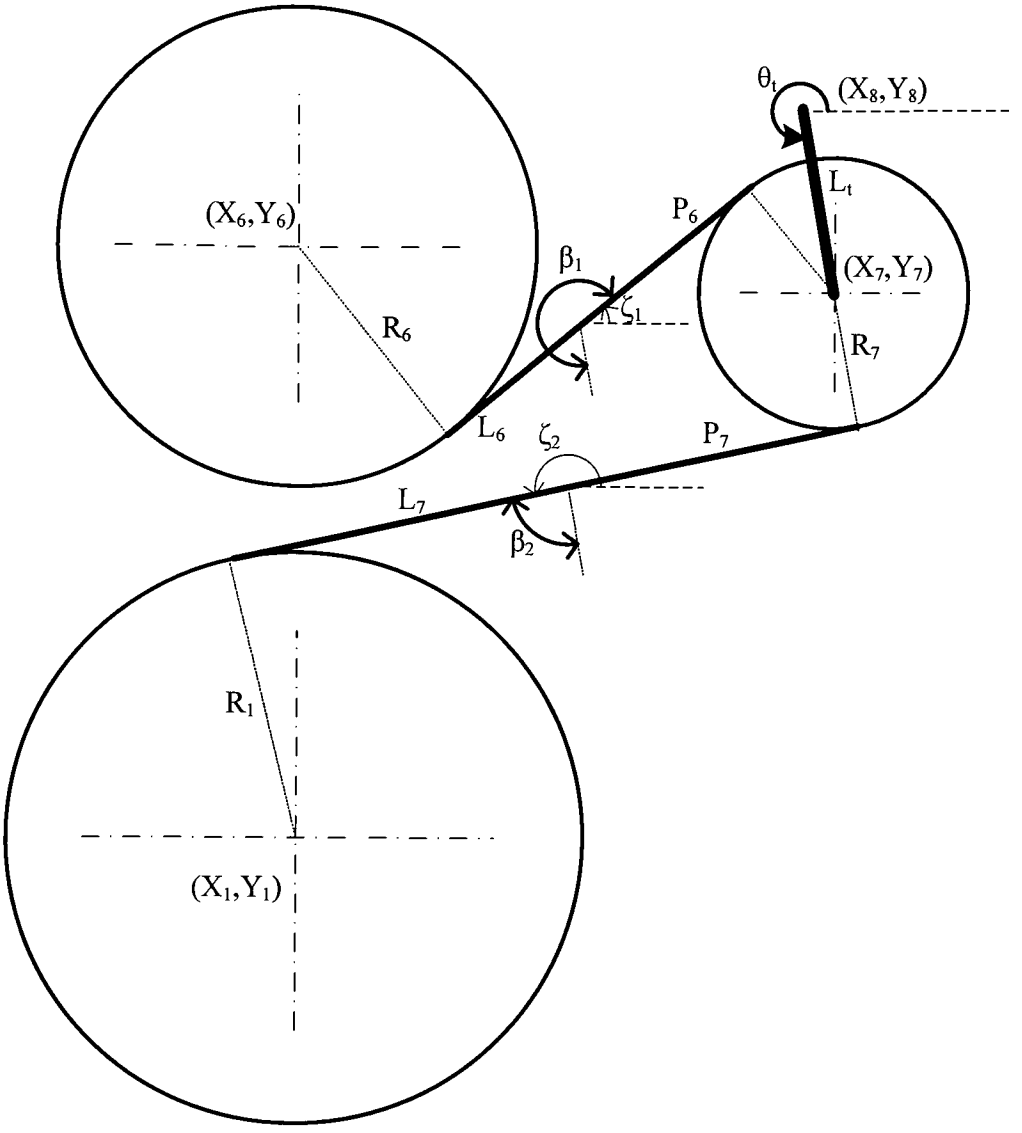

Figure 2.3 Tensioner assembly angles

tensioner assembly, g is the gravitational acceleration, and Q_t is the preload torque on the tensioner spring. The orientation angles $\beta_{1,2}$ are calculated in Appendix B along with the span lengths of the belt sections adjacent to the tensioner. The angle θ_7 is measured relative to a rotating reference frame attached to the tensioner arm at the pivot. The term $\rho(V + R_7\dot{\theta}_7)^2$ represents the centrifugal belt tension. This term provides the centripetal acceleration of the belt as it accelerates around the pulley perimeter and it can be shown to be uniform throughout the system (Beikmann et al. [16]).

In the previous set of equations of motion, there are more unknowns than there are equations to solve them. As a result, additional equations relating the span tensions to the pulley angular positions must be derived. To do this, a linear constitutive law is adopted which describes the belt tension as a function of belt elongation

$$P_j = P_0 + K_j\Delta_j \tag{2.10}$$

where P_0 is a reference static belt tension calculated at zero belt speed and zero accessory torques and Δ_j is the elongation in the longitudinal direction of the j^{th} span. The elongation is related to the pulley rotations through the relationship

$$\Delta_j = R_j\Theta_j - R_{j+1}\Theta_{j+1} - \delta_{j+1} \tag{2.11}$$

where, δ_j is the stretch of the belt over the contact arc of the j^{th} pulley. Substitution of equation (2.1) into the above equation casts the elongation (Δ_j) as a function of the phase angle (θ_j) as follows:

$$\Delta_j = R_j\theta_j - R_{j+1}\theta_{j+1} - \delta_{j+1} \tag{2.12}$$

The stretch (δ_j) is difficult to calculate due to the complicated dynamics of belt creep over the pulley. However, it can be estimated using the average of the adjacent tensions as follows [7]:

$$K_{pj}\delta_j = \frac{(P_{j-1} - P_0) + (P_j - P_0)}{2} \tag{2.13}$$

The reference static tension P_0 must be subtracted from the total tension (P_j) for the reason that δ_j is defined as the *additional* stretch due to motion of the belt. Substitution of equation (2.12) and (2.13) into equation (2.10) and rearranging terms yields

$$\begin{aligned} &P_j\left[1+\frac{K_j}{2K_{pj+1}}\right]+P_{j+1}\left[\frac{K_j}{2K_{pj+1}}\right]= \\ &P_0\left[1+\frac{K_j}{K_{pj+1}}\right]+K_j[R_j\theta_j - R_{j+1}\theta_{j+1}] \end{aligned} \quad ,j=1,2,\ldots,5 \tag{2.14}$$

To account for the change in belt length due to rotation of the tensioner subsystem, spans 6 and 7 must use the following equations which include additional terms beyond those in equation (2.14):

$$\begin{aligned} P_6\left[1+\frac{K_6}{2K_{p7}}\right]+P_7\left[\frac{K_6}{2K_{p7}}\right] &= P_0\left[1+\frac{K_6}{K_{p7}}\right]+K_6[R_6\theta_6 - R_7\theta_7] \\ &+ K_6[(L_6 - L_{6_0}) + (R_6 + R_7)(\zeta_1 - \zeta_{1_0})] \end{aligned} \tag{2.15}$$

$$\begin{aligned} P_7\left[1+\frac{K_7}{2K_{p1}}\right]+P_1\left[\frac{K_7}{2K_{p1}}\right] &= P_0\left[1+\frac{K_7}{K_{p1}}\right]+K_7[R_7\theta_7 - R_1\theta_1] \\ &+ K_7[(L_7 - L_{7_0}) - (R_7 + R_1)(\zeta_2 - \zeta_{2_0})] \end{aligned} \tag{2.16}$$

where the angles $\zeta_{1,2}$ are defined in Fig. 2.3 and calculated in Appendix B. ζ_{1_0}, ζ_{2_0}, L_{6_0}, and L_{7_0} are the reference values of $\zeta_{1,2}$ and $L_{6,7}$ for vanishing belt speed and accessory torques.

The seven unknown coordinates θ_t, θ_j (j=2,3,…,7), are governed by the seven nonlinear equations obtained by substituting equations (2.14)-(2.16) into (2.7)-(2.9). The known inputs to the system are the prescribed motion of the crankshaft (θ_1) and the accessory torques Q_j (j=2,3,…,7).

2.1.2 Equilibrium Analysis

The equilibrium equations are formulated by eliminating the time derivative terms in equations (2.7)-(2.9). The resulting set of nonlinear equations is

$$Q_j = R_j(P_j - P_{j-1}), j=2,3,\ldots,7 \tag{2.17}$$

$$\begin{aligned} -K_t(\theta_0 - \theta_t) &= R_7(P_6 - P_7) + L_t \sin(\beta_1)[P_6 - \rho V^2] \\ &- L_t \sin(\beta_2)[P_7 - \rho V^2] - m_{eff} L_{eff} g \cos(\theta_t) + Q_t \end{aligned} \tag{2.18}$$

Equations (2.17) and (2.18) together with the tension equations (2.14)-(2.16) provide fourteen equations for evaluation of seven steady-state tensions P_j (j=1,2,…,7) and seven pulley coordinates θ_t and θ_j (j=2,3,…,7). The fourteen equations can be reduced to a single equation of the unknown θ_t as follows.

First, the reference tension must be calculated by setting V =0 and realizing that $P_6 = P_7 = P_0$ with vanishing speed and zero accessory torques. As a result, P_0 can be calculated as follows:

$$P_0 = \frac{m_{eff} L_{eff} g \cos(\theta_t) - Q_t - K_t(\theta_0 - \theta_t)}{L_t(\sin(\beta_1) - \sin(\beta_2))} \tag{2.19}$$

Equations (2.14)-(2.17) now represent thirteen linear equations in the thirteen unknowns: P_j (j=1,2,...,7) and θ_j (j=2,3,...,7). Treating θ_t as a parameter, the secant method is used to solve for the steady-state tensions and phase angles. This is accomplished by moving the $-K_t(\theta_0 - \theta_t)$ term to the right side of equation (2.18) to form the following general equation from which the equilibrium θ_t will be calculated.

$$\begin{aligned} F(\theta_t) = {} & K_t(\theta_0 - \theta_t) + R_7(P_6 - P_7) + L_t \sin(\beta_1)\left[P_6 - \rho V^2\right] \\ & - L_t \sin(\beta_2)\left[P_7 - \rho V^2\right] - m_{eff} L_{eff} g \cos(\theta_t) + Q_t \end{aligned} \tag{2.20}$$

where, $F(\theta_t)$ represents a function of θ_t. Employing the secant method, an initial guess of θ_t is made for some steady operating speed. Using equations (2.14)-(2.17), the corresponding tensions and phase angles are calculated. A second guess of θ_t is made and the same procedure is used to find the respective tensions and phase angles. The function $F(\theta_t)$ is evaluated for each guess of θ_t and the secant method is used to find the next value of θ_t. This iterative process continues until the change in θ_t approaches zero. The resulting θ_t is the equilibrium position of the tensioner arm at some steady operating speed and accessory torque loading. The subsequent equilibrium span tensions and phase angle position are found by back substitution into equations (2.14)-(2.17).

2.1.3 Vibration Analysis

The rotational vibration of the system is investigated by linearizing the equations of motion (2.7)-(2.9) and (2.14)-(2.16) about the equilibrium state defined by (2.17) and (2.18). Results of the analysis are used to determine the natural frequencies and mode shapes. The linearized set of equations of motion are written as

$$[M]\ddot{\xi}+[C]\dot{\xi}+[K]\xi=0 \tag{2.21}$$

where, $\xi=[\theta_t,\theta_2,\ldots,\theta_7]^T$, $[M]$ is the mass matrix, $[C]$ is the damping matrix, and $[K]$ is the stiffness matrix. To determine the elements of the mass, damping and stiffness matrices, the tension must be linearized into equations (2.7)-(2.9), then substituted into equations (2.14)-(2.16). The procedure for linearizing the tension begins with defining small perturbations of the phase angles and phase angle velocities about the equilibrium values:

$$\begin{aligned}
\theta_t &= \theta_t^e + \varepsilon_t \\
\theta_1 &= \theta_1^e + \varepsilon_1 \\
\theta_2 &= \theta_2^e + \varepsilon_2 \\
&\vdots \\
\theta_7 &= \theta_7^e + \varepsilon_7 \\
\dot{\theta}_t &= \dot{\theta}_t^e + \dot{\varepsilon}_t \\
\dot{\theta}_1 &= \dot{\theta}_1^e + \dot{\varepsilon}_1 \\
\dot{\theta}_2 &= \dot{\theta}_2^e + \dot{\varepsilon}_2 \\
&\vdots \\
\dot{\theta}_7 &= \dot{\theta}_7^e + \dot{\varepsilon}_7
\end{aligned} \tag{2.22}$$

where the equilibrium values are denoted by the superscript ^{e} and ε represents a small perturbation from equilibrium. In equation (2.22), the $\dot{\theta}^e$ terms are equal to zero as they represent the phase angle velocity at equilibrium. Noting that the tensions are functions of the θ_j, as shown by equations (2.14)-(2.16), and since $\ddot{\theta}^e$ equals zero; equation (2.7) becomes

$$\begin{aligned}
J_j\ddot{\varepsilon}_j = {} & Q_j + R_jP_{j-1}(\theta_t^e+\varepsilon_t,\theta_2^e+\varepsilon_2,\ldots,0+\dot{\varepsilon}_7) \\
& - R_jP_j(\theta_t^e+\varepsilon_t,\theta_2^e+\varepsilon_2,\ldots,0+\dot{\varepsilon}_7)
\end{aligned} \quad ,j=2,3,\ldots,6 \tag{2.23}$$

where P_{j-1} and P_j are functions of the variables in parenthesis. Employing a multi-variable Taylor series expansion of P_{j-1} and P_j about the equilibrium position, equation (2.23) can be rewritten with tension terms linearized as

$$\begin{aligned} J_j\ddot{\varepsilon}_j &= Q_j + R_j P_{j-1}(\theta_1^e,\theta_2^e,\ldots,0) \\ &\quad + R_j(\partial P_{j-1}/\partial\theta_1)\big|_e\varepsilon_1 \\ &\quad + R_j(\partial P_{j-1}/\partial\theta_2)\big|_e\varepsilon_2 \\ &\quad \vdots \\ &\quad + R_j(\partial P_{j-1}/\partial\dot{\theta}_7)\big|_e\dot{\varepsilon}_7 \\ &\quad - R_j P_j(\theta_1^e,\theta_2^e,\ldots,0) \\ &\quad - R_j(\partial P_j/\partial\theta_1)\big|_e\varepsilon_1 \\ &\quad - R_j(\partial P_j/\partial\theta_2)\big|_e\varepsilon_2 \\ &\quad \vdots \\ &\quad - R_j(\partial P_j/\partial\dot{\theta}_7)\big|_e\dot{\varepsilon}_7 \end{aligned} \qquad j=2,3,\ldots,6 \tag{2.24}$$

In the above equation, only the first order differential terms are utilized as higher order terms are ignored given that the perturbations about equilibrium are small. Noting $Q_j + R_j P_{j-1}(\theta_1^e,\theta_2^e,\ldots,0) - R_j P_j(\theta_1^e,\theta_2^e,\ldots,0) = 0$, rearranging of terms yields:

$$\begin{aligned} &J_j\ddot{\varepsilon}_j + R_j[(\partial P_j/\partial\theta_1)\big|_e - (\partial P_{j-1}/\partial\theta_1)\big|_e]\varepsilon_1 \\ &+ R_j[(\partial P_j/\partial\theta_2)\big|_e - (\partial P_{j-1}/\partial\theta_2)\big|_e]\varepsilon_2 \\ &\vdots \\ &+ R_j[(\partial P_j/\partial\theta_7)\big|_e - (\partial P_{j-1}/\partial\theta_7)\big|_e]\varepsilon_7 \\ &+ R_j[(\partial P_j/\partial\dot{\theta}_1)\big|_e - (\partial P_{j-1}/\partial\dot{\theta}_1)\big|_e]\dot{\varepsilon}_1 \\ &+ R_j[(\partial P_j/\partial\dot{\theta}_2)\big|_e - (\partial P_{j-1}/\partial\dot{\theta}_2)\big|_e]\dot{\varepsilon}_2 \\ &\vdots \\ &+ R_j[(\partial P_j/\partial\dot{\theta}_7)\big|_e - (\partial P_{j-1}/\partial\dot{\theta}_7)\big|_e]\dot{\varepsilon}_7 \\ &= 0 \end{aligned} \qquad j=2,3,\ldots,6 \tag{2.25}$$

The mass, damping and stiffness matrix terms are not yet complete as only five equations have been used to describe seven coordinates. The final two equations to be linearized are (2.8) and (2.9). Linearizing tension into equation (2.8) is completed in the same manner as previously described; however the rotational inertia term must account for the rotation of both the pulley and the tensioner subsystem. As a result, the $J_j\ddot{\varepsilon}_j$ term in equation (2.25) becomes $J_7\ddot{\varepsilon}_7 + J_7\ddot{\varepsilon}_t$ for the case of j=7. Linearization of equation (2.9) is completed as follows:

$$\begin{aligned} J_7\ddot{\varepsilon}_7 + (J_7 + J_{7t})\ddot{\varepsilon}_t = & -C_t(\dot{\theta}_t^e + \dot{\varepsilon}_t) + K_t\theta_0 - K_t(\theta_t^e + \varepsilon_t) \\ & + R_7P_6(\theta_t^e + \varepsilon_t, \theta_2^e + \varepsilon_2, \ldots, 0 + \dot{\varepsilon}_7) \\ & - R_7P_7(\theta_t^e + \varepsilon_t, \theta_2^e + \varepsilon_2, \ldots, 0 + \dot{\varepsilon}_7) \\ & + L_t \sin\beta_1\{P_6(\theta_t^e + \varepsilon_t, \theta_2^e + \varepsilon_2, \ldots, 0 + \dot{\varepsilon}_7) - \rho[V + R_7(\dot{\theta}_7^e + \dot{\varepsilon}_7)]\} \\ & - L_t \sin\beta_2\{P_7(\theta_t^e + \varepsilon_t, \theta_2^e + \varepsilon_2, \ldots, 0 + \dot{\varepsilon}_7) - \rho[V + R_7(\dot{\theta}_7^e + \dot{\varepsilon}_7)]\} \\ & m_{eff}L_{eff}g\cos(\theta_t^e + \varepsilon_t) + Q_t \end{aligned} \tag{2.26}$$

Recognizing again that the sum of the equilibrium terms equals zero, and noting that $\cos(\theta_t^e + \varepsilon_t)$ can be transformed using trig identities and Taylor series expansion, rearranging of the remaining terms of equation (2.26) provides the final form

$$\begin{aligned} & J_7\ddot{\varepsilon}_7 + (J_7 + J_{7t})\ddot{\varepsilon}_t \\ & + \{K_t + R_7[(\partial P_7/\partial\theta_t)|_e - (\partial P_6/\partial\theta_t)|_e] - L_t\sin\beta_1(\partial P_6/\partial\theta_t)|_e + L_t\sin\beta_2(\partial P_7/\partial\theta_t)|_e - m_{eff}L_{eff}g\sin\theta_t^e\}\varepsilon_t \\ & + \{R_7[(\partial P_7/\partial\theta_2)|_e - (\partial P_6/\partial\theta_2)|_e] - L_t\sin\beta_1(\partial P_6/\partial\theta_2)|_e + L_t\sin\beta_2(\partial P_7/\partial\theta_2)|_e\}\varepsilon_2 \\ & \vdots \\ & + \{R_7[(\partial P_7/\partial\theta_7)|_e - (\partial P_6/\partial\theta_7)|_e] - L_t\sin\beta_1(\partial P_6/\partial\theta_7)|_e + L_t\sin\beta_2(\partial P_7/\partial\theta_7)|_e\}\varepsilon_7 \\ & + \{C_t + R_7[(\partial P_7/\partial\dot{\theta}_t)|_e - (\partial P_6/\partial\dot{\theta}_t)|_e] - L_t\sin\beta_1(\partial P_6/\partial\dot{\theta}_t)|_e + L_t\sin\beta_2(\partial P_7/\partial\dot{\theta}_t)|_e\}\dot{\varepsilon}_t \\ & + \{R_7[(\partial P_7/\partial\dot{\theta}_2)|_e - (\partial P_6/\partial\dot{\theta}_2)|_e] - L_t\sin\beta_1(\partial P_6/\partial\dot{\theta}_2)|_e + L_t\sin\beta_2(\partial P_7/\partial\dot{\theta}_2)|_e\}\dot{\varepsilon}_2 \\ & \vdots \\ & + \{R_7[(\partial P_7/\partial\dot{\theta}_7)|_e - (\partial P_6/\partial\dot{\theta}_7)|_e] - L_t\sin\beta_1(\partial P_6/\partial\dot{\theta}_7)|_e + L_t\sin\beta_2(\partial P_7/\partial\dot{\theta}_7)|_e + L_t\sin\beta_1\rho R_7 - L_t\sin\beta_2\rho R_7\}\dot{\varepsilon}_7 \\ & = 0 \end{aligned} \tag{2.27}$$

The mass, damping and stiffness matrices can now be assembled from the equations presented above; they are presented in Appendix C. The partial derivative terms in equations (2.24)-(2.27) are determined numerically since the tensions cannot be explicitly written in terms of phase angles θ_j. Calculation of the partial derivatives is accomplished according to

$$(\partial P_j / \partial \theta_i)\big|_e \approx \frac{[P_j(\theta_1^e, \theta_2^e, \ldots, \theta_{i-1}^e, \theta_i^e + \varepsilon, \theta_{i+1}^e, \ldots, \dot{\theta}_7^e) - P_j(\theta_1^e, \theta_2^e, \theta_3^e, \ldots, \dot{\theta}_7^e)]}{\varepsilon} \qquad (2.28)$$

$$j=1,2,3,\ldots,7$$

$$i=t,2,3,\ldots,7$$

where ε is some small perturbation of the j^{th} pulley from its equilibrium position.

With the mass, damping and stiffness matrices assembled, the eigenvalues and eigenvectors can be determined. Assuming a solution for equation (2.21); of the form

$$Z(t) = \xi e^{2\pi\omega t} \qquad (2.29)$$

the resulting eigenvalue problem is the following

$$\{(2\pi\omega_n)^2[M] + 2\pi\omega_n[C] + [K]\}\xi = 0 \qquad (2.30)$$

The natural frequencies and mode shapes of the system are determined numerically from the previous equation. The natural frequencies are given by the imaginary parts of the eigenvalues due to the damping term, and the mode shapes are determined from the eigenvectors ξ_j, j=1,2,…,7.

2.2 TRANSVERSE MOTION MODEL – TENSIONER SPANS

As a result of assumption (3), the previous formulation neglects transverse motion of all belt spans. Assumption (3) is purely a simplification of the system and it permits simplified computation of the rotational eigenvalues and eigenvectors. However, there still exist transverse motions of the belt, particularly in those spans adjacent to the tensioner.

Increased velocity of the belt will increase belt tension; however due to the fact that the tensioner support is not rigid, the resulting belt stretch will allow the tensioner to relax. The interaction between a non-rigid tensioner support and the adjacent spans is considered by Mote [1]. Results are presented by Abrate [23] in a form that is easily adaptable to serpentine belt drive systems. The reference tensions within the span are calculated as

$$P_{rj} = P_j - \eta \rho V^2 \tag{2.31}$$

where P_{rj} is the reference tension of the j^{th} span, and η is a constant that depends upon the relative stiffness of the support and belt. For spans adjacent to the non-rigid tensioner, η can be calculated according to Beikmann et al. [24] as

$$\eta = \frac{k_b}{k_b + k_s + k_g} \tag{2.32}$$

where

$$k_b = \frac{EA}{L_{belt}} \left(\cos\psi_1 + \cos\psi_2 \right) \tag{2.33}$$

$$k_s = \frac{K_t}{L_t^2} \tag{2.34}$$

$$k_g = P_{rj}\left(\frac{d\cos(\psi_1)}{dx_s} + \frac{d\cos(\psi_2)}{dx_s}\right) \tag{2.35}$$

where, $\psi_{1,2}$ are defined in Fig. 2.4, x_s is the tensioner support motion, and L_{belt} is the length of the entire belt. Since the terms $\frac{d\cos(\psi_{1,2})}{dx_s}$ are approximately zero, the k_g term can be neglected.

The transverse natural frequencies of the spans are now calculated as

$$\omega_n = \frac{n\pi}{L_j}\cdot\left(\frac{P_{rj}}{\rho}\right)^{1/2}\cdot\left(1-\kappa\frac{V^2}{c^2}\right)\left(1+\eta\frac{V^2}{c^2}\right)^{-1/2} \tag{2.36}$$

where, ω_n is the transverse natural frequency, n is the mode to be calculated, L_j is the length of the individual span, $\kappa = 1-\eta$, and

$$c = \sqrt{\frac{P_{rj}}{\rho}} \tag{2.37}$$

where, c is the propagation speed of transverse waves relative to the belt.

2.3 TRANSVERSE MOTION MODEL – FIXED-FIXED SPANS

Transverse motion may occur not only in the spans adjacent to the tensioner, but also in spans bounded by rigid pulleys. Unlike the tensioner, rigid pulleys rotate about a fixed axis. Assuming negligible bending stiffness of the belt, the transverse motions of the fixed-fixed belt spans are linearly decoupled from the rotational motions of the pulleys.

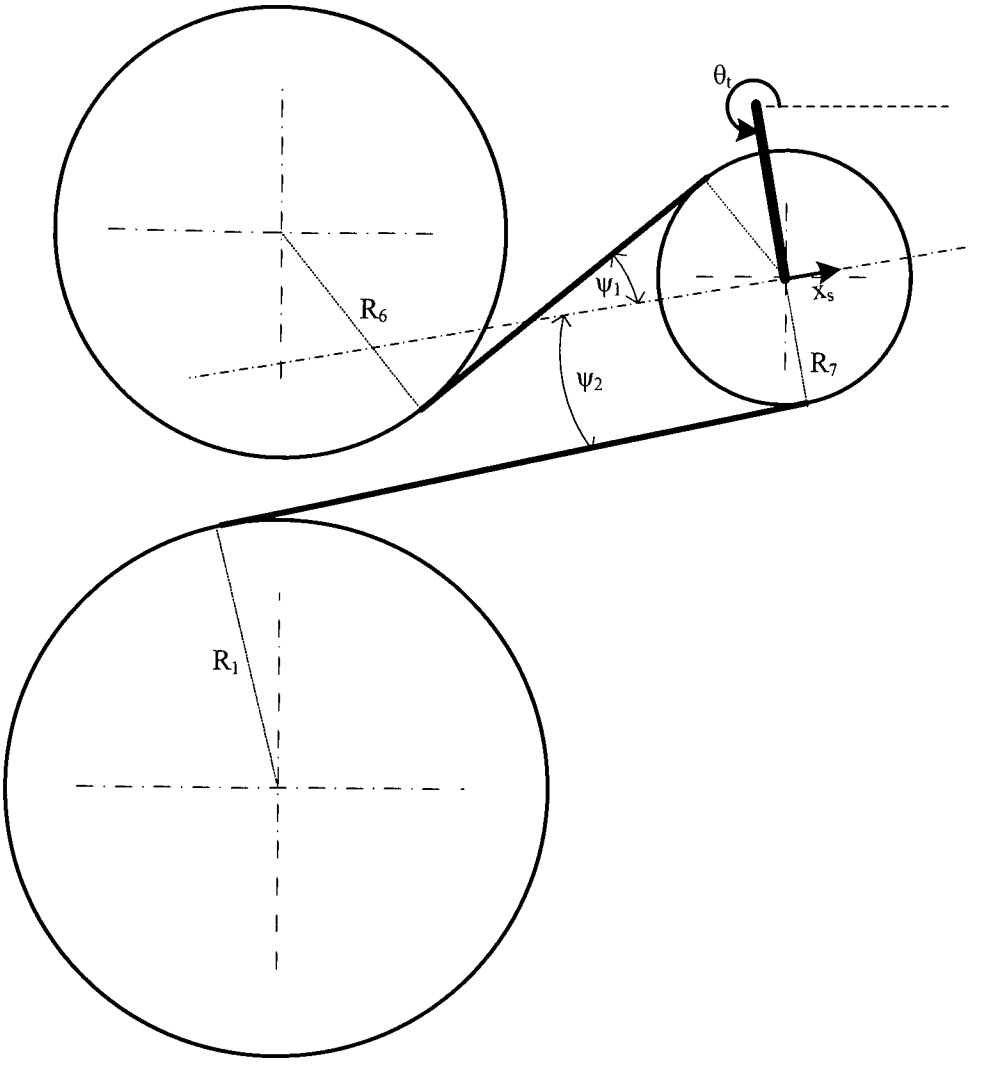

Figure 2.4 Tensioner motion and angle definition

However, excitations of the transverse modes may occur due to pulley eccentricities or irregularities of the accessory torques. As a result, it is important to know the transverse natural frequencies. Beikmann [13] presented a formula to determine the transverse natural frequencies of a moving string

$$\omega_n = \frac{n\pi \cdot c_j'}{L_j} \tag{2.38}$$

where, c_j' is the mean effective wave velocity for the j^{th} span and is calculated by:

$$c_j' = \frac{c_j^2 - V^2}{c_j} \tag{2.39}$$

In the above equation, c_j is calculated differently than in equation (2.37) as follows:

$$c_j = \sqrt{\frac{P_j}{\rho}} \tag{2.40}$$

where the tension term P_j used here represents the total equilibrium operating tension.

Upon further examination of equations (2.36) and (2.38), it is evident that they are basically the same with the exception that equation (2.36) accounts for the flexibility of the tensioner support. By setting η equal to zero, indicating a rigid support, it can be shown that equation (2.36) reduces to equation (2.38).

2.4 ALGORITHM FOR DECOUPLED SOLUTION

Presented below in Fig. 2.5 is a flow chart that outlines the procedure presented previously throughout Chapter 2 that one must follow to solve the decoupled serpentine belt drive model. Results of the formulation include the operating belt tensions,

equilibrium phase angles, system natural frequencies and their corresponding mode shapes.

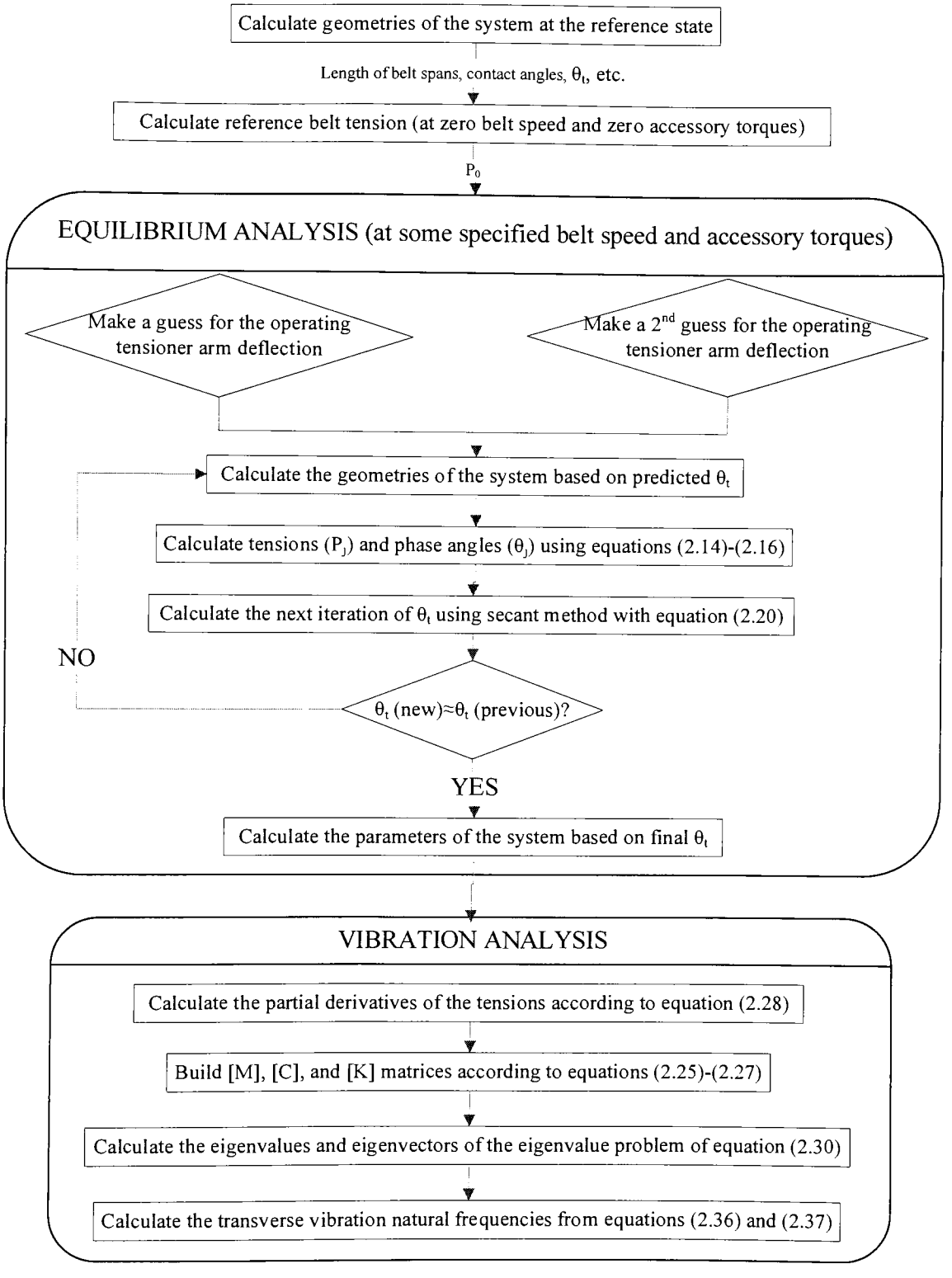

Figure 2.5 Algorithm for the decoupled analysis

CHAPTER 3

COUPLED FORMULATION

This chapter presents a method for determining the natural frequencies and mode shapes of serpentine belt drive systems where the transverse motions of the belt spans adjacent to the tensioner are coupled to the rotational motion. The equations of motion are presented and given an extended operator form in order to facilitate discretization of the belt spans adjacent to the tensioner. An equilibrium analysis is performed to determine the steady state operating belt tensions and tensioner arm position. Lagrange multipliers are used to enforce the geometric boundary conditions at the span-tensioner interface. The final discretized form is used to calculate the dynamic response of the system.

3.1 PARTIALLY COUPLED MOTION MODEL

Equilibrium analysis is used to set the operating position of the tensioner arm and the span tensions due to some steady operating speed and accessory torque loading. For small belt motions, the linearized model decouples the transverse motion of all belt spans, except those adjacent to the tensioner, from the rotational motion of the pulleys. The spans adjacent to the tensioner remain coupled to the rotational motion due the condition that their boundary motion depends upon tensioner rotation and translation. This crucial detail is the motivation behind the extended formulation presented here. The rotational model in Section 2.1 neglects this coupling and as a result it cannot capture the transverse motion of the spans.

3.1.1 Equations of Motion

The model shown in Fig. 3.1 is used to derive the equations of motion governing the response of a serpentine belt drive system to a specified input motion from the crankshaft. It can be adapted to any system of n-pulleys as the model shown consists of all the necessary components of a serpentine belt drive system including a single belt,

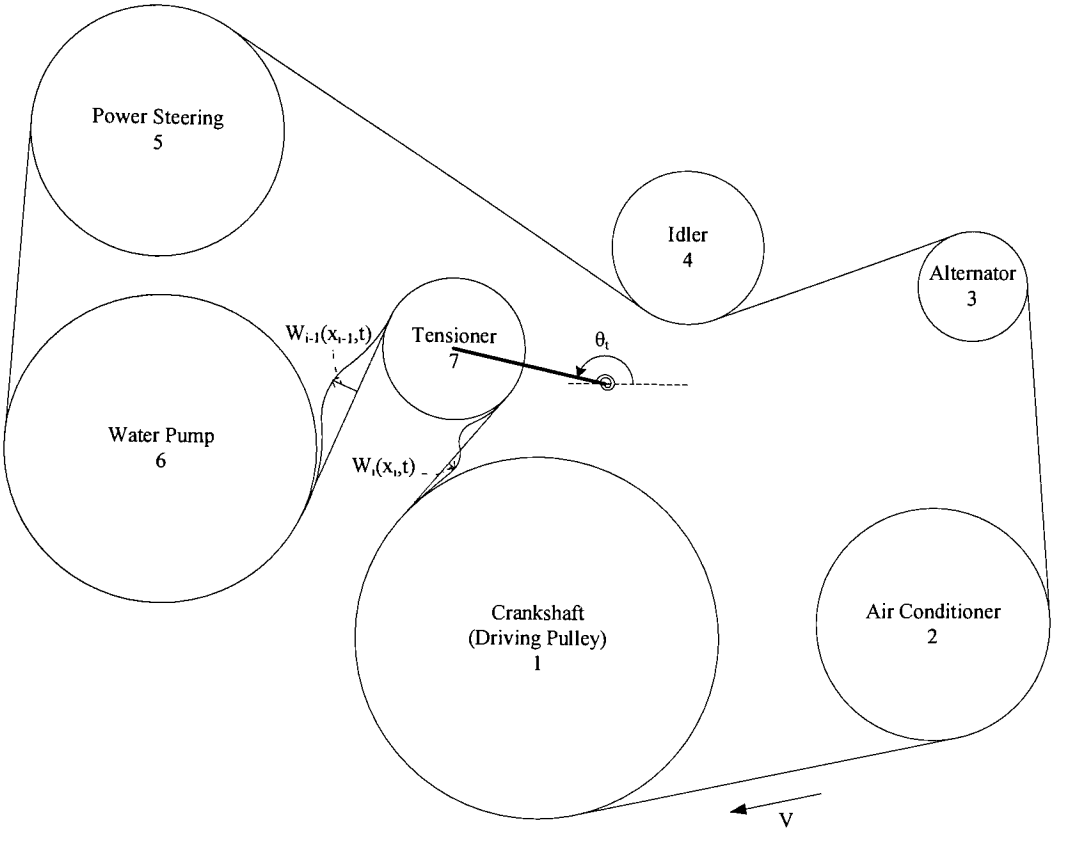

Figure 3.1 Serpentine belt drive model

driving pulley, driven pulleys, and tensioner. The equations of motion presented here are used to calculate the rotational vibration characteristics of the system as well as the transverse vibrations in the spans adjacent to the tensioner. The following formulation is based on the work of Parker [22] where the key assumptions preserved herein include:

1. The belt properties and belt speed are uniform.
2. Belt bending stiffness is negligible.
3. Damping is not modeled.
4. Belt-pulley wedging and belt slip at the belt-pulley interfaces are not considered.

Assumptions (1), (2), and (4) above are the same as those used in Chapter 2. However, assumption (3) is not consistent with the model in Chapter 2 as tensioner damping is not employed here. This discrepancy will be investigated when the solutions are compared in chapter 4.

The equations of motion presented here can be derived using Hamilton's principle as described in Beikmann's [13] work. The nonlinear equations of motion are linearized for small transverse belt motions about an equilibrium state. Transverse motions of the belt are described by the term $W_j(x,t)$ which represents the transverse displacement of the j^{th} span taken positive for deflection toward the interior of the belt loop as shown in Fig. 3.2. As described in Chapter 2, the crankshaft (pulley 1) is the driving pulley which rotates clockwise to induce a clockwise motion of the belt. θ_j is the phase angle of the j^{th} pulley as utilized in Chapter 2. However, the tensioner pulley rotation (θ_i) is the absolute rotation, not the rotation relative to the tensioner arm as in Chapter 2.

The transverse motions of the belt spans adjacent to the tensioner are governed by the following equation:

$$\rho\frac{\partial^2 W_j}{\partial t^2} - 2\rho V\frac{\partial^2 W_j}{\partial x \partial t} - \left(P_j - \rho V^2\right)\frac{\partial^2 W_j}{\partial x^2} = 0, j=i\text{-}1,i \tag{3.1}$$

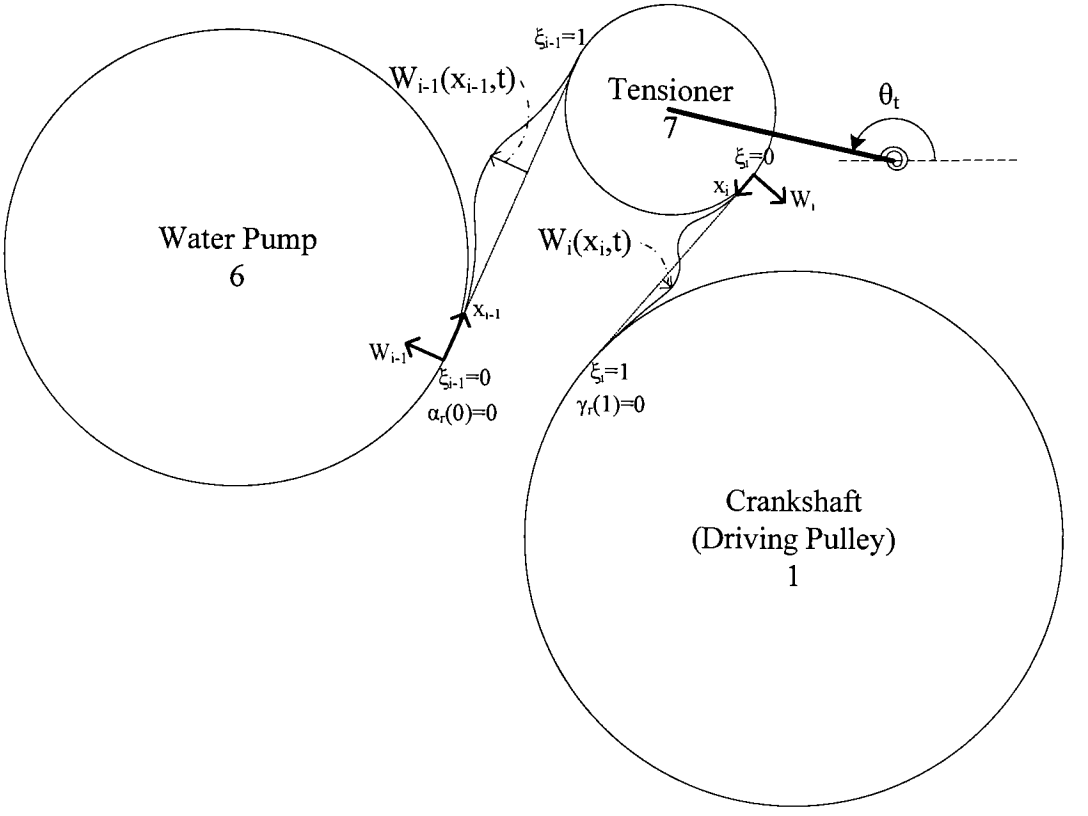

Figure 3.2 Tensioner span coordinates

where i signifies the tensioner pulley. The spans have zero boundary conditions for the endpoints away from the tensioner

$$W_{i-1}\big|_0 = 0, \quad W_i\big|_{L_i} = 0 \tag{3.2}$$

However, at the span-tensioner interface, the transverse displacements of the spans are dependent upon the rotation of the tensioner arm according to

$$W_{i-1}\big|_{L_{i-1}} = L_t\theta_t \cos\beta_1, \quad W_i\big|_0 = L_t\theta_t \cos\beta_2 \tag{3.3}$$

The rotational motion of the pulleys and the tensioner arm are governed by the following equations:

$$J_j\ddot{\theta}_j + K_jR_j\left(R_j\theta_j - R_{j+1}\theta_{j+1}\right) - K_{j-1}R_j\left(R_{j-1}\theta_{j-1} - R_j\theta_j\right) = Q_j, j=2,\ldots,n, \quad j\neq i\text{-}1, i, i+1; \tag{3.4}$$

$$J_{i-1}\ddot{\theta}_{i-1} + K_{i-1}R_{i-1}\left(R_{i-1}\theta_{i-1} - R_i\theta_i - L_t\theta_t \sin\beta_1\right) - K_{i-2}R_{i-1}\left(R_{i-2}\theta_{i-2} - R_{i-1}\theta_{i-1}\right) = Q_{i-1}, i\neq 2 \tag{3.5}$$

$$J_i\ddot{\theta}_i + K_iR_i\left(R_i\theta_i - R_{i+1}\theta_{i+1} + L_t\theta_t \sin\beta_2\right) - K_{i-1}R_i\left(R_{i-1}\theta_{i-1} - R_i\theta_i - L_t\theta_t \sin\beta_1\right) = Q_i \tag{3.6}$$

$$J_{i+1}\ddot{\theta}_{i+1} + K_{i+1}R_{i+1}\left(R_{i+1}\theta_{i+1} - R_{i+2}\theta_{i+2}\right) - K_iR_{i+1}\left(R_i\theta_i - R_{i+1}\theta_{i+1} + L_t\theta_t \sin\beta_2\right) = Q_{i+1}, i\neq n \tag{3.7}$$

$$J_t\ddot{\theta}_t + \left(\frac{K_t}{L_t} + K_{i-1}L_t\sin^2\beta_1 + K_iL_t\sin^2\beta_2\right)L_t\theta_t - K_{i-1}L_t\left(R_{i-1}\theta_{i-1} - R_i\theta_i\right)\sin\beta_1$$
$$+ K_iL_t\left(R_i\theta_i - R_{i+1}\theta_{i+1}\right)\sin\beta_2 + \rho VL_t\left(\frac{\partial W_{i-1}}{\partial t}\Big|_{L_{i-1}}\cos\beta_1 - \frac{\partial W_i}{\partial t}\Big|_0\cos\beta_2\right) \qquad (3.8)$$
$$+ \left(P_{i-1} - \rho V^2\right)L_t\frac{\partial W_{i-1}}{\partial x}\Big|_{L_{i-1}}\cos\beta_1 - \left(P_i - \rho V^2\right)L_t\frac{\partial W_i}{\partial x}\Big|_0\cos\beta_2 = 0$$

where, $J_t = J_{arm} + m_iL_t^2$; m_i is the mass of the tensioner pulley, P_j is the equilibrium tension in the j^{th} span, and Q_j are the moments on the accessory pulleys (with steady, average moments being negative as defined in Chapter 2). The convention $\theta_{n+1} = \theta_1$ is used.

The equations of motion are now cast in dimensionless form with the angular rotations θ_j defined in terms of a new coordinate ψ_j according to

$$R_j\theta_j = R_1\theta_1 - R_1\psi_j \Rightarrow \psi_j = \theta_1 - \frac{R_j\theta_j}{R_1} \qquad (3.9)$$

where, according to the convention adopted above, $\psi_1 = \psi_{n+1} = 0$. The rest of the dimensionless parameters of the system are

$$l_t = \frac{L_t}{R_1},\ l_j = \frac{L_j}{L_1},\ w_j = \frac{W_j}{R_1},\ \hat{x}_j = \frac{x_j}{L_1},\ r_1 = \frac{R_1}{L_1},\ v = \frac{V}{\sqrt{P_1/\rho}},\ \hat{t} = \frac{t}{\sqrt{\rho L_1^2/P_1}}$$
$$p_j = \frac{P_j}{P_1},\ k_b = \frac{EA}{P_1},\ k_j = \frac{L_1K_j}{P_1} = \frac{k_b}{l_j},\ k_t = \frac{L_1K_t}{L_t^2P_1},\ \hat{J}_t = \frac{J_t}{\rho L_1R_1^2},\ \hat{J}_j = \frac{J_j}{\rho L_1R_j^2},$$
$$q_j = \frac{Q_j}{P_1R_jR_1/L_1} \qquad (3.10)$$

Using the above definitions, the governing equations are cast into dimensionless form as follows:

$$\frac{\partial^2 w_j}{\partial \hat{t}^2} - 2v\frac{\partial^2 w_j}{\partial \hat{x}_j \partial \hat{t}} - \left(p_j - v^2\right)\frac{\partial^2 w_j}{\partial \hat{x}^2} = 0, j=i\text{-}1,i \tag{3.11}$$

$$w_{i-1}\big|_0 = 0, \quad w_i\big|_{l_i} = 0 \tag{3.12}$$

$$w_{i-1}\big|_{l_{i-1}} = l_t\theta_t \cos\beta_1, \quad w_i\big|_0 = l_t\theta_t \cos\beta_2 \tag{3.13}$$

$$\hat{J}_j\ddot{\psi}_j + \frac{k_b}{l_j}\left(\psi_j - \psi_{j+1}\right) - \frac{k_b}{l_{j-1}}\left(\psi_{j-1} - \psi_j\right) = \hat{J}_j\ddot{\theta}_1 - q_j,\ j=2,\ldots,n \quad j\neq i\text{-}1,\ i,\ i+1; \tag{3.14}$$

$$\hat{J}_{i-1}\ddot{\psi}_{i-1} + \frac{k_b}{l_{j-1}}\left(\psi_{i-1} - \psi_i + l_t\theta_t \sin\beta_1\right) - \frac{k_b}{l_{j-2}}\left(\psi_{i-2} - \psi_{i-1}\right) = \hat{J}_{i-1}\ddot{\theta}_1 - q_{i-1},\ i\neq 2 \tag{3.15}$$

$$\hat{J}_i\ddot{\psi}_i + \frac{k_b}{l_i}\left(\psi_i - \psi_{i+1} - l_t\theta_t \sin\beta_2\right) - \frac{k_b}{l_{i-1}}\left(\psi_{i-1} - \psi_i + l_t\theta_t \sin\beta_1\right) = \hat{J}_i\ddot{\theta}_1 - q_i \tag{3.16}$$

$$\hat{J}_{i+1}\ddot{\psi}_{i+1} + \frac{k_b}{l_{i+1}}\left(\psi_{i+1} - \psi_{i+2}\right) - \frac{k_b}{l_i}\left(\psi_i - \psi_{i+1} - l_t\theta_t \sin\beta_2\right) = \hat{J}_{i+1}\ddot{\theta}_1 - q_{i+1},\ i\neq n \tag{3.17}$$

$$\begin{aligned}\hat{J}_t\ddot{\theta}_t &+ \left(k_t + \frac{k_b}{l_{i-1}}\sin^2\beta_1 + \frac{k_b}{l_i}\sin^2\beta_2\right)l_t^2\theta_t - \frac{k_b}{l_{i-1}}l_t\left(\psi_i - \psi_{i-1}\right)\sin\beta_1 \\ &+ \frac{k_b}{l_i}l_t\left(\psi_{i+1} - \psi_i\right)\sin\beta_2 + vl_t\left(\frac{\partial w_{i-1}}{\partial \hat{t}}\Big|_{l_{i-1}}\cos\beta_1 - \frac{\partial w_i}{\partial \hat{t}}\Big|_0\cos\beta_2\right) \\ &+ \left(p_{i-1} - v^2\right)l_t\frac{\partial w_{i-1}}{\partial \hat{x}_{i-1}}\Big|_{l_{i-1}}\cos\beta_1 - \left(p_i - v^2\right)l_t\frac{\partial w_i}{\partial \hat{x}_i}\Big|_0\cos\beta_2 = 0\end{aligned} \tag{3.18}$$

Equations (3.11)-(3.18) are given an extended operator form to allow the use of classical methods of analysis. The extended variable a is used to represent the system displacements

$$a = \left\{ \underbrace{w_{i-1}, w_i}_{spans}, \underbrace{\psi_2, \psi_3, \ldots, \psi_n}_{pulleys}, \underbrace{\theta_t}_{tensioner} \right\}^T \tag{3.19}$$

Note that, included in the definition of the extended variable a, are the continuum deflections of the two spans adjacent to the tensioner. The above equations can be written compactly by utilizing the extended operators M, G, K, and $\tilde{K}$ acting on the extended variable a.

$$M\frac{\partial^2 a}{\partial \hat{t}^2} - G\frac{\partial a}{\partial \hat{t}} + \left(K - v^2\tilde{K}\right)a = f \tag{3.20}$$

$$Ma = \left(w_{i-1}, w_i, \hat{J}_2\psi_2, \hat{J}_3\psi_3, \ldots, \hat{J}_n\psi_n, \hat{J}_t\theta_t\right)^T \tag{3.21}$$

$$Ga = \left(2v\frac{\partial w_{i-1}}{\partial \hat{x}_{i-1}}, 2v\frac{\partial w_i}{\partial \hat{x}_i}, \underbrace{0,0,\ldots,0}_{n-1}, vl_t w_i\big|_0 \cos\beta_2 - vl_t w_{i-1}\big|_{l_{i-1}} \cos\beta_1 \right)^T \tag{3.22}$$

$$Ka = \begin{pmatrix} -p_{i-1}\dfrac{\partial^2 w_{i-1}}{\partial \hat{x}_{i-1}^2} \\ -p_i \dfrac{\partial^2 w_i}{\partial \hat{x}_i^2} \\ \left(\dfrac{k_b}{l_2}+\dfrac{k_b}{l_1}\right)\psi_2 - \dfrac{k_b}{l_2}\psi_3 \\ \vdots \\ -\dfrac{k_b}{l_{j-1}}\psi_{j-1} + \left(\dfrac{k_b}{l_j}+\dfrac{k_b}{l_{j-1}}\right)\psi_j - \dfrac{k_b}{l_j}\psi_{j+1} \\ \vdots \\ -\dfrac{k_b}{l_{i-2}}\psi_{i-2} + \left(\dfrac{k_b}{l_{i-1}}+\dfrac{k_b}{l_{i-2}}\right)\psi_{i-1} - \dfrac{k_b}{l_{i-1}}\psi_i + \dfrac{k_b}{l_{i-1}} l_t\theta_t \sin\beta_1 \\ -\dfrac{k_b}{l_{i-1}}\psi_{i-1} + \left(\dfrac{k_b}{l_i}+\dfrac{k_b}{l_{i-1}}\right)\psi_i - \dfrac{k_b}{l_i}\psi_{i+1} - \left(\dfrac{k_b}{l_{i-1}}\sin\beta_1 + \dfrac{k_b}{l_i}\sin\beta_2\right) l_t\theta_t \\ -\dfrac{k_b}{l_i}\psi_i + \left(\dfrac{k_b}{l_{i+1}}+\dfrac{k_b}{l_i}\right)\psi_{i+1} - \dfrac{k_b}{l_{i+1}}\psi_{i+2} + \dfrac{k_b}{l_i} l_t\theta_t \sin\beta_2 \\ \vdots \\ -\dfrac{k_b}{l_{n-1}}\psi_{n-1} + \left(\dfrac{k_b}{l_n}+\dfrac{k_b}{l_{n-1}}\right)\psi_n \\ \begin{bmatrix} \left(k_t + \dfrac{k_b}{l_{i-1}}\sin^2\beta_1 + \dfrac{k_b}{l_i}\sin^2\beta_2\right) l_t^2\theta_t + p_{i-1} l_t \dfrac{\partial w_{i-1}}{\partial \hat{x}_{i-1}}\Big|_{l_{i-1}} \cos\beta_1 - p_i l_t \dfrac{\partial w_i}{\partial \hat{x}_i}\Big|_0 \cos\beta_2 \\ -\dfrac{k_b}{l_{i-1}} l_t(\psi_i - \psi_{i-1})\sin\beta_1 + \dfrac{k_b}{l_i}(\psi_{i+1} - \psi_i)\sin\beta_2 \end{bmatrix} \end{pmatrix} \tag{3.23}$$

$$\tilde{K}a = \left(-\frac{\partial^2 w_{i-1}}{\partial \hat{x}_{i-1}^2}, -\frac{\partial^2 w_i}{\partial \hat{x}_i^2}, \underbrace{0,0,\ldots,0}_{n-1}, l_t \frac{\partial w_{i-1}}{\partial \hat{x}_{i-1}}\Big|_{l_{i-1}} \cos\beta_1 - l_t \frac{\partial w_i}{\partial \hat{x}_i}\Big|_0 \cos\beta_2 \right)^T \tag{3.24}$$

$$f = \left(0,0,\hat{J}_2\ddot{\theta}_1 - q_2, \hat{J}_3\ddot{\theta}_1 - q_3, \ldots, \hat{J}_n\ddot{\theta}_1 - q_n, 0\right)^T \tag{3.25}$$

The inner product between two extended variables y and z, as shown by Parker [22], is defined as:

$$\langle y, z\rangle = \int_0^{l_{i-1}} y_1 \bar{z}_1 d\hat{x}_{i-1} + \int_0^{l_i} y_2 \bar{z}_2 d\hat{x}_i + y_3 \bar{z}_3 + \ldots + y_{n+2}\bar{z}_{n+2} \tag{3.26}$$

where y_r and z_r are elements of the extended variables y and z, and the overbar signifies the complex conjugate. With this inner product, the extended operators M, K, and $\widetilde{K}$ are self-adjoint, however G is skew self-adjoint. In addition, M and K are positive-definite and $\widetilde{K}$ is positive semi-definite.

Using a separable solution of the form $a \rightarrow ae^{i\omega t}$, the resulting eigenvalue problem is:

$$-\omega^2 Ma - i\omega Ga + La = 0 \tag{3.27}$$

where $L = K - v^2\widetilde{K}$ and here ω represents the dimensionless natural frequency. With the separable solution above, the component equations of the eigenvalue problem are obtained from equations (3.11)-(3.18). The dimensionless natural frequencies obtained from solution of equation (3.27) are related to the dimensional ones using the relation

$$\omega_n = \omega\sqrt{\frac{P_1}{\rho L_1^2}} \tag{3.28}$$

3.1.2 Equilibrium Analysis

The following equilibrium analysis, to determine the steady state span tensions and tensioner arm position, is based on the work of Beikmann et al. [16]. The first step is to calculate the initial static tension, P_0, and the reference belt length, $L_{reference}$. Initial static tension is calculated using equation (2.19) where, based on the model of Fig. 3.1, Q_t must be assigned a negative value as the tensioner torque acts to generate a clockwise motion of the tensioner arm about its pivot. The reference belt length is calculated as follows:

$$L_{reference} = \sum_{j=1}^{n}\left(L_{reference_j} + R_j\phi_{reference_j}\right) \tag{3.29}$$

where, $L_{reference_j}$ is the reference length of the j^{th} span at zero belt velocity and zero accessory torques, n is the number of pulleys, and $\phi_{reference_j}$ is the reference wrap angle of the belt on the j^{th} pulley.

The operating tension is defined here as:

$$P_j = P_{tj} + P_c \tag{3.30}$$

where, P_{tj} is the tractive tension in the j^{th} span, and $P_c = \rho V^2$ is the centrifugal tension component which is uniform throughout the system. Tractive tension is the tension component that provides the normal contact force of the belt on the pulley that is necessary drive each accessory. Equilibrium for the pulleys is defined by:

$$\begin{aligned}
&(P_7 - P_1)R_1 + Q_1 = 0 \\
&(P_1 - P_2)R_2 + Q_2 = 0 \\
&(P_2 - P_3)R_3 + Q_3 = 0 \\
&\qquad\vdots \\
&(P_6 - P_7)R_7 + Q_7 = 0
\end{aligned} \tag{3.31}$$

Equilibrium for the tensioner arm is defined by:

$$P_{t6}L_t \sin\beta_1 - P_{t7}L_t \sin\beta_2 + Q_t - K_t(\theta_t - \theta_0) = 0 \tag{3.32}$$

Now that equilibrium for each of the unknowns is defined, the solution of the equations is computed numerically. This is completed by first making an initial guess for the operating position of the tensioner. Based on this guess, the operating belt length is calculated using:

$$L_{operating} = \sum_{j=1}^{n} \left(L_{operating_j} + R_j \phi_{operating_j} \right) \tag{3.33}$$

where, $L_{operating_j}$ is the operating length of the j^{th} span, n is the number of pulleys, and $\phi_{operating_j}$ is the operating wrap angle of the belt on the j^{th} pulley. The difference between equations (3.29) and (3.33) is the belt deflection from the reference state to the operating state as calculated by geometry. In order to determine if the guess for θ_t is correct; the difference between $L_{reference}$ and $L_{operating}$ must now be compared against the deflection allowed by Hooke's Law.

To apply Hooke's law, the belt tensions must be computed based upon the assumed tensioner arm position. By rearranging equation (3.32), and noting that Q_7 equals zero in equation (3.31), the tractive tensions in the spans adjacent to the tensioner are calculated as:

$$P_{t6} = P_{t7} = \frac{K_t(\theta_t - \theta_0) - Q_t}{L_t(\sin\beta_1 - \sin\beta_2)} \tag{3.34}$$

Using this result, the tractive tensions of spans 6 and 7 are substituted into equation (3.30) to find the operating tensions which are then back-substituted into equation (3.31) to calculate the remainder of the span operating tensions.

As assumed in Chapter 2, the average tension over the contact arc of the pulley is taken as the average tension between the two spans adjacent to the pulley. Using this simplification, the elongation due to Hooke's law is calculated as:

$$\Delta L = \frac{1}{EA} \sum_{j=1}^{n} \left[L_{operating_j} \left(P_0 - P_j \right) + R_j \phi_{operating_j} \left(P_0 - \tfrac{1}{2} \{ P_j + P_{j-1} \} \right) \right] \tag{3.35}$$

where, ΔL is the elongation of the belt. Note that the subscript $_{j-1}$ becomes $_n$ when j=1. In addition, since the term K_{pj} is not utilized within this formulation as it is in Chapter 2, the $\frac{1}{2}\{P_j + P_{j-1}\}$ term is necessary to calculate the average tension over the contact arc of the pulley.

If the initial guess for θ_t is correct, then the following equation should be satisfied:

$$L_{reference} - L_{operating} = \Delta L \tag{3.36}$$

If equation (3.36) is not satisfied, a new guess for θ_t is made and the procedure is repeated. The solution method consists of adjusting θ_t until equation (3.36) is satisfied. By substituting equations (3.29), (3.33), and (3.35) into equation (3.36), a single nonlinear algebraic equation, which is dependent upon θ_t, is produced. Applying a standard secant method, the solution can be determined; typically within five iterations.

3.1.3 Discretization of the Belt Spans

A local discretization of solely the spans adjacent to the tensioner is implemented due to the fact that global discretization of the entire system is not possible for the reasons explained by Parker [22]. With the local discretization, the deflections of the two spans adjacent to the tensioner are represented in a series of basis functions as

$$\begin{aligned} w_{i-1}(\xi_{i-1},\hat{t}) &= \sum_{r=1}^{f} a_r(\hat{t})\alpha_r(\xi_{i-1}), \\ w_i(\xi_i,\hat{t}) &= \sum_{r=1}^{f} b_r(\hat{t})\gamma_r(\xi_i) \end{aligned} \tag{3.37}$$

where, f represents the number of basis functions used, $\xi_{i-1} = \hat{x}_{i-1}/l_{i-1}$ and $\xi_i = \hat{x}_i/l_i$. The non-dimensional basis functions, α_r and γ_r, satisfy the zero boundary conditions

($\alpha_r(0)=0$ and $\gamma_r(1)=0$) at the bounding points away from the tensioner where $\xi_{i-1}=0$ and $\xi_i=1$; shown in Fig. 3.2. The α_r and γ_r are not constrained by any boundary conditions at the span endpoints in contact with the tensioner arm where $\xi_{i-1}=1$ and $\xi_i=0$.

The basis functions are chosen to be orthonormal polynomials since the eigenfunctions of Sturm-Liouville problems have the general property of being orthogonal to one another. The model of the vibrating elastic string employed here falls under the Sturm-Liouville classification; so the basis functions used to represent the mode shapes must be an orthogonal set of functions as well. As a result, the basis functions are determined by

$$\begin{aligned}\int_0^1 \alpha_r \alpha_s d\xi_{i-1} &= \delta_{rs} \\ \int_0^1 \gamma_r \gamma_s d\xi_i &= \delta_{rs}\end{aligned} \tag{3.38}$$

where, δ_{rs} represents the Kronecker delta. These functions can be represented in terms of orthogonal polynomials $\mu_m(\xi)$ with $\int_0^1 \mu_r(\xi)\mu_s(\xi)d\xi = \begin{cases}0\ldots r\neq s\\ 1\ldots r=s\end{cases}$ as the following

$$\begin{aligned}\alpha_m(\xi_{i-1}) &= \mu_m(\xi_{i-1})/\sqrt{l_{i-1}} \\ \gamma_m(\xi_i) &= \mu_m(1-\xi_i)/\sqrt{l_i}\end{aligned} \tag{3.39}$$

The first four $\mu_m(\xi)$ are provided by Parker [22] and shown in Fig. 3.3

$$\begin{aligned}\mu_1(\xi) &= \sqrt{3}\xi \\ \mu_2(\xi) &= 4\sqrt{5}\left(\xi^2 - 3/4\xi\right) \\ \mu_3(\xi) &= 15\sqrt{7}\left(\xi^3 - 4/3\xi^2 + 2/5\xi\right) \\ \mu_4(\xi) &= 168\left(\xi^4 - 15/8\xi^3 + 15/14\xi^2 - 5/28\xi\right)\end{aligned} \tag{3.40}$$

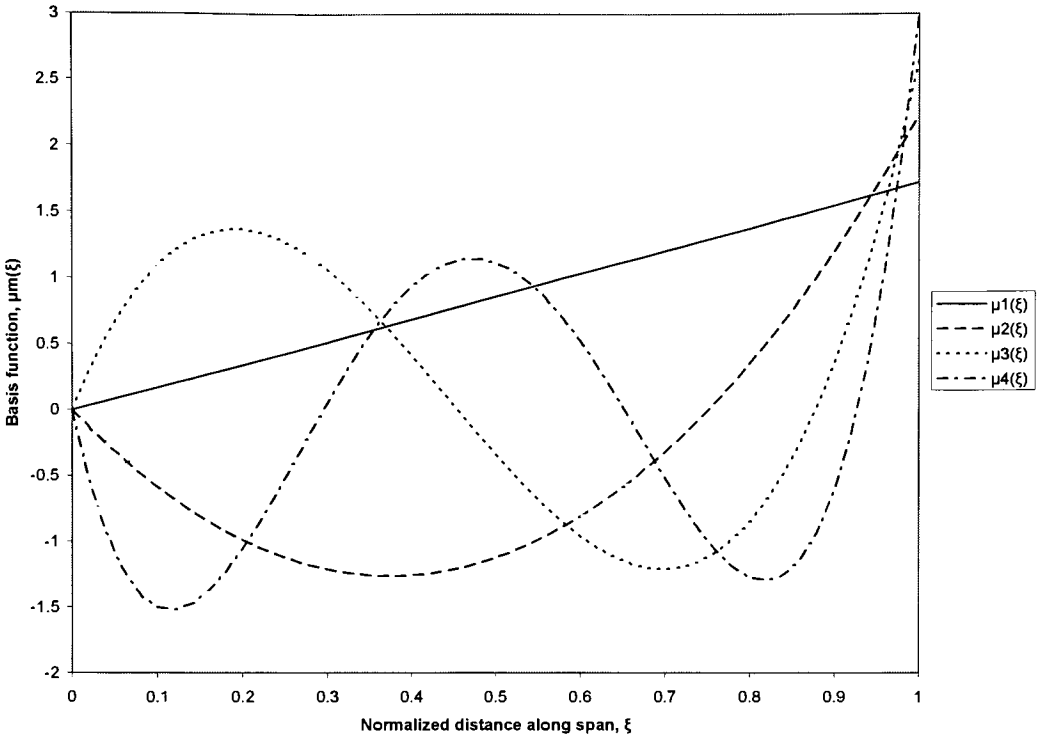

Figure 3.3 Basis functions $\mu_m(\xi)$ for the belt deflections

The kinetic and strain energies in dimensionless form are formulated as follows:

$$k.e. = \frac{K.E.}{\left(P_1 R_1^2 / L_1\right)} = \sum_{j=2}^{n} \frac{1}{2} \hat{J}_j \left(\dot{\psi}_j - \dot{\theta}_1\right)^2 + \frac{1}{2} \hat{J}_t \dot{\theta}_t^2 + \sum_{s=i-1}^{i} \frac{1}{2} \int_0^{l_s} \left(\frac{\partial w_s}{\partial \hat{t}} - v \frac{\partial w_s}{\partial \hat{x}_s} \right)^2 d\hat{x}_s$$
$$= \sum_{j=2}^{n} k.e._j + k.e._t + k.e._{span}^{i-1} + k.e._{span}^{i} \tag{3.41}$$

$$s.e. = \frac{S.E.}{\left(P_1 R_1^2 / L_1\right)} = \sum_{j=1, j\neq i-1, i}^{n} \frac{1}{2} \frac{k_b}{l_j} \left(\psi_{j+1} - \psi_j\right)^2 + \frac{1}{2} \frac{k_b}{l_{i-1}} \left(\psi_i - \psi_{i-1} - l_t \theta_t \sin\beta_1\right)^2$$
$$+ \frac{1}{2} \frac{k_b}{l_i} \left(\psi_{i+1} - \psi_i - l_t \theta_t \sin\beta_2\right)^2 + \frac{1}{2} k_t l_t^2 \theta_t^2 + \sum_{s=i-1}^{i} \frac{1}{2} \int_0^{l_s} p_s \left(\frac{\partial w_s}{\partial \hat{x}_s} \right)^2 d\hat{x}_s \tag{3.42}$$
$$= s.e._{stretch} + s.e._t + s.e._{span}^{i-1} + s.e._{span}^{i}$$

Employing Lagrange's equations permits the use of a minimum number of variables while eliminating constraint forces from the system [25]. The dynamic response of the system is determined using Lagrange multipliers to set up the dimensionless Lagrange's equations

$$\frac{\mathrm{d}}{\mathrm{d}\hat{t}} \left(\frac{\partial L}{\partial \dot{u}_s} \right) - \frac{\partial L}{\partial u_s} = \lambda_1 A_{1s} + \lambda_2 A_{2s}, s = 1,2,\ldots,2f+n \tag{3.43}$$

where $L = k.e. - s.e.$ and where λ_1 and λ_2 are the dimensionless boundary forces required to enforce the boundary conditions at the tensioner end of the spans [22]. The boundary conditions of equation (3.13) are the basis for the holonomic constraints on the generalized coordinates $a_r(t)$, $b_r(t)$, and $\theta_t(t)$. The transformed boundary conditions are

$$\Phi_1 = w_{i-1}\big|_{l_{i-1}} - l_t \theta_t \cos\beta_1 = \sum_{r=1}^{f} a_r(t)\alpha_r(1) - l_t \theta_t \cos\beta_1 = 0$$
$$\Phi_2 = w_i\big|_0 - l_t \theta_t \cos\beta_2 = \sum_{r=1}^{f} b_r(t)\gamma_r(0) - l_t \theta_t \cos\beta_2 = 0 \tag{3.44}$$

In equation (3.43), the A_{1s} and A_{2s} terms are the coefficients of the s^{th} generalized coordinate in the constraints Φ_1 and Φ_2, respectively. Here, $A_{1s} = \partial\Phi_1 / \partial u_s$ and $A_{2s} = \partial\Phi_2 / \partial u_s$, where the generalized coordinates u_s are ordered as $a_1,\ldots,a_f,b_1,\ldots,b_f,\psi_2,\ldots,\psi_n,\theta_t$. As a result,

$$\left.\begin{aligned} A_{1s} &= \alpha_s(1) \\ A_{2s} &= 0 \end{aligned}\right\} s = 1,2,\ldots,f,$$
$$\left.\begin{aligned} A_{1s} &= 0 \\ A_{2s} &= \gamma_s(0) \end{aligned}\right\} s = f+1, f+2,\ldots,2f$$
$$\left.\begin{aligned} A_{1s} &= 0 \\ A_{2s} &= 0 \end{aligned}\right\} s = 2f+1,2f+2,\ldots,2f+n-1 \qquad (3.45)$$
$$A_{1(2f+n)} = -l_t \cos\beta_1$$
$$A_{2(2f+n)} = -l_t \cos\beta_2$$

Using Lagrange's equations (3.43), the $2f$ equations for the span generalized coordinates become

$$\begin{aligned} \ddot{a}_r - \frac{v}{l_{i-1}} \sum_{s=1}^{f} G_{rs}^{span} \dot{a}_s + \frac{p_{i-1} - v^2}{l_{i-1}^2} \sum_{s=1}^{f} K_{rs}^{span} a_s &= \lambda_1 A_{1r} + \lambda_2 A_{2r} \\ \ddot{b}_r - \frac{v}{l_i} \sum_{s=1}^{f} G_{rs}^{span} b_s + \frac{p_i - v^2}{l_i^2} \sum_{s=1}^{f} K_{rs}^{span} b_s &= \lambda_1 A_{1(f+r)} + \lambda_2 A_{2(f+r)}, r = 1,2,\ldots,f \end{aligned} \qquad (3.46)$$

$$\begin{aligned} G_{rs}^{span} &= \int_0^1 \left(\mu_r \frac{\mathrm{d}\mu_s}{\mathrm{d}\xi} - \mu_s \frac{\mathrm{d}\mu_r}{\mathrm{d}\xi} \right) d\xi = -G_{sr}^{span} \\ K_{rs}^{span} &= \int_0^1 \frac{\mathrm{d}\mu_r}{\mathrm{d}\xi} \frac{\mathrm{d}\mu_s}{\mathrm{d}\xi} d\xi = K_{sr}^{span} \end{aligned} \qquad (3.47)$$

where G_{rs}^{span} represents the discretized form of the Coriolis acceleration term $2\rho V \dfrac{\partial^2 W_j}{\partial x \partial t}$ from equation (3.1). Now that the span equations have been discretized, the equations of

motion can be put into matrix form for solution using standard techniques. The equations for the pulley rotations remain as they are in equations (3.14)-(3.17). The tensioner equation must adopt two modifications. First, equation (3.37) is substituted for the span deflections. Second, the right-hand side becomes $\lambda_1(-l_t\cos\beta_1)+\lambda_2(-l_t\cos\beta_2)$. The resulting matrix equation is

$$\begin{bmatrix}\mathbf{M}_{11} & 0\\ 0 & 0\end{bmatrix}\begin{Bmatrix}\ddot{\mathbf{h}}\\ \ddot{\lambda}\end{Bmatrix}-\begin{bmatrix}\mathbf{G}_{11} & 0\\ 0 & 0\end{bmatrix}\begin{Bmatrix}\dot{\mathbf{h}}\\ \dot{\lambda}\end{Bmatrix}+\begin{bmatrix}\mathbf{L}_{11} & \mathbf{L}_{12}\\ \mathbf{L}_{12}^T & 0\end{bmatrix}\begin{Bmatrix}\mathbf{h}\\ \lambda\end{Bmatrix}=\begin{Bmatrix}\mathbf{f}_1\\ \mathbf{0}\end{Bmatrix} \tag{3.48}$$

$$\mathbf{h}=\left\{\underbrace{a_1,a_2,\ldots,a_f,b_1,b_2,\ldots,b_f}_{spans},\underbrace{\psi_2,\psi_3,\ldots,\psi_n}_{pulleys},\underbrace{\theta_t}_{tensioner}\right\}^T \tag{3.49}$$

$$\lambda=\begin{Bmatrix}\lambda_1\\ \lambda_2\end{Bmatrix}$$

$$
\mathbf{M}_{11} = \begin{bmatrix} \mathbf{I}_{f\times f} & \mathbf{0} & \mathbf{0} & 0 \\ \mathbf{0} & \mathbf{I}_{f\times f} & \mathbf{0} & 0 \\ \mathbf{0} & \mathbf{0} & diag(\hat{J}_j) & 0 \\ 0 & 0 & 0 & 0 \end{bmatrix}
$$

$$
\mathbf{G}_{11} = v\begin{bmatrix} (1/l_{i-1})\mathbf{G}^{span} & \mathbf{0} & \mathbf{0} & \mathbf{0} \\ \mathbf{0} & (1/l_i)\mathbf{G}^{span} & \mathbf{0} & \mathbf{0} \\ \mathbf{0} & \mathbf{0} & \mathbf{0} & \mathbf{0} \\ \mathbf{G}^{t(i-1)} & \mathbf{G}^{t(i)} & \mathbf{0} & 0 \end{bmatrix}
$$

$$
\mathbf{L}_{11} = \begin{bmatrix} \dfrac{p_{i-1}-v^2}{l_{i-1}^2}\mathbf{K}^{span} & \mathbf{0} & \mathbf{0} & \mathbf{0} \\ \mathbf{0} & \dfrac{p_i-v^2}{l_i^2}\mathbf{K}^{span} & \mathbf{0} & \mathbf{0} \\ \mathbf{0} & \mathbf{0} & \mathbf{K}^{pulley} & \mathbf{K}^{pt} \\ \mathbf{K}^{t(i-1)} & \mathbf{K}^{t(i)} & \mathbf{K}^{tp} & K^{tt} \end{bmatrix}
$$

$$
\mathbf{L}_{12} = \begin{bmatrix} A_{11} & A_{21} \\ A_{12} & A_{22} \\ \vdots & \vdots \\ A_{1(n+2f)} & A_{2(n+2f)} \end{bmatrix}
$$

$$
\mathbf{f}_1 = \left\{ \underbrace{0,\ldots,0}_{2f}, \hat{J}_2\ddot{\theta}_1 - q_2, \hat{J}_3\ddot{\theta}_1 - q_3, \ldots, \hat{J}_n\ddot{\theta}_1 - q_n, 0 \right\}^T \tag{3.50}
$$

The components of $\mathbf{G}^{span}$ and $\mathbf{K}^{span}$ are given in equation (3.47); the rest of the matrix components are provided in Appendix D.

Multiplying out the matrices of equation (3.48) yields

$$
\mathbf{M}_{11}\ddot{\mathbf{h}} - \mathbf{G}_{11}\dot{\mathbf{h}} + \mathbf{L}_{11}\mathbf{h} + \mathbf{L}_{12}\lambda = \mathbf{f}_1 \tag{3.51}
$$

The Lagrange multiplier λ can be removed by pre-multiplying the above equation by $\mathbf{C}^T$. $\mathbf{C}$ is such that $\mathbf{C}^T\mathbf{L}_{12} = 0$, which demands that the columns of $\mathbf{C}$ are a basis for the null space of $\mathbf{L}_{12}^T$. The $(n+2f)\times(n+2f-2)$ matrix $\mathbf{C}$ is formulated through singular

value decomposition. Making the substitution $\mathbf{h} = \mathbf{C}\mathbf{z}$ in equation (3.51), and pre-multiplying by $\mathbf{C}^T$, as needed to eliminate λ, yields

$$\begin{aligned}
&\mathbf{M}_{system}\ddot{\mathbf{z}} - \mathbf{G}_{system}\dot{\mathbf{z}} + \mathbf{L}_{system}\mathbf{z} = \mathbf{C}^T\mathbf{f}_1 = \mathbf{y} \\
&\mathbf{M}_{system} = \mathbf{C}^T\mathbf{M}_{11}\mathbf{C} \\
&\mathbf{G}_{system} = \mathbf{C}^T\mathbf{G}_{11}\mathbf{C} \\
&\mathbf{L}_{system} = \mathbf{C}^T\mathbf{L}_{11}\mathbf{C}
\end{aligned} \tag{3.52}$$

This is the final discretized form through which the dynamic response of the system to a specified input from the crankshaft can be determined. With the separable form $\mathbf{z} \rightarrow \mathbf{z}e^{i\omega t}$, the eigenvalues and eigenvectors can be calculated using the eigenvalue problem below

$$\left(-\omega^2\mathbf{M}_{system} - i\omega\mathbf{G}_{system} + \mathbf{L}_{system}\right)\mathbf{z} = \mathbf{0} \tag{3.53}$$

The system modes $\mathbf{h}$ are found from $\mathbf{h} = \mathbf{C}\mathbf{z}$; the span modal deflections are determined using $\mathbf{h}$ and equation (3.37). The non-dimensional natural frequencies are related to the dimensional ones using equation (3.28).

3.2 TRANSVERSE MOTION – FIXED-FIXED SPANS

The preceding formulation takes into account the transverse motion of the belt spans adjacent to the tensioner. As a result, it is not necessary to use an additional method to calculate the transverse vibration characteristics of those spans. However, as described previously in this chapter; for small belt motions, the linearized model decouples the transverse motion of all belt spans, except those adjacent to the tensioner, from the rotational motion of the pulleys. This statement is based on the assumption that there is no bending stiffness in the belt. Therefore, if the transverse natural frequencies of the spans between fixed pulleys are needed, the same procedure described in section 2.3 must be used to find the transverse natural frequencies of the fixed-fixed spans.

3.3 ALGORITHM FOR COUPLED SOLUTION

Presented below in Fig. 3.4 is a flow chart that outlines the procedure presented previously throughout Chapter 3 that one must follow to solve the coupled serpentine belt drive model. Results of the formulation include the operating belt tensions along with system natural frequencies and their corresponding mode shapes.

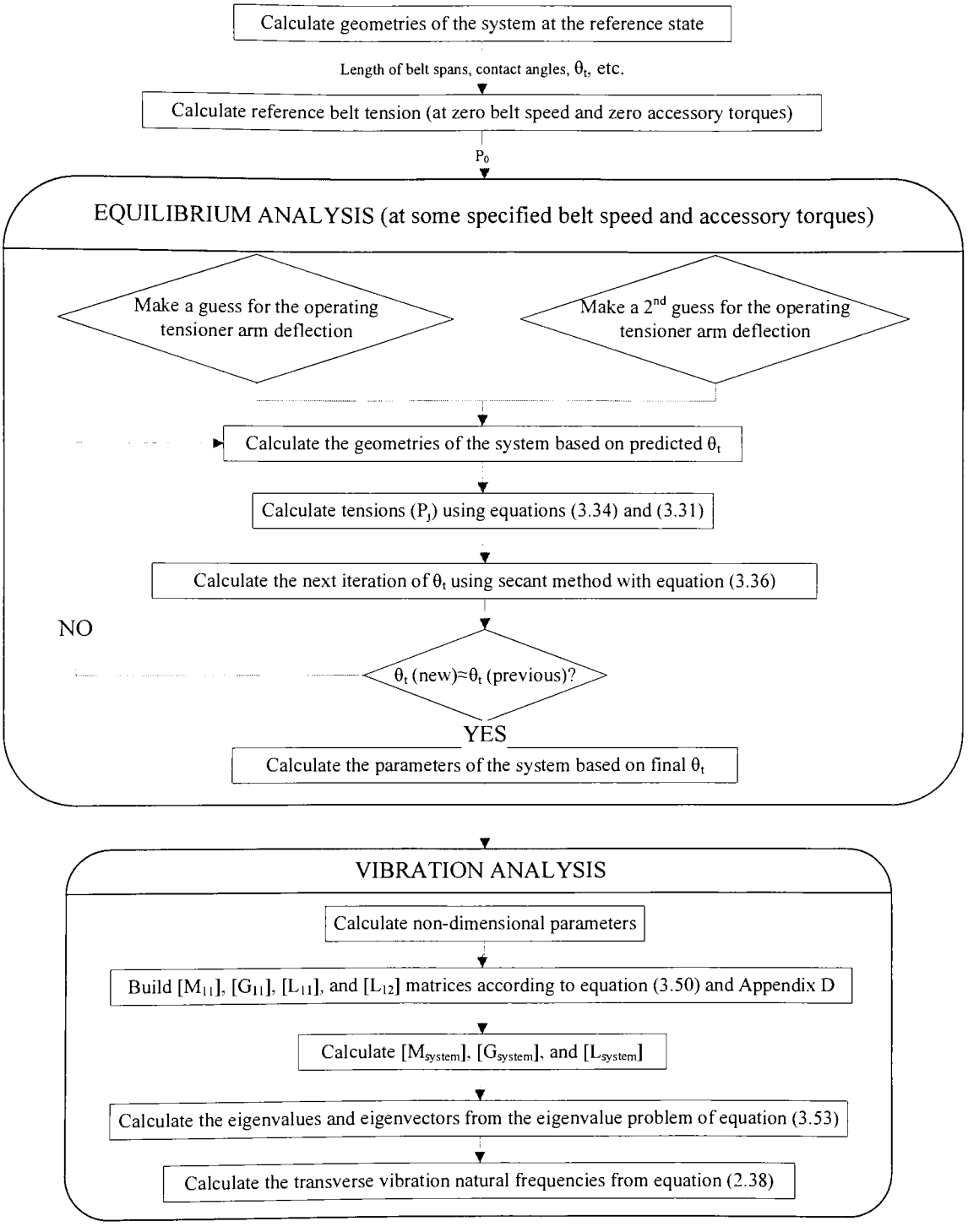

Figure 3.4 Algorithm for the coupled analysis

CHAPTER 4

CASE STUDIES – ANALYTICAL AND EXPERIMENTAL

This chapter presents three case studies that that are used to assess each of the two methods presented in Chapter 2 and Chapter 3 to accurately describe the equilibrium state and vibration characteristics of the systems. The first analytical case study is borrowed from Hwang et al. [7] and the results found here are compared against those published in the paper. The second analytical case study is borrowed from Parker [22] and the results found here are compared against those published in the paper. The third case study is based on experimental work completed by Beikmann et al. [13] and the results found here are validated by comparison against those published in the paper. A parametric study is completed to determine the effect of coupling on the accuracy of the results based on varying engine speed.

4.1 CASE STUDY 1 – ANALYTICAL

4.1.1 System Configuration

Data for an example serpentine belt drive system is presented in Table 4.1. The data is taken from Hwang et al. [7] who determined the values based on the setup of an actual engine. Most of the parameters can be calculated based on the geometry of the system. However, as described by Hwang et al., the parameters K_t and C_t were determined experimentally. Note that J_{7t} is included in the value of J_t.

4.1.2 Decoupled Results

4.1.2.1 Equilibrium

Tractive tension is the steady state tension component that is available to drive each pulley. The tractive tension is given by

Table 4.1 Dimensional specifications and load information: case 1

PULLEYS

Pulley # j	Type	X_j - Y_j Location (mm)	R_j (mm)	J_j (kg-m^2)	Q_j (Equil. Study) (N-m)	Q_j (Vibs. Study) (N-m)
1	C/S	(0, 0)	81.25	0.122		
2	A/C	(261.5, 60)	64.5	0.00415	-24.4	0
3	P/S	(252, 234)	70.6	0.00131	-24.4	-24.4
4	IDL	(90.3, 251.1)	41.15	0.000263	0	0
5	ALT	(86, 354)	30	0.00421	-8.13	0
6	W/P	(0, 167.5)	67.5	0.00176	-1.36	-1.36
7	TENS. Pulley	(151.2, 155.3)	38.1	0.000207	0	0

TENSIONER ARM

X_8 - Y_8 Location (mm)	θ_0 (deg)	J_t (kg-m^2)	g (m/s^2)	m_{eff} (kg)	EA (N)
(142, 207.5)	280	0.001424	0 (assumed)	0.458	80064
L_{eff} (mm)	L_t (mm)	Q_t (N-m)	C_t (N-m-s)	K_t (N-m/rad)	ρ (kg/m)
25	53	25.19	2.26	28.25	0.10687

$$P_j' = P_j - \rho V^2 \tag{4.1}$$

where ρV^2 represents the centrifugal belt tension as described previously. Tractive tensions are plotted in Fig. 4.1 for all seven belt spans over a range of steady belt speeds. The specified steady accessory torques are $Q_2 = Q_3 = -24.40$, $Q_4 = Q_7 = 0$, $Q_5 = -8.13$, and $Q_6 = -1.36$ (N-m). Note that since L_{eff} and m_{eff} are rarely provided in a given set of data for a system; the solution provided here ignores their effect by equating the gravitational constant (g) to zero. By setting $g = 0$, the weight term is eliminated and as a result, each of the case study dimensional specifications and solutions are further alike. Since the weight term is small, ignoring it does not affect the results.

From the plot in Fig. 4.1 it can be seen that the tractive tensions are equal for belt spans 3 and 4, and spans 6 and 7. This is due to the fact that no steady-state torque is applied at the idler and tensioner pulleys. In addition, it is apparent that the tractive tensions are speed dependent; however, this dependence is not overwhelmingly strong.

The tensioner arm angle at equilibrium is also a function of speed. As mentioned in Section 2.2, the tensioner will relax as a result of belt stretch at increasing speeds. Relaxation of the tensioner is indicated by an increase in tensioner arm angle (according to Fig. 2.1) as shown in Fig. 4.2. Notice that extrapolating the graph back to zero engine speed will not result in a tensioner arm angle that agrees with the reference tensioner arm angle of 280 degrees. The reason for this inconsistency is the accessory torque loading that is present when the belt is in motion. Recall that the reference state is defined by zero belt speed *and* zero accessory torques.

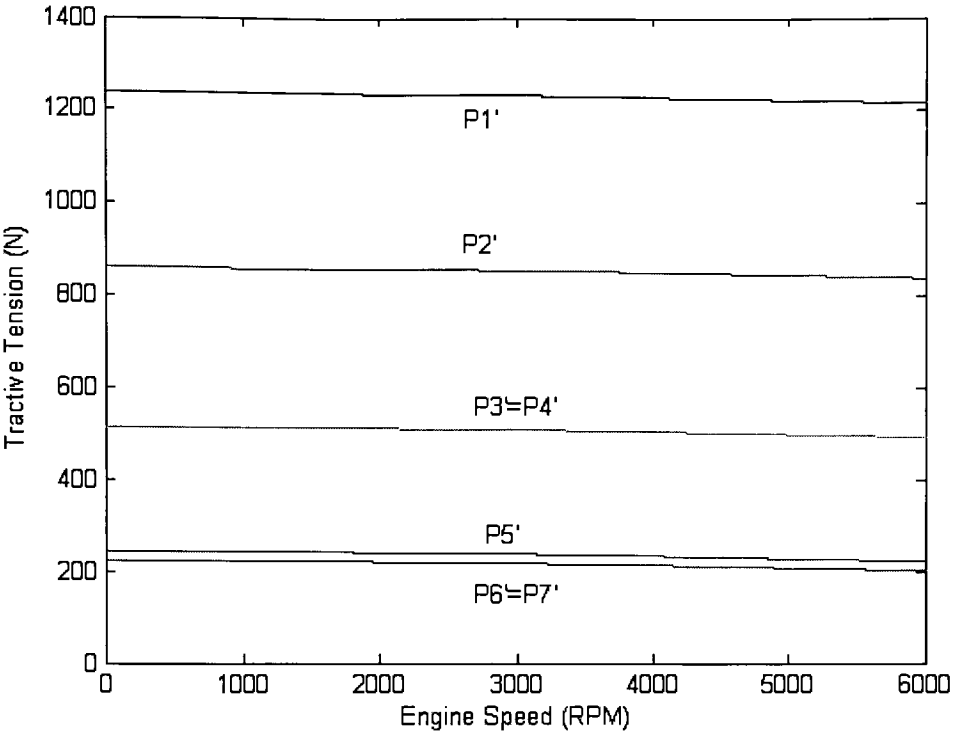

Figure 4.1 Steady-state tractive tensions: decoupled analysis, case 1

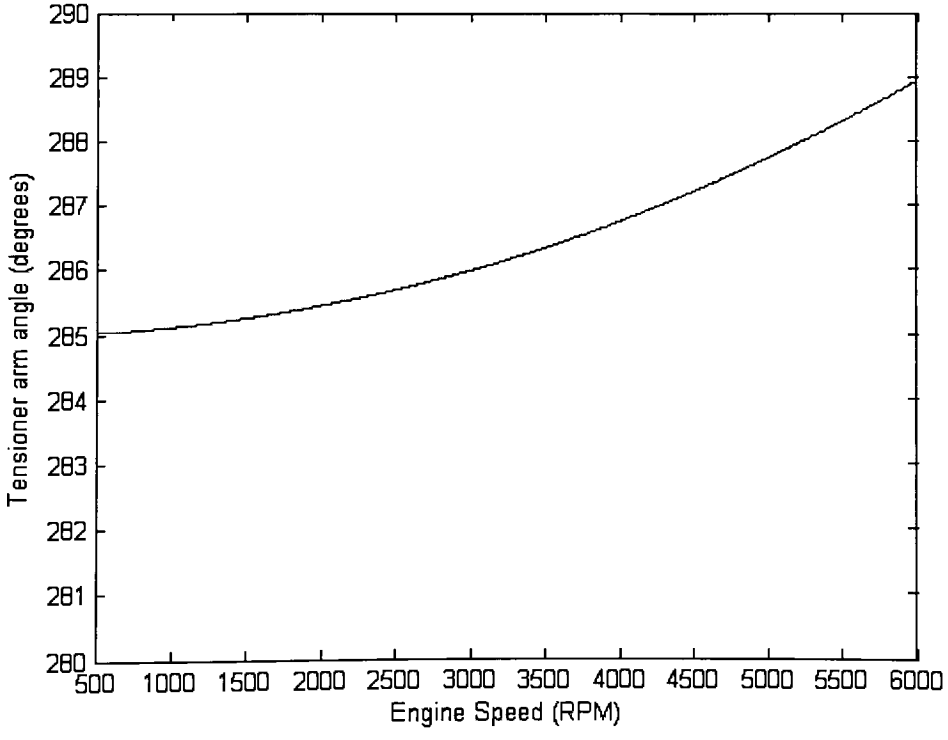

Figure 4.2 Equilibrium tensioner arm angle: decoupled analysis, case 1

4.1.2.2 Natural frequencies and mode shapes

The decoupled rotational vibration and transverse vibration of the spans adjacent to the tensioner, along with the spans bounded by fixed pulleys are now studied. Using the model described in Table 4.1, with accessory torques $Q_3 = -24.40$, $Q_6 = -1.36$, $Q_2 = Q_4 = Q_5 = Q_7 = 0$ (N-m), and $C_t = 0$, the natural frequencies are plotted as a function of engine speed (rpm) in Figs. 4.3, 4.4 and 4.5. Note that the effect of damping is removed by setting $C_t = 0$. This eliminates the discrepancy due to the difference in the assumptions between Chapter 2 and Chapter 3.

It is apparent from the figure that the natural frequencies of the rotational modes are essentially independent of engine speed. However, the natural frequencies of the transverse modes are strongly dependent upon belt speed. This result is expected in the spans adjacent to the tensioner, since the lengths of the spans increase as engine speed increases due to the relaxation of the tensioner arm. It can be seen from equation (2.36) that increasing the belt speed and belt length will result in decreasing natural frequencies. Similarly for the spans between fixed pulleys, increasing belt speed will decrease the natural frequency according to equation (2.38).

Natural frequencies and modes of the system are provided in Table 4.2 for the steady operating speed of 477.5 rpm and accessory torque loading described within this section. The "Mode" column describes the dominant type of vibration and the element of the system that is most affected at the corresponding frequency. Despite the reference to only one dominant element, all degrees of freedom for the system experience some vibration at each natural frequency.

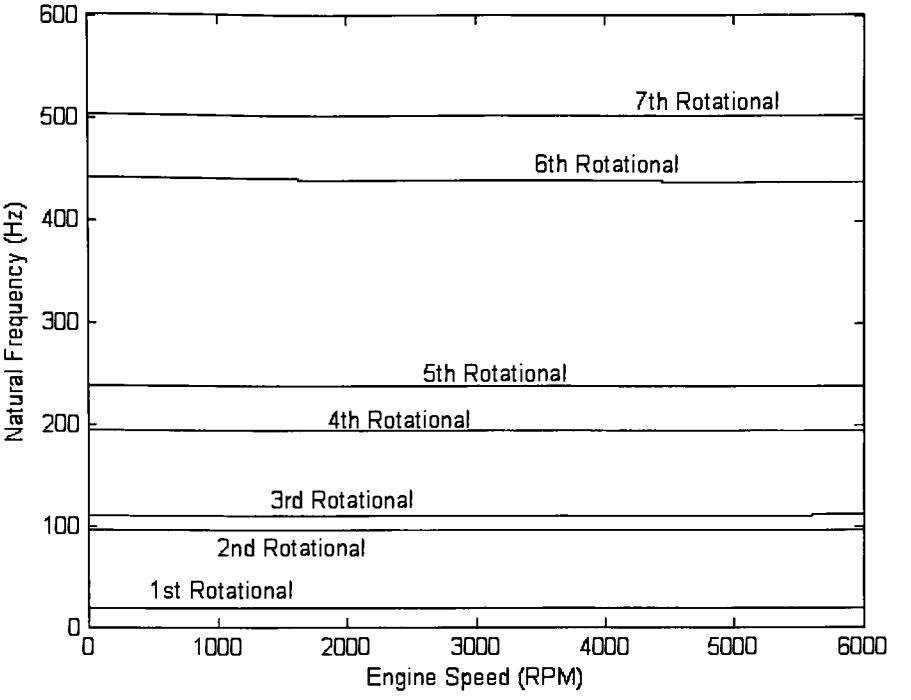

Figure 4.3 Rotational mode natural frequencies: decoupled analysis, case 1

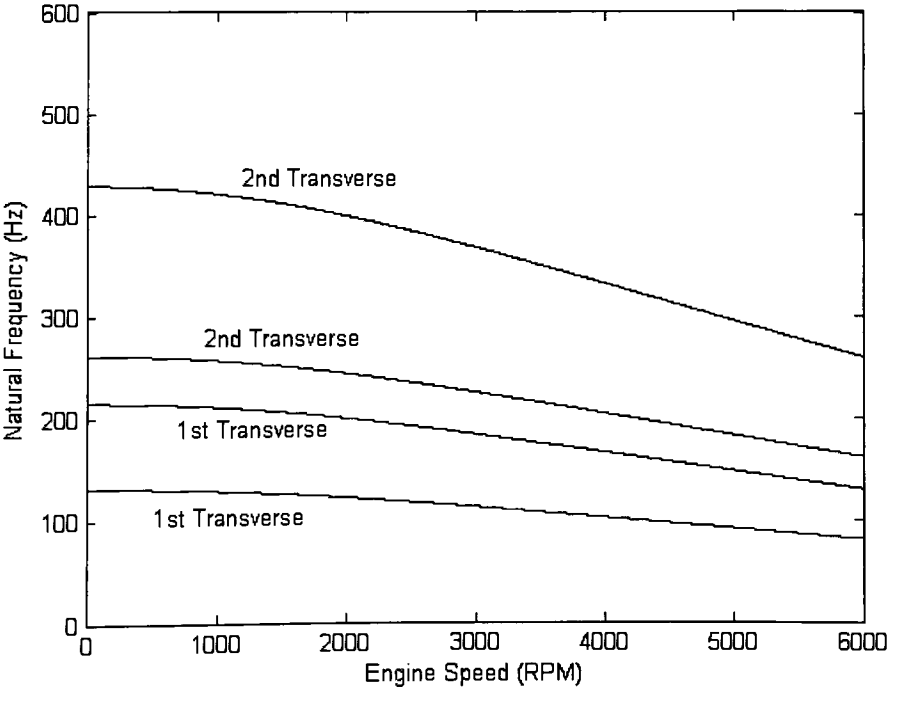

Figure 4.4 Transverse mode natural frequencies for spans adjacent to tensioner: decoupled analysis, case 1

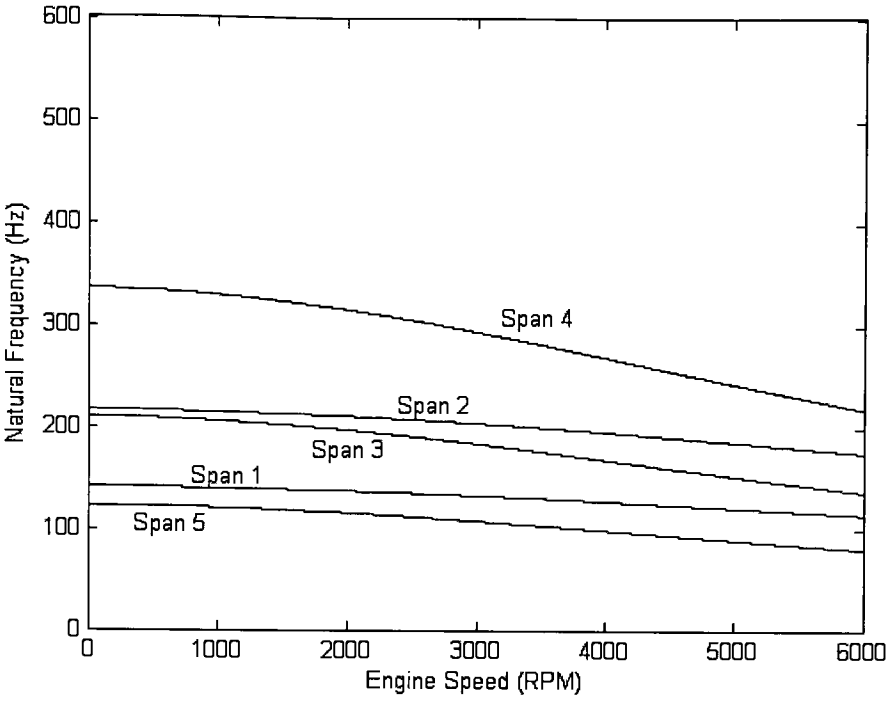

Figure 4.5 Transverse mode natural frequencies for the spans between fixed pulleys: decoupled analysis, case 1

Table 4.2 Natural frequencies and mode shapes: decoupled analysis, case 1, 477.5 rpm

CALCULATED RESULTS

Natural Frequency (Hz)	Mode
19.1	1st Rotational - Pulley 5
95.4	2nd Rotational - Pulley 2
109.8	3rd Rotational - Tensioner Arm
129.9	1st Transverse - Span 7
193.5	4th Rotational - Pulley 7
213.3	1st Transverse - Span 6
237.3	5th Rotational - Pulley 3
259.7	2nd Transverse - Span 7
426.5	2nd Transverse - Span 6
440.6	6th Rotational - Pulley 7
502.9	7th Rotational - Pulley 4

PUBLISHED RESULTS

Natural Frequency (Hz)	Mode
19.1	1st Rotational - Pulley 5
96.3	2nd Rotational - Pulley 2
103.7	3rd Rotational - Tensioner Arm
186.9	4th Rotational - Pulley 7/Tensioner
236.9	5th Rotational - Pulley 3
436.2	6th Rotational - Pulley 7
502.2	7th Rotational - Pulley 4

4.1.3 Coupled Results

4.1.3.1 Equilibrium

Using the same configuration and accessory torque loading as in Section 4.1.2.1, tractive tension is plotted in Fig. 4.6 for the coupled analysis. As in the decoupled analysis, the tractive tensions remain dependent upon engine speed; however, this dependence is weak. The tensioner arm angle is plotted against engine speed in Fig 4.7. As with the tractive tensions, the coupled analysis provides nearly identical results to the decoupled analysis. This result is expected as the two methods for finding equilibrium are based on the same principle.

4.1.3.2 Natural frequencies and mode shapes

Whereas the decoupled analysis requires separate calculation of the transverse vibration characteristics for the spans adjacent to the tensioner, the coupled analysis accounts for the motions within the formulation. As a result, when the eigenvalues are calculated using equation (3.53), the natural frequencies of all modes are described (except the transverse modes between fixed pulleys). The natural frequencies are plotted below as a function of engine speed in Figs. 4.8, 4.9, and 4.10.

The natural frequencies and modes of the system are described in Table 4.3 for the same conditions described in Section 4.1.2.2.

4.1.4 Comparison

Upon comparing the results presented here for the decoupled analysis with those offered by Hwang et al. [7], it is apparent that Hwang's et al. findings are indeed repeatable. This is evident in the fact that the trends predicted by Hwang et al. with respect to the tractive tensions and natural frequencies versus engine speed are matched by the results

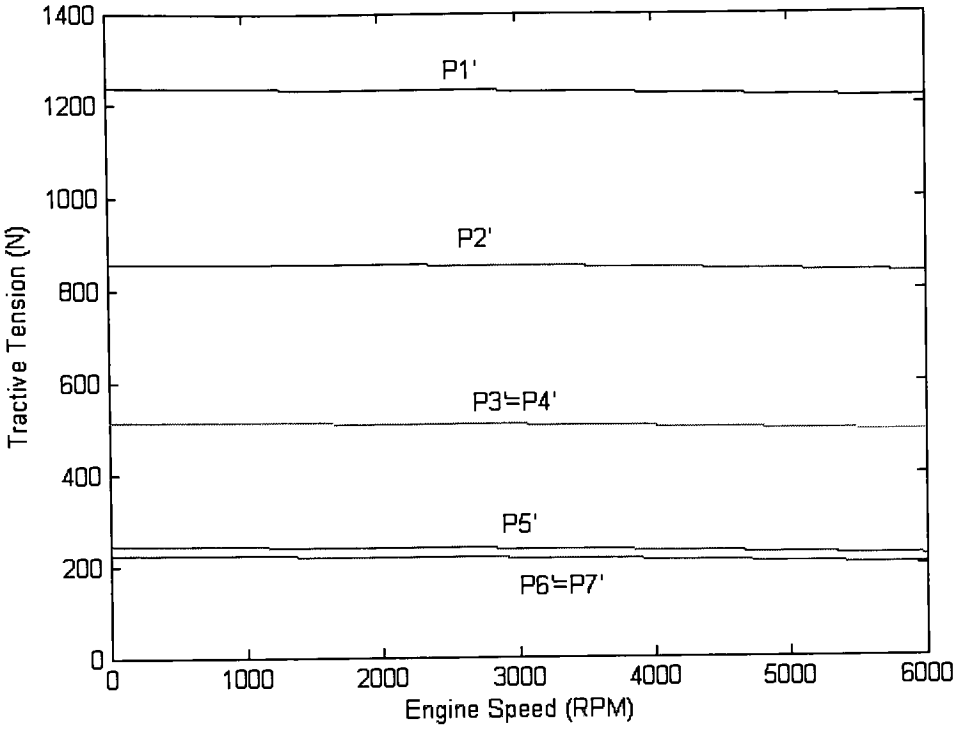

Figure 4.6 Steady-state tractive tensions: coupled analysis, case 1

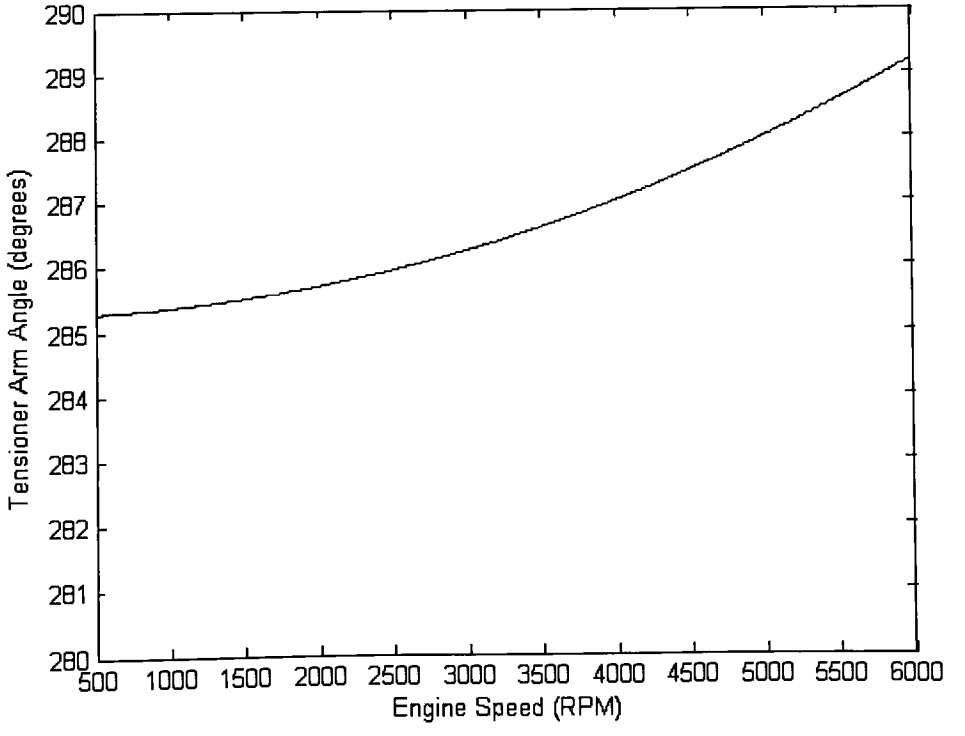

Figure 4.7 Equilibrium tensioner arm angle: coupled analysis, case 1

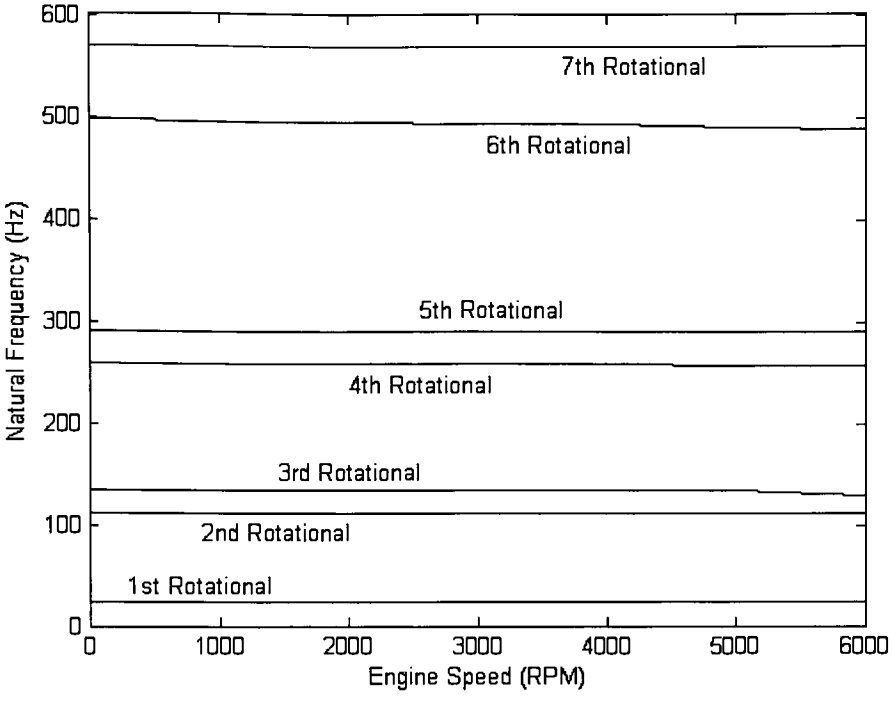

Figure 4.8 Rotational mode natural frequencies: coupled analysis, case 1

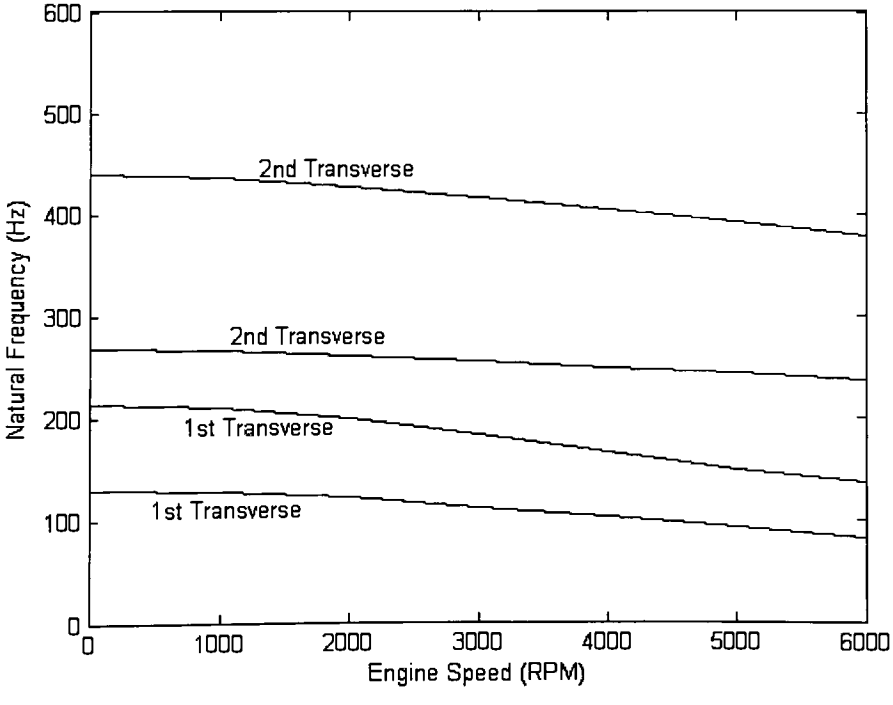

Figure 4.9 Transverse mode natural frequencies for spans adjacent to tensioner: coupled analysis, case 1

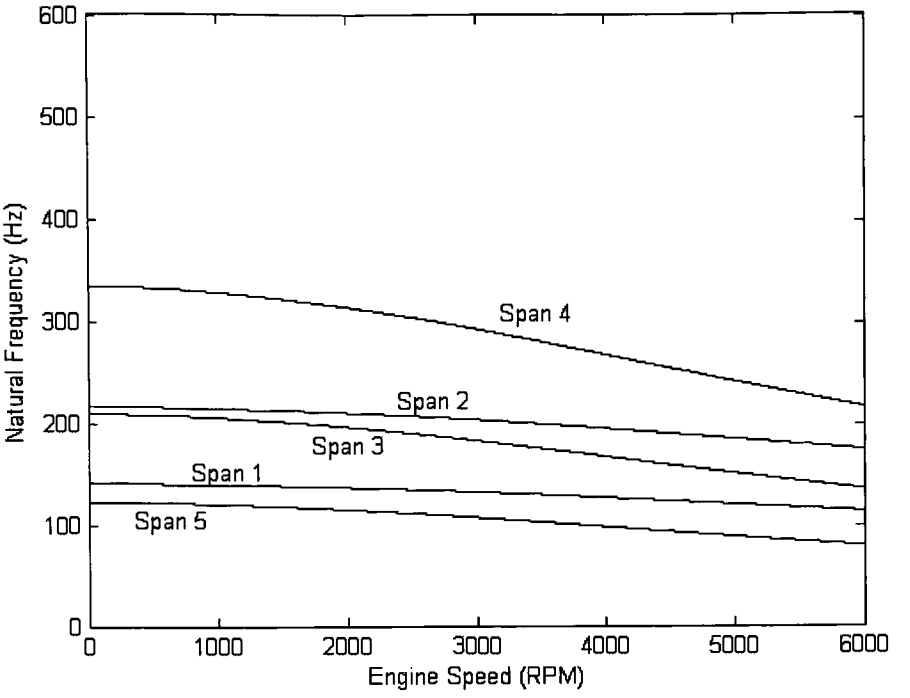

Figure 4.10 Transverse mode natural frequencies for the spans between fixed pulleys: coupled analysis, case 1

Table 4.3 Natural frequencies and mode shapes: coupled analysis, case 1, 477.5 rpm

Natural Frequency (Hz)	Mode
24	1st Rotational - Pulley 5
111.9	2nd Rotational - Pulley 2
129.3	1st Transverse - Span 7
134.8	3rd Rotational - Tensioner Arm
211.9	1st Transverse - Span 6
258.7	4th Rotational - Tensioner Arm
267.3	2nd Transverse - Span 7
290.3	5th Rotational - Pulley 3
438.4	2nd Transverse - Span 6
496.6	6th Rotational - Pulley 7
569.5	7th Rotational - Pulley 4

presented herein. In addition, the natural frequencies generally match to within a few percent. This result demonstrates that eliminating the weight term of the tensioner arm, as described previously, does not have a noticeable effect on the results. The corresponding modes predicted by Hwang et al. are reproduced here.

The results obtained using the decoupled analysis are compared to those of the coupled analysis by analyzing the values presented in Tables 4.2 and 4.3 along with the graphs in Figs. 4.3-4.5, and Figs. 4.8-4.10. Upon examining the natural frequencies of the rotationally dominant modes in Tables 4.2 and 4.3; it is apparent that the coupled and decoupled solutions produce decidedly different values. Even at the lower modes, the natural frequencies experience a 15-20% difference between the two methods. Examining the 4^{th} rotational mode (where the natural frequencies differ by the greatest amount), it is predicted by the coupled analysis that the tensioner arm is the dominant motion. However, the decoupled analysis predicts that pulley 7 experiences the largest amplitude vibration. Upon further examination it becomes unclear which is truly the dominant motion as both pulley 7 and the tensioner arm experience large vibrations. Recalling that since the "Modes" described in Tables 4.2 and 4.3 refer to the degree of freedom experiencing the *largest* vibration, it is possible that two elements of the system may be excited almost equally; which is the case for the 4^{th} rotational mode described here. Also, the coupled model captures an additional coupling of the motions among the tensioner arm, span 6, and pulley 6. This is evident by noticing in Figs. 4.8 and 4.9 that as the 1^{st} transverse mode approaches the frequency of the 3^{rd} rotational mode near 6000 rpm; the 3^{rd} rotational mode veers suddenly downward. This behavior demonstrates an interaction is occurring between the elements. This interaction is further exemplified by the mode shapes which indicate that all three of the elements mentioned previously experience similar large motions.

Due to the difficulty in comparing the eigenvectors qualitatively, the modal assurance criterion is introduced as a quantitative means to better assess the consistency between the two methods. As a measure of the least squares deviation of the points from the

straight line correlation [26], the modal assurance criterion compares the coupled and decoupled mode shapes at the rotationally dominant frequencies. Details are provided in Appendix E. The comparison yields a value between 0 and 1, where a value closer to 1 indicates similar mode shapes and 0 indicates dissimilar results. As applied here to this analysis, the modal assurance criterion compares only the rotational mode shapes between the methods. The values are given in Table 4.4, where it is shown that the 3rd and 4th rotational modes are inconsistent between the two methods. This discrepancy is remedied when the 3rd rotational mode shape of the coupled solution is compared with the 4th rotational mode shape of the decoupled model and visa versa. With this comparison, the modal assurance criterion improves to 0.748 and 0.842 for the 3rd and 4th modes respectively. With the convention that the natural frequencies are compared between modes with similar mode shapes, the coupled rotational natural frequency of the 3rd mode should be related to the decoupled rotational natural frequency of the 4th mode and visa versa. Using this rule the rotational natural frequencies differ by 50% between the two methods for the 3rd and 4th modes, further differentiating the solution techniques.

Despite the quantitative differences, both decoupled and coupled analyses show the same trend that indicates the rotational natural frequencies are relatively independent from engine speed.

Transverse natural frequencies of the spans adjacent to the tensioner are similar between the two methods. At the lower modes, the results are comparable to within 1.0%. However, for the higher modes, the results begin to diverge with increasing engine speed. At lower speeds, the results remain consistent between the methods. However, at higher speeds, natural frequencies for the 2nd modes differ by as much as 30%.

The spans bounded by fixed pulleys have identical transverse natural frequencies when calculated by both the coupled and decoupled models. This result is expected as these motions are completely decoupled in both methods and the technique to determine these frequencies is the same. The results are provided here for completeness.

Table 4.4 Modal assurance criterion values: case 1, 477.5 rpm

Rotational Mode	Modal Assurance Criterion
First Coupled, First Decoupled	0.834
Second Coupled, Second Decoupled	0.898
Third Coupled, Third Decoupled	0.003
Fourth Coupled, Fourth Decoupled	0.002
Fifth Coupled, Fifth Decoupled	0.923
Sixth Coupled, Sixth Decoupled	0.802
Seventh Coupled, Seventh Decoupled	0.989
Third Coupled, Fourth Decoupled	0.748
Fourth Coupled, Third Decoupled	0.842

4.2 CASE STUDY 2 – ANALYTICAL

4.2.1 System Configuration

Data for an example serpentine belt drive system is presented in Table 4.5. The data is taken from Parker [22] who obtained the values from a system in an automobile that was experiencing a vibration and noise problem. Parameters θ_0 and L_t were not provided directly by Parker but instead were calculated from the information given and the system geometry. In addition, m_{eff} and L_{eff} were not given by Parker; however, their effects are ignored nevertheless by setting $g = 0$ as in the previous analysis. Finally, J_{7t} is included in the value of J_t, and C_t is not utilized due the assumption that there is no damping within the system.

4.2.2 Decoupled Results

4.2.2.1 Equilibrium

Tractive tensions are plotted in Fig. 4.11 for all seven belt spans. As in case study 1, tractive tension does not change with increasing engine speed. Equilibrium tensioner arm angle is plotted in Fig. 4.12. Again, similar trends are seen here as in case study 1. In Fig 4.12, relaxation of the tensioner arm due to increasing engine speed is signified by a decrease in tensioner arm angle according to Fig. 3.1.

4.2.2.2 Natural frequencies and mode shapes

System natural frequencies are plotted in Figs. 4.13-4.15. The rotational natural frequencies remain constant with increasing engine speed. However, the transverse natural frequencies of the belt spans adjacent to the tensioner and those between fixed pulleys are highly dependent upon engine speed as seen in Figs. 4.14 and 4.15. Note that

Table 4.5 Dimensional specifications and load information: case 2

PULLEYS

Pulley # j	Type	X_j - Y_j Location (mm)	R_j (mm)	J_j (kg-m^2)	Q_j (N-m)
1	C/S	(0, 0)	97	0.122	
2	A/C	(211.6, 9)	62.5	0.003785	-24.82
3	ALT	(231.7, 189.8)	29.1	0.0043	-9.09
4	IDL	(79.6, 209.7)	40.75	0.00024	0
5	P/S	(-202.6, 269.9)	66.85	0.000596	-18.908
6	W/P	(-200, 100)	82.45	0.004596	-2.382
7	TENS. Pulley	(-45.1, 154.3)	37.75	0.000043	0

TENSIONER ARM

X_8 - Y_8 Location (mm)	θ_0 (deg)	J_t (kg-m^2)	g (m/s^2)	m_{eff} (kg)	EA (N)
(33, 137)	167.5	0.004601	0 (assumed)	0 (assumed)	111200
L_{eff} (mm)	L_t (mm)	Q_t (N-m)	C_t (N-m-s)	K_t (N-m/rad)	ρ (kg/m)
0 (assumed)	80	39.768	0	38.84	0.107

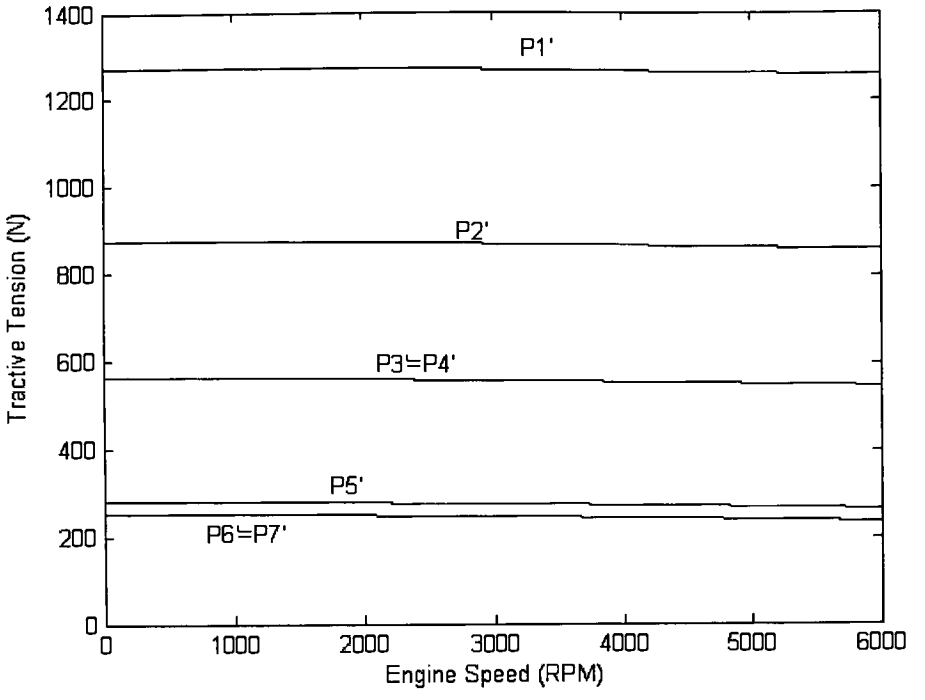

Figure 4.11 Steady-state tractive tensions: decoupled analysis, case 2

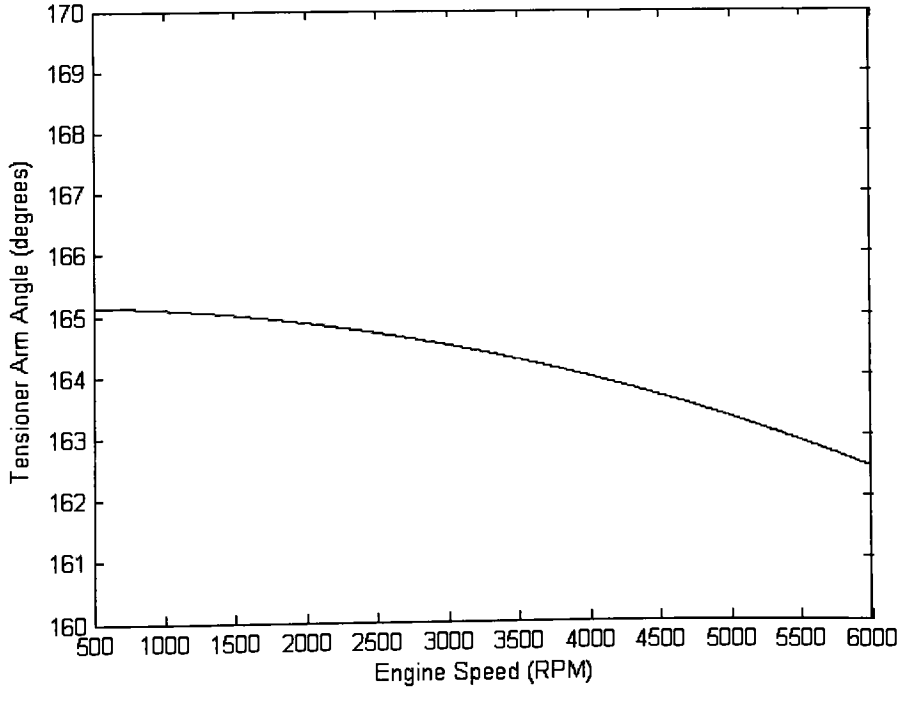

Figure 4.12 Equilibrium tensioner arm angle: decoupled analysis, case 2

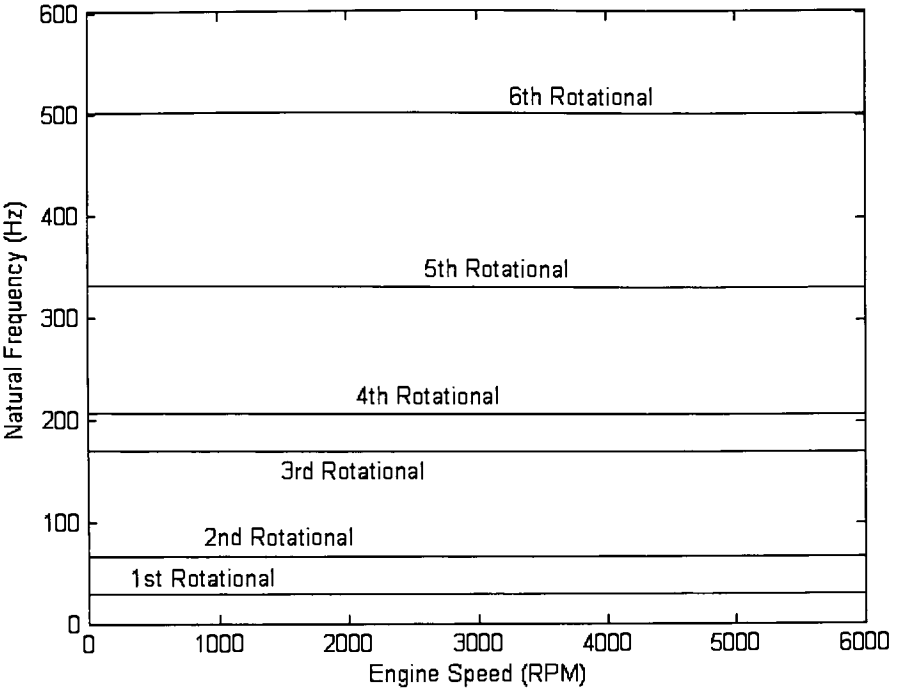

Figure 4.13 Rotational mode natural frequencies: decoupled analysis, case 2

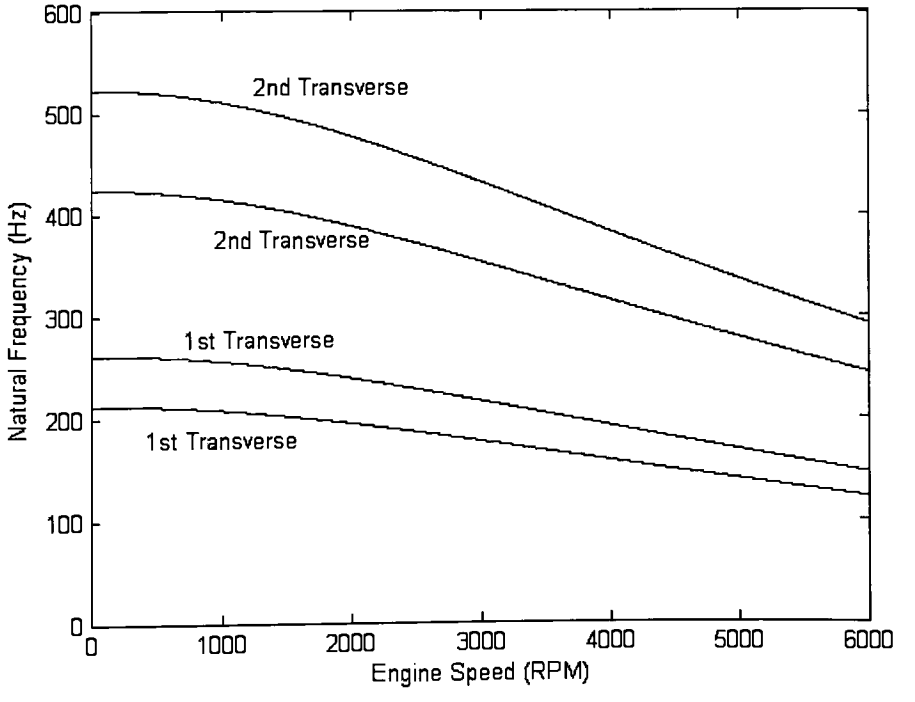

Figure 4.14 Transverse mode natural frequencies for spans adjacent to tensioner: decoupled analysis, case 2

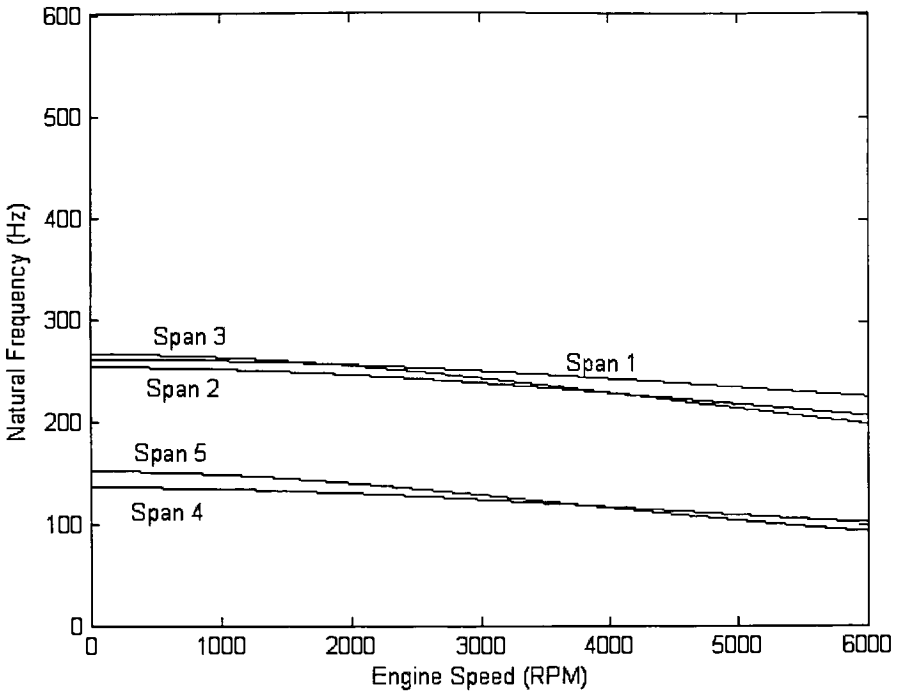

Figure 4.15 Transverse mode natural frequencies for the spans between fixed pulleys: decoupled analysis, case 2

the 7^{th} rotational mode is not plotted in Fig. 4.13 for the purpose of showing the behavior of the other modes more clearly.

For the steady operating speed of 680 rpm, the natural frequencies and mode shapes are given in Table 4.6.

4.2.3 Coupled Results

Results for the coupled analysis are presented in Figs. 4.16-4.20 and Table 4.7. Similar results as in Section 4.1.3 are seen. Parker's results are included in Table 4.7 for comparison.

4.2.4 Comparison

Results presented by Parker [22] are compared to the findings of the coupled analysis completed herein. Based on this comparison, it is determined that Parker's findings are indeed repeatable. This is shown by the fact that the equilibrium and vibration analysis results presented herein match those given by Parker to within a few percent.

As in Section 4.1.4, the results obtained from the decoupled analysis are compared to those found using the coupled analysis by analyzing the values presented in Tables 4.6 and 4.7 along with the graphs in Figs. 4.13-4.15, and Figs. 4.18-4.20. Upon examining the natural frequencies of the rotationally dominant modes in Tables 4.6 and 4.7; it is again apparent that the coupled and decoupled solutions produce distinctly different values. For all modes, the natural frequencies experience a 15-20% difference between the two methods. The modal assurance criterion reveals that the 2^{nd}, 3^{rd}, and 4^{th} rotational mode shapes are inconsistent between the two methods as shown in Table 4.8. Upon comparing the 2^{nd} rotational mode shape of the coupled analysis with the 4^{th} rotational mode shape of the decoupled analysis and visa versa; the modal assurance criterion improves to 0.586 and 0.401 respectively. Again using the convention that the

Table 4.6 Natural frequencies and mode shapes: decoupled analysis, case 2, 680 rpm

Natural Frequency (Hz)	Mode
28.4	1st Rotational - Pulley 3
65.0	2nd Rotational - Pulley 7
168.7	3rd Rotational - Pulley 2
205.8	4th Rotational - Pulley 5
209.7	1st Transverse - Span 6
258.5	1st Transverse - Span 7
330.7	5th Rotational - Pulley 4
419.4	2nd Transverse - Span 6
516.9	2nd Transverse - Span 7
500.1	6th Rotational - Pulley 4
1064.4	7th Rotational - Pulley 7

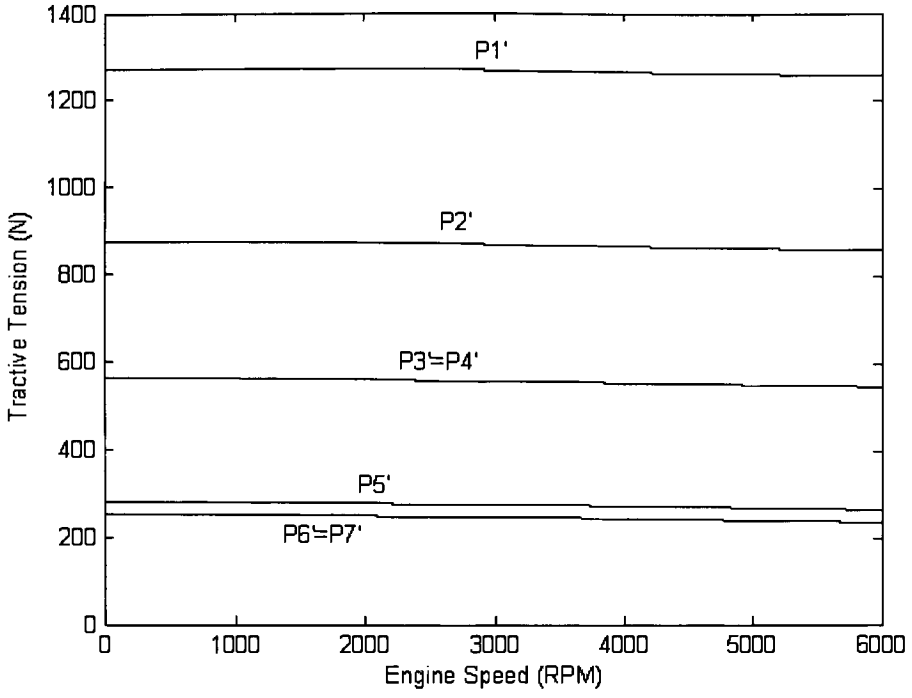

Figure 4.16 Steady-state tractive tensions: coupled analysis, case 2

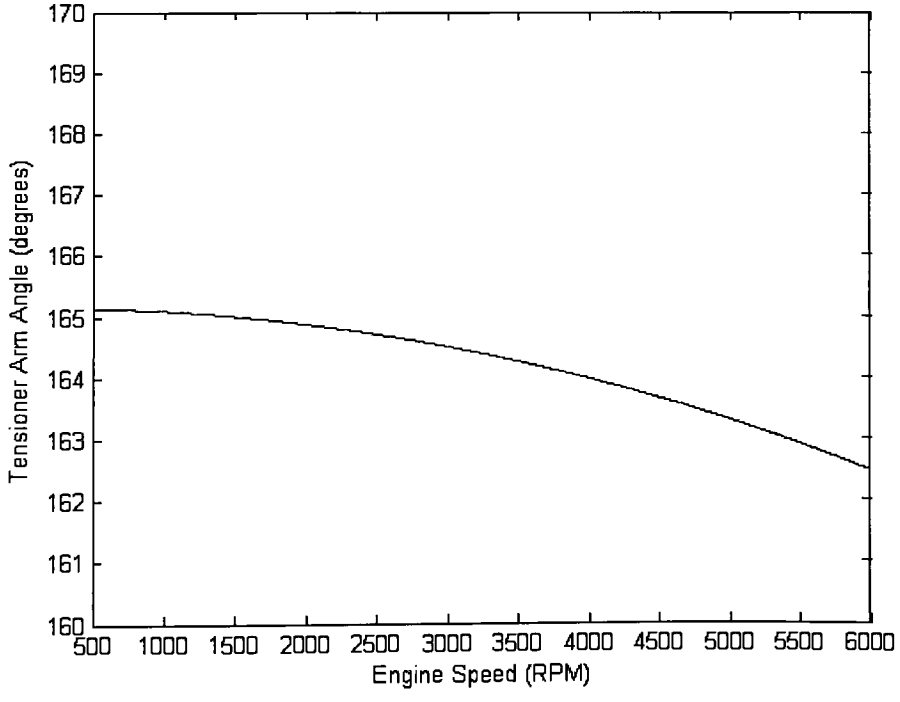

Figure 4.17 Equilibrium tensioner arm angle: coupled analysis, case 2

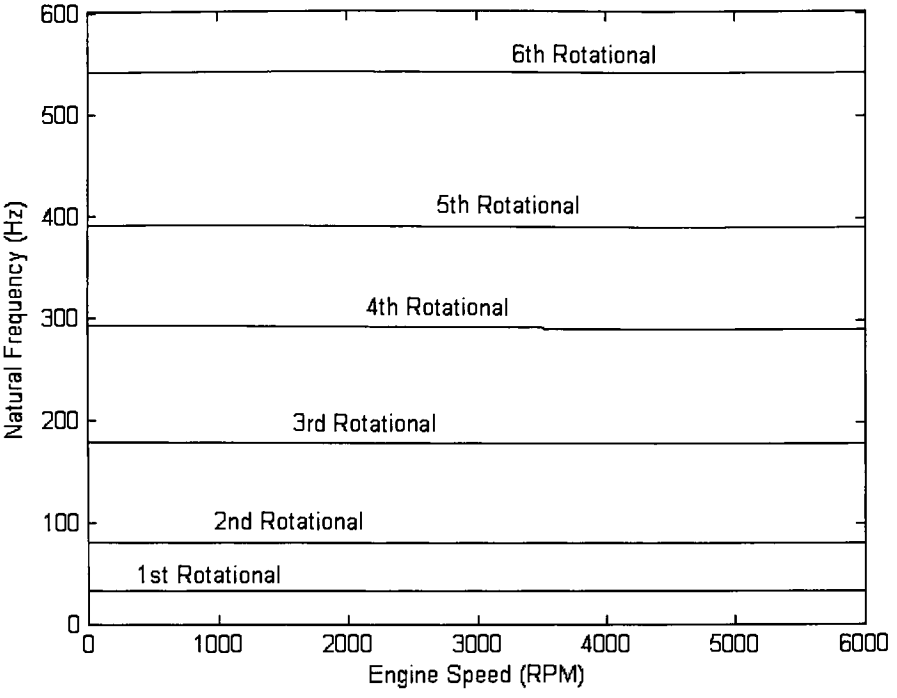

Figure 4.18 Rotational mode natural frequencies: coupled analysis, case 2

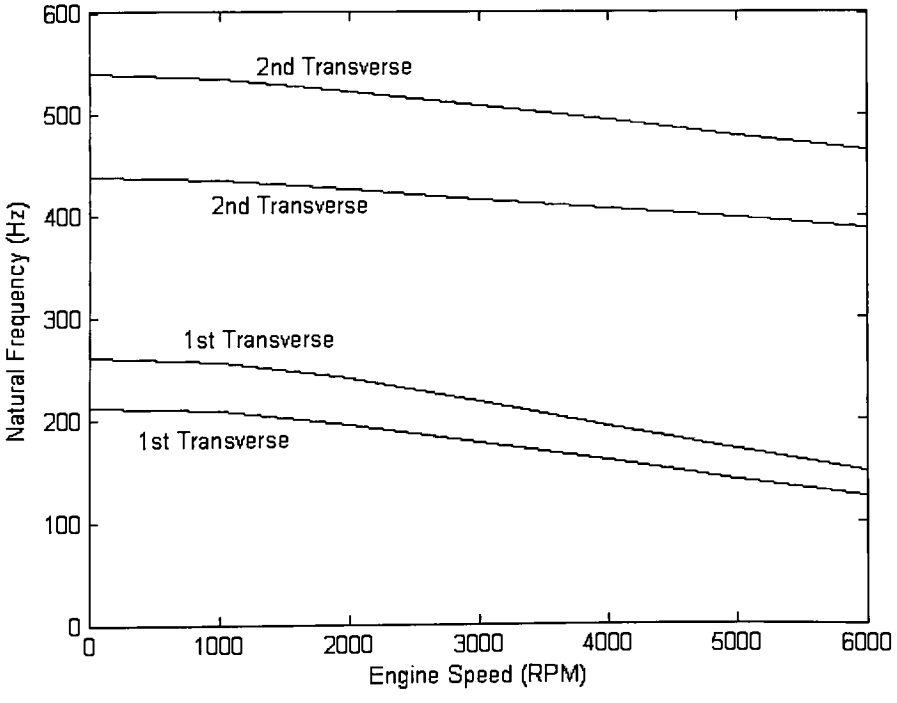

Figure 4.19 Transverse mode natural frequencies for spans adjacent to tensioner: coupled analysis, case 2

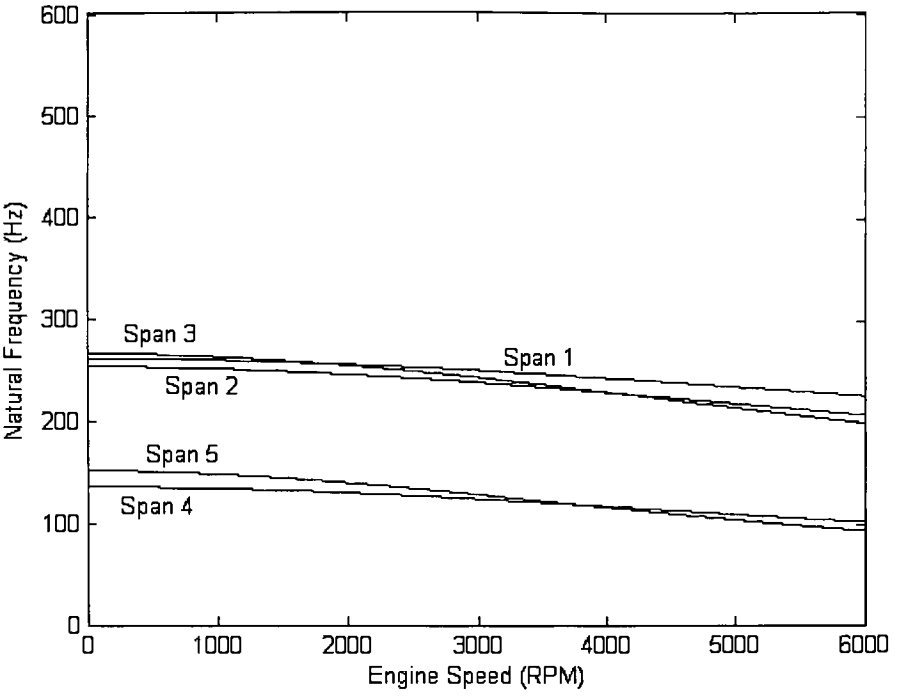

Figure 4.20 Transverse mode natural frequencies for the spans between fixed pulleys: coupled analysis, case 2

Table 4.7 Natural frequencies and mode shapes: coupled analysis, case 2, 680 rpm

CALCULATED RESULTS

Natural Frequency (Hz)	Mode
32.8	1st Rotational - Pulley 3
79.4	2nd Rotational - Pulley 6
178.7	3rd Rotational - Pulley 2
209.7	1st Transverse - Span 6
258.5	1st Transverse - Span 7
291.7	4th Rotational - Tensioner Arm
389.9	5th Rotational - Pulley 4
435.5	2nd Transverse - Span 6
536.7	2nd Transverse - Span 7
541.0	6th Rotational - Pulley 5
1355.7	7th Rotational - Pulley 7

PUBLISHED RESULTS

Natural Frequency (Hz)	Mode
32.9	1st Rotational
79.5	2nd Rotational
178.7	3rd Rotational - Pulley 2
210.0	1st Transverse - Span 6
258.9	1st Transverse - Span 7
292.0	4th Rotational
389.9	5th Rotational
420.0	2nd Transverse - Span 6
518.2	2nd Transverse - Span 7
541.0	6th Rotational

Table 4.8 Modal assurance criterion values: case 2, 680 rpm

Rotational Mode	Modal Assurance Criterion
First Coupled, First Decoupled	0.889
Second Coupled, Second Decoupled	0.309
Third Coupled, Third Decoupled	0.367
Fourth Coupled, Fourth Decoupled	0.036
Fifth Coupled, Fifth Decoupled	0.942
Sixth Coupled, Sixth Decoupled	0.847
Seventh Coupled, Seventh Decoupled	0.997
Second Coupled, Fourth Decoupled	0.586
Fourth Coupled, Second Decoupled	0.401

natural frequencies are compared between modes with similar mode shapes, the coupled rotational natural frequency of the 2nd mode should be related to the decoupled rotational natural frequency of the 4th mode and visa versa. Using this rule the rotational natural frequencies differ by more than 100% for each mode. The inconsistencies are further supported by the different dominant modes as described in Tables 4.6 and 4.7. Despite the differences in the values as determined by each of the methods, both show the same trend that indicates the rotational natural frequencies are relatively independent from engine speed.

Transverse natural frequencies of the spans adjacent to the tensioner are similar between the two methods. For the lower modes, the results are again comparable to within 1.0%. However, for the higher modes, the frequencies show the same behavior as in case study 1. At lower engine speeds, the results remain consistent between the methods. However, at higher engine speeds, natural frequencies for the 2nd modes differ by as much as 40%.

Those spans bounded by fixed pulleys are once more shown to have the same transverse natural frequencies when calculated by either the coupled and decoupled models. The results are again provided for completeness.

4.3 CASE STUDY 3 – EXPERIMENTAL

4.3.1 System Configuration

Evaluating the ability of both the coupled and decoupled solutions to accurately predict natural frequencies and mode shapes is completed by comparing the results obtained using each method to those determined through experiment. Data for an example serpentine belt drive system is presented in Table 4.9. The data is based on an experimental setup used by Beikmann [13] to validate the results of his coupled formulation. The experimental results presented in [13] will be used to complete the

Table 4.9 Dimensional specifications and load information: case 3

PULLEYS

Pulley # j	Type	X_j - Y_j Location (mm)	R_j (mm)	J_j (kg-m^2)	Q_j (N-m)
1	C/S	(552.5, 55.6)	88.9	0.07248	
2	TENS. Pulley	(347.7, 57.15)	45.2	0.000293	0
3	IDL	(0, 0)	26.97	0.000293	0

TENSIONER ARM

X_8 - Y_8 Location (mm)	θ_0 (deg)	J_t (kg-m^2)	g (m/s^2)	m_{eff} (kg)	EA (N)
(250.8, 63.5)	356.3	0.001165	0 (assumed)	0 (assumed)	170000
L_{eff} (mm)	L_t (mm)	Q_t (N-m)	C_t (N-m-s)	K_t (N-m/rad)	ρ (kg/m)
0 (assumed)	97	8.34	0	54.37	0.1029

comparison between the coupled and decoupled models. The system presented here is smaller than those in the previous case studies; however it contains all the necessary components critical to a serpentine belt drive system including a driving pulley, automatic tensioner, and a driven pulley. The simplicity of the system was necessary to reduce potential errors in the experiment. The mass of the tensioner pulley is included in J_t using the parallel axis theorem. Additional required parameters are calculated from the system geometry.

4.3.2 Decoupled Results

4.3.2.1 Equilibrium

Tractive tensions are not plotted here since tension is uniform throughout the entire belt length due to the condition that there are no accessory torque loads applied to any of the pulleys. It can be shown, as in the previous case studies, that tractive tension does not change with increasing engine speed. Equilibrium tensioner arm angle can also be shown to produce similar trends as in the previous case studies.

4.3.2.2 Natural frequencies and mode shapes

The natural frequencies are plotted in Fig. 4.21-4.23. The rotational natural frequencies remain constant with increasing engine speed. However, the transverse natural frequencies of the belt spans adjacent to the tensioner and those between fixed pulleys are highly dependent upon engine speed as seen in Fig. 4.22 and 4.23.

For zero engine speed, the natural frequencies and mode shapes are given in Table 4.10. Notice the transverse natural frequency of the fixed-fixed span is given. This is included in Table 4.10 for completeness since Beikmann includes it in the results.

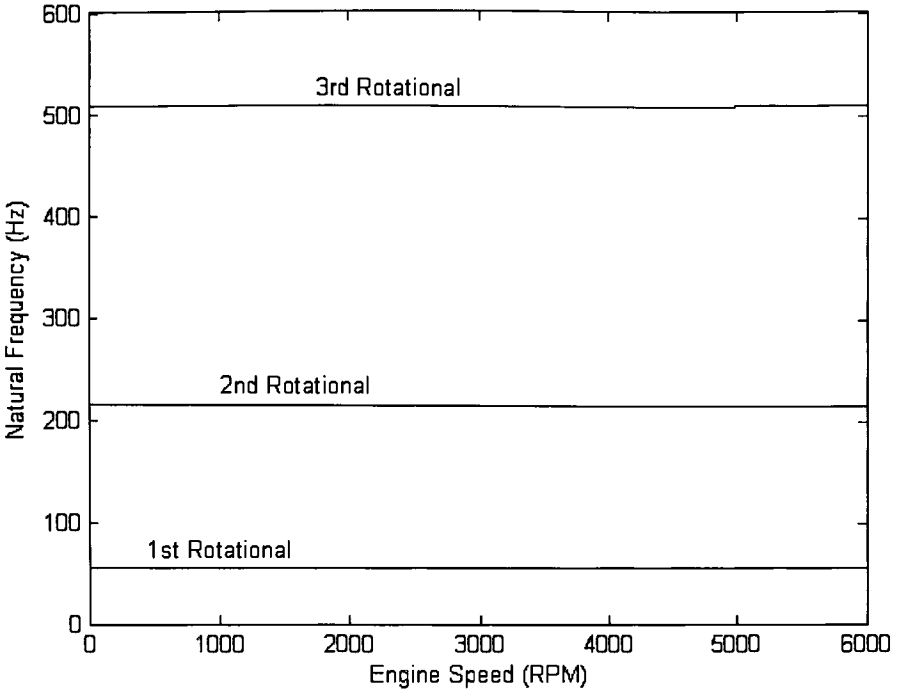

Figure 4.21 Rotational mode natural frequencies: decoupled analysis, case 3

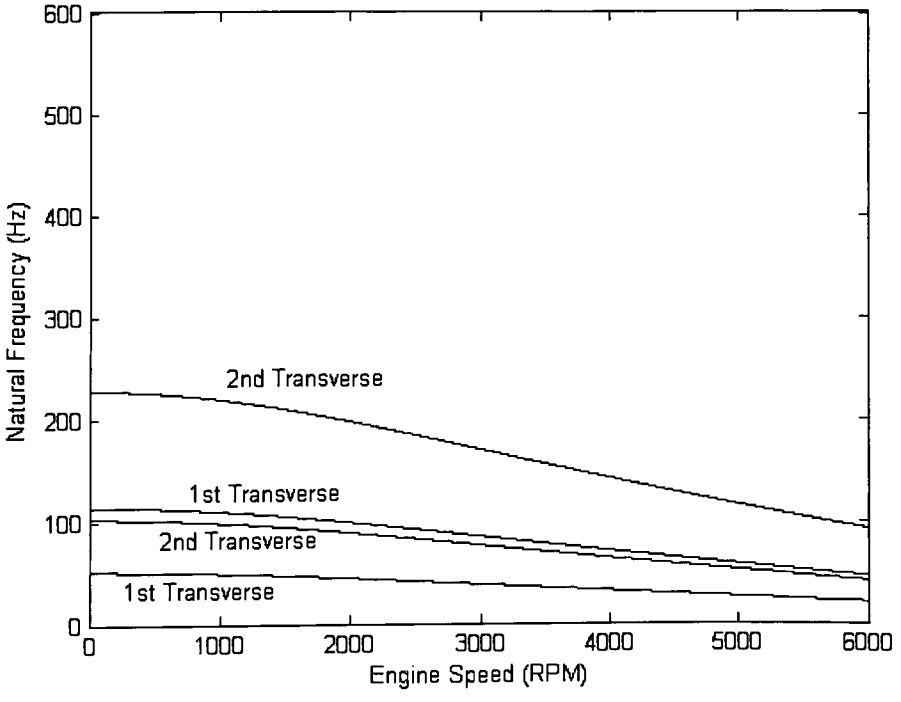

Figure 4.22 Transverse mode natural frequencies for spans adjacent to tensioner: decoupled analysis, case 3

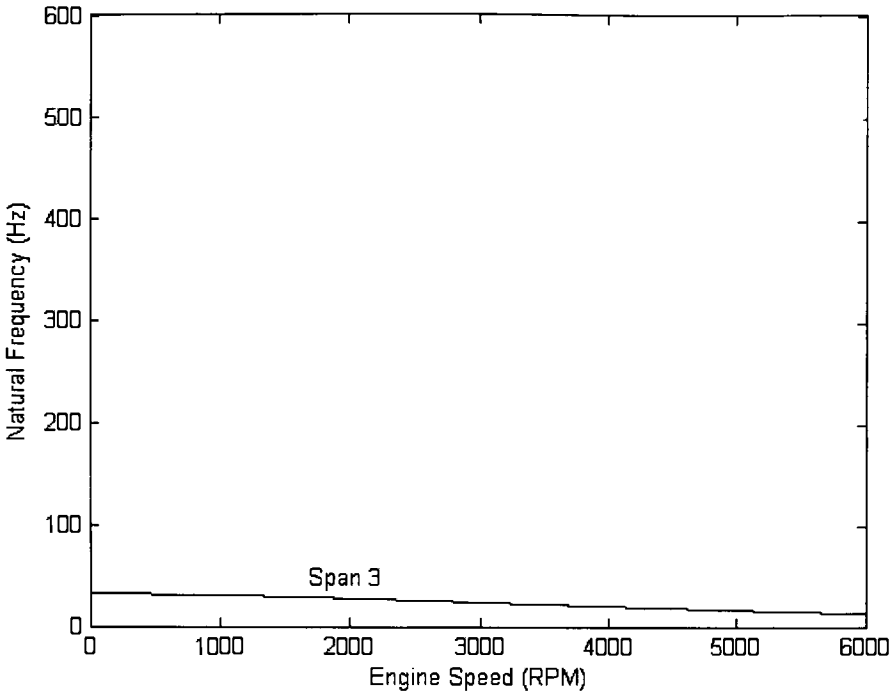

Figure 4.23 Transverse mode natural frequencies for the spans between fixed pulleys: decoupled analysis, case 3

Table 4.10 Natural frequencies and mode shapes: decoupled analysis, case 3, 0 rpm

Natural Frequency (Hz)	Mode
31.9	Transverse - Fixed-Fixed Span
51.0	1st Transverse - Span 2
55.6	1st Rotational - Pulley 3
101.9	2nd Transverse - Span 2
113.6	1st Transverse - Span 1
214.8	2nd Rotational - Pulley 3
227.1	2nd Transverse - Span 1
508.1	3rd Rotational - Pulley 2

4.3.3 Coupled Results

Results for the coupled analysis are presented in Figs. 4.24-4.26 and Table 4.11. Similar results are seen here as in the previous sections with the addition of the transverse natural frequency of the fixed-fixed span.

4.3.4 Comparison

Results presented by Beikmann [13] are compared to the findings of both the coupled and decoupled analyses completed herein. Based on this comparison, it is determined that the coupled solution provides the most accurate results. This is shown by the fact that the 1st rotational natural frequency differs from the experimental value by less than 2 percent. However, the decoupled analysis provides an estimate of the natural frequency that is more than 10 percent off the experimental value. Both analyses result in the same transverse natural frequency for span 2 adjacent to the tensioner; which deviates from the experimental value by less than 2 percent.

Analyzing the higher modes not presented by Beikmann reveals that the natural frequencies remain more consistent for this small system than for the larger systems of case studies one and two. Here, the natural frequencies differ by less than 10 percent as can be seen in Tables 4.10 and 4.11. The modal assurance criterion demonstrates that only the first mode shape is inconsistent between the two methods as shown in Table 4.12. This result is further reinforced by the experimental findings that demonstrate the same dominant motion as the coupled analysis.

Transverse natural frequencies of the spans adjacent to the tensioner are similar between the two methods. For the lower modes, the results are again comparable to within 1.0%. However, for the higher modes, the frequencies show the same behavior as in case studies 1 and 2. At lower engine speeds, the results remain consistent between the methods.

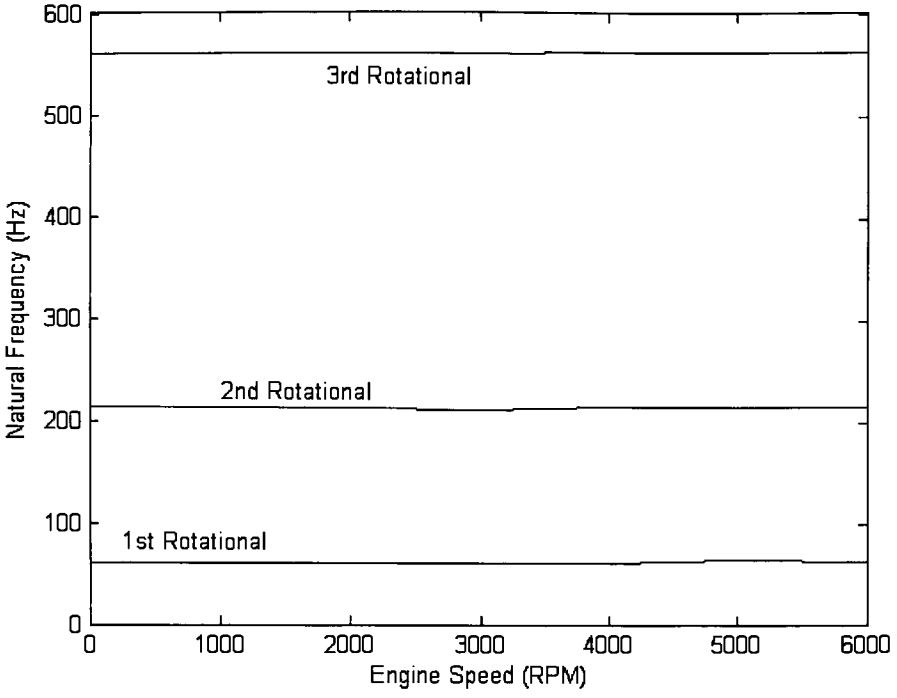

Figure 4.24 Rotational mode natural frequencies: coupled analysis, case 3

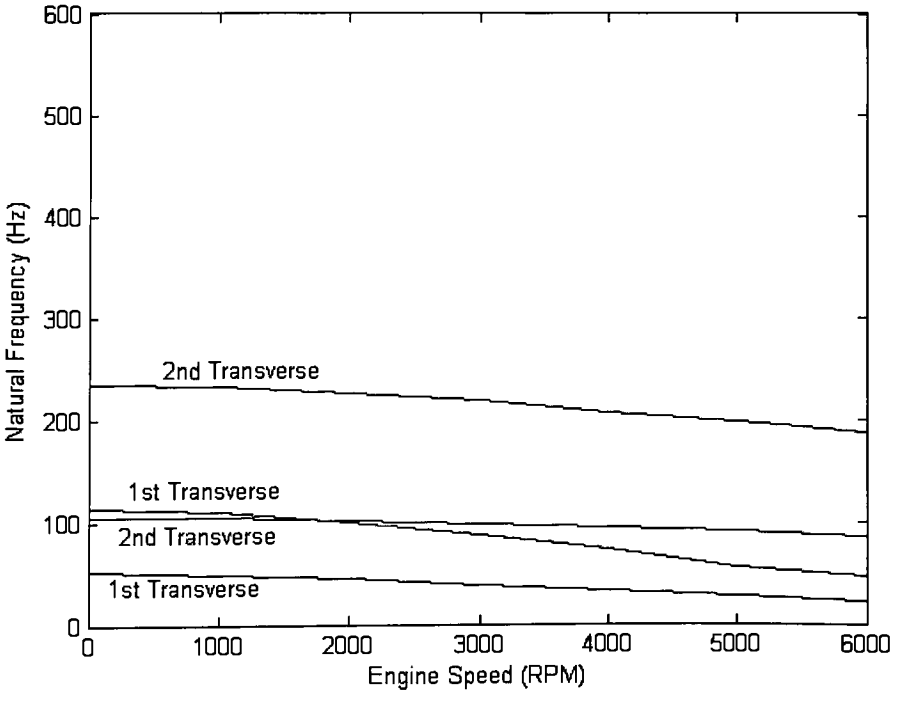

Figure 4.25 Transverse mode natural frequencies for spans adjacent to tensioner: coupled analysis, case 3

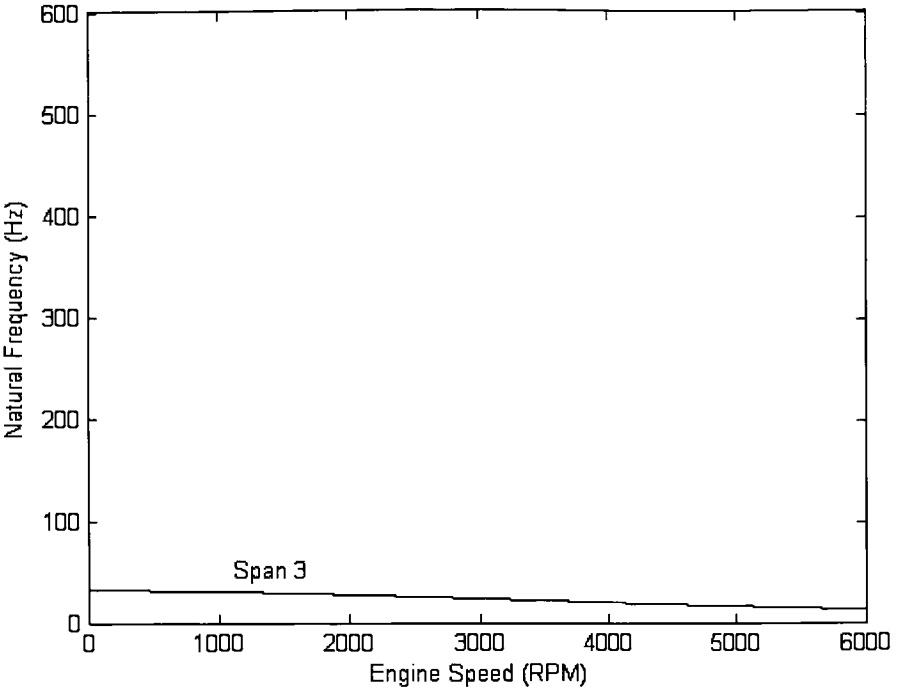

Figure 4.26 Transverse mode natural frequencies for the spans between fixed pulleys: coupled analysis, case 3

Table 4.11 Natural frequencies and mode shapes: coupled analysis, case 3, 0 rpm

CALCULATED RESULTS

Natural Frequency (Hz)	Mode
31.9	Transverse - Fixed-Fixed Span
51.0	1st Transverse - Span 2
61.3	1st Rotational - Tensioner Arm
105.0	2nd Transverse - Span 2
114.0	1st Transverse - Span 1
214.0	2nd Rotational - Pulley 3
234.8	2nd Transverse - Span 1
560.2	3rd Rotational - Pulley 2

PUBLISHED RESULTS

Natural Frequency (Hz)	Mode
33.00	Fixed-Fixed Transverse
51.75	1st Transverse - Span 2
62.50	1st Rotational - Tensioner Arm

Table 4.12 Modal assurance criterion values: case 3, 0 rpm

Rotational Mode	Modal Assurance Criterion
First Coupled, First Decoupled	0.04
Second Coupled, Second Decoupled	0.791
Third Coupled, Third Decoupled	0.939

However, at higher engine speeds, natural frequencies for the 2nd modes differ by as much as 50%.

Those spans bounded by fixed pulleys are once more shown to have the same transverse natural frequencies when calculated by both the coupled and decoupled models. The results are again provided for completeness.

CHAPTER 5

SUMMARY AND CONCLUSIONS

This chapter reviews the thesis objectives and contributions described in Chapter 1. The results presented in Chapter 4 are summarized and final conclusions about the need to couple or decouple the model are made. Finally, recommendations for future work in the area of serpentine belt drives are discussed.

5.1 PROBLEM OBJECTIVES

In the field of serpentine belt drives, it has become common for authors to couple the transverse and rotational motions of the belt due to the motion of the tensioner arm. It has been assumed that this coupling mechanism will produce more accurate results. However, as these systems become more complex, the solution of their models require greater computing power; a condition made worse by more complicated solution techniques.

The problem objective of this thesis is to determine whether it is necessary to couple the transverse and rotational motions of the belt due to the motion of the tensioner arm. Two solution techniques (one coupled and one decoupled) are applied to three case studies to determine the versatility and accuracy of each technique. A parametric study is used to determine the ability of each solution to predict system behavior based on varying system parameters.

5.2 THESIS CONTRIBUTIONS

1. The formulation presented by Hwang et al. [7] is extended to present the linearization solution technique necessary for determining the rotational natural frequencies and mode shapes of the decoupled model. Decoupled

methods for determining the transverse natural frequencies of the spans adjacent to the tensioner and those between fixed pulleys are presented.

2. The coupled model presented by Parker [22] is extended to present the entire technique for determining the steady state tensions and tensioner arm angle necessary to calculate the natural frequencies and mode shapes of the system. An decoupled model is used to determine the transverse natural frequencies of the spans bounded by fixed pulleys.
3. The accuracy of each method is examined using three case studies. Both solution techniques are applied to each case study and the natural frequency and mode shape results are compared to determine the necessity of coupling the motions.
4. The ability of each method to accurately predict changes in natural frequencies due to varying system parameters is examined through a parametric study.

5.3 PARAMETRIC STUDY

The figures referenced in Chapter 4 are plotted across a specific range of engine speed. Upon referring to those figures, it is apparent that certain characteristics of the system are affected largely by speed. The range over which the figures are plotted is chosen since it represents a normal operating range of an automotive engine.

The rotational natural frequencies are relatively unaffected by an increase in engine speed up to the 6000 rpm limit. However, the transverse natural frequencies are greatly influenced by increasing speed as evidenced by the figures. Transverse natural frequencies of the spans bounded by fixed pulleys change at the same rate for both the coupled and decoupled models since both are calculated using the same procedure. The transverse natural frequencies of the spans adjacent to the tensioner show different behavior between the two methods. At lower engine speeds, the natural frequencies of all the transverse modes are found to be closely related between the two methods to within 10 percent. However, as engine speed begins to increase, the methods produce distinctly

different results. This occurs particularly for the 2nd transverse modes. For case study 1, the natural frequencies of the 2nd transverse modes differ by 30% at 6000 rpm. Similar results are seen for case study 2 and case study 3, where the frequencies differ by 40% and 50% respectively.

5.4 CONCLUSIONS

The decoupled solution has the advantage of simplicity over the coupled solution. When the transverse motions of the belt spans adjacent to the tensioner are ignored, the process to determine the natural frequencies and mode shapes of a serpentine belt drive system is straightforward and readily programmable in any coding language.

Despite the simplicity of the decoupled solution, the results show that rotational motion is indeed coupled to the transverse motions of the spans adjacent to the tensioner. The decoupled analysis cannot predict the rotational natural frequencies with the accuracy of the coupled analysis. The variation between the results is consistently in the 15-25% range. The coupled solution is shown to produce the more accurate results based on the comparison to the experimental data.

As the number of pulleys and therefore the size of the system decrease, the variation in results between the solution techniques diminishes. As is shown by case study 3, the difference between the coupled and decoupled rotational natural frequencies is consistently less than 10%. This small error in the results is deemed acceptable as experimental results are only reliable to within 10% due to the difficulty in measuring characteristics of the system.

The coupled and decoupled solutions provide similar results for the transverse natural frequencies. The spans bounded by fixed pulleys require the same method for each model to determine the transverse natural frequencies. It follows then that both produce the same accurate results validated by the experimental data.

The spans adjacent to the tensioner are not as straightforward. For the lower modes, the results are consistent between the two methods for the entire range of belt speeds. However, the second modes begin to see increased deviation between the two solutions. For lower engine speeds a difference of 10% is acceptable; however at higher speeds, the difference grows to over 30%. This behavior is observed for both large and small systems.

From these results, it is evident that the rotational and transverse motions must be coupled to accurately predict the natural frequencies and mode shapes of a serpentine belt drive system.

5.5 RECOMMENDATIONS FOR FUTURE WORK

The analysis completed in this thesis has led to observations for future work in the field of serpentine belt drive modeling.

In the coupled analysis, a set of four basis functions were used to represent the shape of the span adjacent to the tensioner. Increasing the number of basis functions is shown by Parker [22] to result in faster convergence of the natural frequencies. However, it is unclear the effect that the shape of the basis function has on the results. To examine this, a new set of basis functions should be used to determine how the natural frequencies and modes shapes are affected.

The results presented in this thesis are validated by the experimental data provided by Beikmann [13]. However, the amount of data available is limited as only the first few modes are presented in the experimental results. Therefore, more experimental work needs to be done to detect the true behavior of serpentine belt drive systems in order to better understand how each assumption limits the accuracy of a formulation.

APPENDIX A

DERIVATION OF THE EQUATIONS OF MOTION FOR THE TENSIONER SUBSYSTEM

A model of the tensioner subsystem is shown in Fig. 2.2. This configuration is used to derive the equations of motion that describe the rotational response of the tensioner assembly. Consider a control volume enclosing the tensioner arm and pulley 7 which rotates rigidly with the tensioner arm about the pivot [7]. The governing equation for a noninertial control volume rotating about a fixed axis is [27],

$$\begin{aligned}&\vec{r}\times\vec{F}_s+\int_{CV}\vec{r}\times\vec{g}\rho d\forall+\vec{T}_{shaft}-\int_{CV}\vec{r}\times[2\vec{\omega}\times\vec{V}_{xyz}+\vec{\omega}\times(\vec{\omega}\times\vec{r})+\dot{\vec{\omega}}\times\vec{r}]\rho d\forall\\&=\frac{\partial}{\partial t}\int_{CV}\vec{r}\times\vec{V}_{xyz}\rho_p d\forall+\int_{CS}\vec{r}\times\vec{V}_{xyz}\rho_b\vec{V}_{xyz}\cdot d\vec{A}\end{aligned}\qquad(A.1)$$

where, $\forall$ is the volume, ρ_p is the pulley density, and ρ_b is the density of the belt. In this equation, the $\vec{r}$ and $\vec{V}_{xyz}$ vectors represent position and velocity measured relative to the control volume, and $\vec{\omega}$ represents the angular velocity of the entire control volume. Surface forces ($\vec{F}_s$) include the force of both spans on the surface of the control volume and $\vec{T}_{shaft}$ is the toque at the tensioner hub due to tensioner arm damping and the torque applied by the tensioner spring. Each term in equation (A.1) is evaluated for this particular system

$$\vec{r}\times\vec{F}_s=[P_6(R_7+L_t\sin\beta_1)-P_7(R_7+L_t\sin\beta_2)]\hat{k}$$

$$\int_{CV}\vec{r}\times\vec{g}\rho d\forall=-m_{eff}L_{eff}g\cos\theta_t\hat{k}$$

$$\int_{CV}\vec{r}\times[2\vec{\omega}\times\vec{V}_{xyz}+\vec{\omega}\times(\vec{\omega}\times\vec{r})+\dot{\vec{\omega}}\times\vec{r}]\rho d\forall=(J_t+J_{7t})\ddot{\theta}_t\hat{k}$$

$$\frac{\partial}{\partial t}\int_{CV}\vec{r}\times\vec{V}_{xyz}\rho_p dV = J_7\ddot{\theta}_7\hat{k}$$

$$\int_{CS}\vec{r}\times\vec{V}_{xyz}\rho_b\vec{V}_{xyz}\cdot d\vec{A} = \rho(V+R_7\dot{\theta}_7)(V+R_7\dot{\theta}_7)L_t(\sin\beta_1-\sin\beta_2)\hat{k}$$

Substitution of these terms into equation (A.1) and rearranging terms yields the equation of motion for the tensioner subsystem as presented in equation (2.9). Equation (2.8) for pulley 7 can be prepared in the same manner by constructing a control volume around pulley 7 exclusively and repeating the formulation above.

APPENDIX B

CALCULATION OF TENSIONER AFFECTED GEOMETRIES

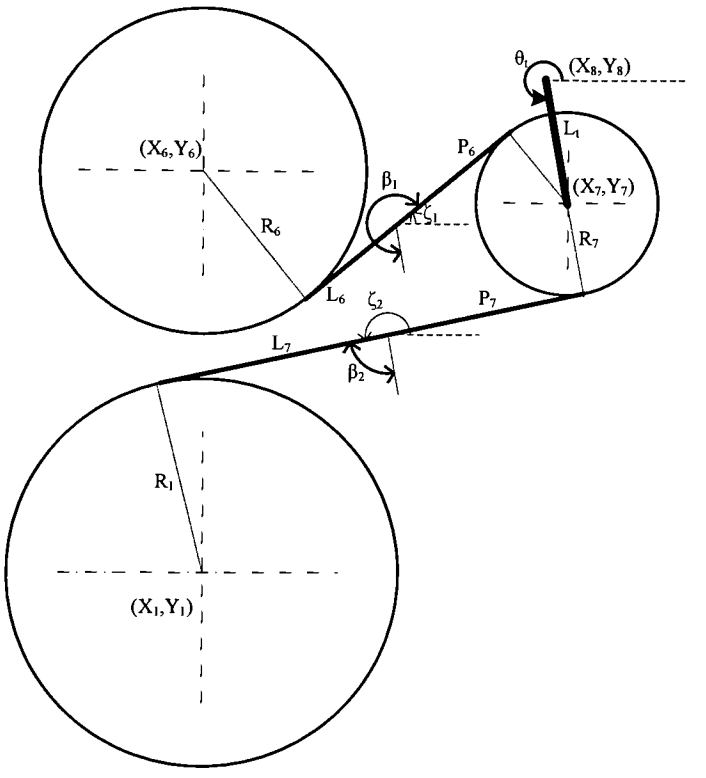

Figure 2.3 Tensioner assembly angles

By examining Fig. 2.3 it is apparent that the span lengths L_6 and L_7 as well as the orientation angles β_1 and β_2 are calculated as functions of the tensioner arm angle (θ_t). It is important to know these relationships as solution of the equations of motion of the entire system depend upon these parameters. The system geometries are related through

$$X_7 = X_8 + L_t \cos\theta_t$$

$$Y_7 = Y_8 + L_t \sin\theta_t$$

$$L_6 = \sqrt{(X_6 - X_7)^2 + (Y_6 - Y_7)^2 - (R_6 + R_7)^2}$$

$$L_7 = \sqrt{(X_7 - X_1)^2 + (Y_7 - Y_1)^2 - (R_7 + R_1)^2}$$

$$\zeta_1 = \tan^{-1}\left[\frac{R_6 + R_7}{L_6}\right] + \tan^{-1}\left[\frac{Y_6 - Y_7}{X_6 - X_7}\right]$$

$$\zeta_2 = \frac{3\pi}{2} - \tan^{-1}\left[\frac{R_7 + R_1}{L_7}\right] - \tan^{-1}\left[\frac{X_7 - X_1}{Y_7 - Y_1}\right]$$

$$\beta_1 = \theta_t - \zeta_1$$

$$\beta_2 = \theta_t - \zeta_2$$

APPENDIX C

MASS, DAMPING AND STIFFNESS MATRICES FOR THE LINEARIZED EQUATIONS OF MOTION

$$[M]=\begin{bmatrix} J_t+J_{7t} & 0 & 0 & \cdots & J_7 \\ 0 & J_2 & 0 & \cdots & 0 \\ 0 & 0 & J_3 & \cdots & 0 \\ \vdots & \vdots & \vdots & \ddots & \vdots \\ J_7 & 0 & 0 & \cdots & J_7 \end{bmatrix}$$

$$[C]=\begin{bmatrix} C_t & 0 & 0 & \cdots & L_t \sin\beta_1 \rho R_7 - L_t \sin\beta_2 \rho R_7 \\ 0 & 0 & 0 & \cdots & 0 \\ 0 & 0 & 0 & \cdots & 0 \\ \vdots & \vdots & \vdots & \ddots & \vdots \\ 0 & 0 & 0 & \cdots & 0 \end{bmatrix}$$

$$[K]=\begin{bmatrix} K_{11} & K_{12} & K_{13} & \cdots & K_{17} \\ R_2\left[\frac{\partial P_2}{\partial \theta_t}\Big|_e-\frac{\partial P_1}{\partial \theta_t}\Big|_e\right] & R_2\left[\frac{\partial P_2}{\partial \theta_2}\Big|_e-\frac{\partial P_1}{\partial \theta_2}\Big|_e\right] & R_2\left[\frac{\partial P_2}{\partial \theta_3}\Big|_e-\frac{\partial P_1}{\partial \theta_3}\Big|_e\right] & \cdots & R_2\left[\frac{\partial P_2}{\partial \theta_7}\Big|_e-\frac{\partial P_1}{\partial \theta_7}\Big|_e\right] \\ R_3\left[\frac{\partial P_3}{\partial \theta_t}\Big|_e-\frac{\partial P_2}{\partial \theta_t}\Big|_e\right] & R_3\left[\frac{\partial P_3}{\partial \theta_2}\Big|_e-\frac{\partial P_2}{\partial \theta_2}\Big|_e\right] & R_3\left[\frac{\partial P_3}{\partial \theta_3}\Big|_e-\frac{\partial P_2}{\partial \theta_3}\Big|_e\right] & \cdots & R_3\left[\frac{\partial P_3}{\partial \theta_7}\Big|_e-\frac{\partial P_2}{\partial \theta_7}\Big|_e\right] \\ \vdots & \vdots & \vdots & \ddots & \vdots \\ R_7\left[\frac{\partial P_7}{\partial \theta_t}\Big|_e-\frac{\partial P_6}{\partial \theta_t}\Big|_e\right] & R_7\left[\frac{\partial P_7}{\partial \theta_2}\Big|_e-\frac{\partial P_6}{\partial \theta_2}\Big|_e\right] & R_7\left[\frac{\partial P_7}{\partial \theta_3}\Big|_e-\frac{\partial P_6}{\partial \theta_3}\Big|_e\right] & \cdots & R_7\left[\frac{\partial P_7}{\partial \theta_7}\Big|_e-\frac{\partial P_6}{\partial \theta_7}\Big|_e\right] \end{bmatrix}$$

$$K_{11}=K_t+R_7\left[\frac{\partial P_7}{\partial \theta_t}\Big|_e-\frac{\partial P_6}{\partial \theta_t}\Big|_e\right]-L_t\sin\beta_1\left[\frac{\partial P_6}{\partial \theta_t}\Big|_e\right]+L_t\sin\beta_2\left[\frac{\partial P_7}{\partial \theta_t}\Big|_e\right]-m_{eff}L_{eff}\,g\sin\theta_t^e$$

$$K_{12}=R_7\left[\frac{\partial P_7}{\partial \theta_2}\Big|_e-\frac{\partial P_6}{\partial \theta_2}\Big|_e\right]-L_t\sin\beta_1\left[\frac{\partial P_6}{\partial \theta_2}\Big|_e\right]+L_t\sin\beta_2\left[\frac{\partial P_7}{\partial \theta_2}\Big|_e\right]$$

$$K_{13} = R_7\left[\frac{\partial P_7}{\partial \theta_3}\Big|_e - \frac{\partial P_6}{\partial \theta_3}\Big|_e\right] - L_t \sin\beta_1\left[\frac{\partial P_6}{\partial \theta_3}\Big|_e\right] + L_t \sin\beta_2\left[\frac{\partial P_7}{\partial \theta_3}\Big|_e\right]$$

$$K_{17} = R_7\left[\frac{\partial P_7}{\partial \theta_7}\Big|_e - \frac{\partial P_6}{\partial \theta_7}\Big|_e\right] - L_t \sin\beta_1\left[\frac{\partial P_6}{\partial \theta_7}\Big|_e\right] + L_t \sin\beta_2\left[\frac{\partial P_7}{\partial \theta_7}\Big|_e\right]$$

APPENDIX D

ELEMENTS OF MATRICES IN EQUATION (3.50)

$$\mathbf{G}^{t(i-1)} = l_t \cos\beta_1[\alpha_1(1), \alpha_2(1), \ldots, \alpha_f(1)]$$

$$\mathbf{G}^{t(i)} = -l_t \cos\beta_2[\gamma_1(0), \gamma_2(0), \ldots, \gamma_f(0)]$$

$$\mathbf{K}^{t(i-1)} = \left(\frac{l_t}{l_{i-1}}\right)\left(p_{i-1} - v^2\right)\cos\beta_1[\alpha_1'(1), \alpha_2'(1), \ldots, \alpha_f'(1)]$$

$$\mathbf{K}^{t(i)} = -\left(\frac{l_t}{l_i}\right)\left(p_i - v^2\right)\cos\beta_2[\gamma_1'(0), \gamma_2'(0), \ldots, \gamma_f'(0)]$$

$$K^{tt} = l_t^2\left(k_t + \frac{k_b}{l_{i-1}}\sin^2\beta_1 + \frac{k_b}{l_i}\sin^2\beta_2\right)$$

$$\mathbf{K}^{tp}(1, i-2) = l_t\left(\frac{k_b}{l_{i-1}}\right)\sin\beta_1$$

$$\mathbf{K}^{tp}(1, i-1) = -l_t\left[\left(\frac{k_b}{l_{i-1}}\right)\sin\beta_1 + \left(\frac{k_b}{l_i}\right)\sin\beta_2\right]$$

$$\mathbf{K}^{tp}(1, i) = l_t\left(\frac{k_b}{l_i}\right)\sin\beta_2$$

All other elements in $\mathbf{K}^{tp}$ are zero and $\mathbf{K}^{pt} = transpose\left(\mathbf{K}^{tp}\right)$.

$$\mathbf{K}^{pulley}(m,m-1)=-\frac{k_b}{l_m}$$

$$\mathbf{K}^{pulley}(m,m)=\frac{k_b}{l_m}+\frac{k_b}{l_{m+1}}$$

$$\mathbf{K}^{pulley}(m,m+1)=-\frac{k_b}{l_{m+1}}$$

where $m=1,2,\ldots,n-1$. All other elements in $\mathbf{K}^{pulley}$ are zero.

APPENDIX E

MODAL ASSURANCE CRITERION

As a technique for quantifying the comparison between similar mode shapes of different origin (either predicted or experimental), the modal assurance criterion (MAC) provides a measure of the least squares deviation of the points from the straight line correlation [26]. This is determined by:

$$MAC = \frac{\left[\{\phi\}_1^T \{\phi\}_2\right]^2}{\{\phi\}_1^T \{\phi\}_1 \times \{\phi\}_2^T \{\phi\}_2}$$

where $\{\phi\}$ is the mode shape. The subscripts 1 and 2 signify mode shapes determined by either method 1 or method 2 respectively. The MAC will be a scalar quantity whether or not the mode shapes are complex, and the degree of correlation is signified by a value between 0 and 1. A value closer to 1 indicates similar mode shape while a value closer to 0 indicates dissimilar mode shapes. There is no strict value which MAC should take in order to guarantee good results, but it is generally accepted that a value above 0.9 indicates correlated modes, and a value below 0.05 signifies uncorrelated modes.

REFERENCES

1. Mote, C.D. Jr. "A Study of Band Saw Vibrations." Journal of The Franklin Institute 279 (1965): 430-444.
2. Wickert, J.A., Mote, C.D. Jr. "Classical Vibration Analysis of Axially Moving Continua." ASME Journal of Applied Mechanics 57 (1990): 738-744.
3. Ulsoy, A.G., Whitesell, J.E., Hooven, M.D. "Design of Belt-Tensioner Systems for Dynamic Stability." ASME Journal of Vibration, Acoustics, Stress, and Reliability in Design (1985): 1-9.
4. Gasper, R.G.S., Hawker, L.E. "Resonance Frequency Prediction of Automotive Serpentine Belt Drive Systems by Computer Modeling." Machinery Dynamics - Applications and Vibration Control Problems, September 17-21 ASME, 1989. 13-16.
5. Hawker, Larry E. A Vibration Analysis of Automotive Serpentine Accessory Drive Systems. Diss. University of Windsor, 1991. Windsor.
6. Barker, C.R., Oliver, L.R., Breig, W.F. "Dynamic Analysis of Belt Drive Tension Forces During Rapid Engine Acceleration." International Congress and Exposition, February 25-March 1 SAE, 1991.
7. Hwang, S.J., Perkins, N.C., Ulsoy, A.G., Meckstroth, R.J. "Rotational Response and Slip Prediction of Serpentine Belt Drive Systems." ASME Journal of Vibration and Acoustics 116 (1994): 71-78.
8. Kraver, T.C., Fan, G.W., Shah, J.J. "Complex Modal Analysis of a Flat Belt Pulley System With Belt Damping and Coulomb-Damped Tensioner." ASME Journal of Mechanical Design 118 (1996): 306-311.
9. Leamy, M.J., Perkins, N.C. "Nonlinear Periodic Response of Engine Accessory Drives With Dry Friction Tensioners." ASME Journal of Vibration and Acoustics 120 (1998): 909-916.
10. Balaji, R., Mockensturm, E.M. "Dynamic Analysis of a Serpentine Belt Drive With a Decoupler/Isolator." ASME International Mechanical Engineering Congress and Exposition, November 13-20 ASME, 2004. 291-303.

11. Schulz, M. "Elastic Creep in Serpentine Belt Drives and Adopting a Suitable Strain Measure." Proceedings of the Institute of Mechanical Engineers: Journal of Mechanical Engineering Science 218 (2004): 1421-1433.
12. Nouri, M., Zu, J.W. "Dynamic Analysis and Optimization of Tensioner in Automotive Serpentine Belt Drive Systems." ASME Design Engineering Technical conferences and Computer and Information in Engineering Conference, September 29-October 2 ASME, 2002. 813-820.
13. Beikmann, R.S. Static and Dynamic Behavior of Serpentine Belt Drive Systems: Theory and Experiment Diss. University of Michigan, 1992. Michigan.
14. Beikmann, R.S., Perkins, N.C., Ulsoy, A.G. "Free Vibration of Serpentine Belt Drive Systems." ASME Journal of Vibration and Acoustics 118 (1996): 406-413.
15. Beikmann, R.S., Perkins, N.C., Ulsoy, A.G. "Nonlinear Coupled Vibration Response of Serpentine Belt Drive Systems." ASME Journal of Vibration and Acoustics 118 (1996): 567-574.
16. Beikmann, R.S., Perkins, N.C., Ulsoy, A.G. "Design and Analysis of Automotive Serpentine Belt Drive Systems for Steady State Performance." ASME Journal of Mechanical Design 119 (1997): 162-168.
17. Zhang, L., Zu, J.W. "Modal Analysis of Serpentine Belt Drive Systems." Journal of Sound and Vibration 222 (1999): 259-279.
18. Zhang, L., Zu, J.W. "One-To-One Auto-Parametric Resonance in Serpentine Belt Drive Systems." Journal of Sound and Vibration 232 (2000): 783-806.
19. Wasfy, T.M., Leamy, M. "Effect of Bending Stiffness on the Dynamic and Steady-State Responses of Belt Drives." ASME Design Engineering Technical Conferences and Computer and Information in Engineering Conference ASME, 2002. 217-224.
20. Kong, L., Parker, R.G. "Coupled Belt-Pulley Vibration in Serpentine Drives with Belt Bending Stiffness." ASME Journal of Applied Mechanics 71 (2004): 109-119.

21. Kong, L., Parker, R.G. "Equilibrium and Belt-Pulley Vibration Coupling in Serpentine Belt Drives." ASME Journal of Applied Mechanics 70 (2003): 739-750.

22. Parker, R.G. "Efficient Eigensolution, Dynamic Response, and Eigensensitivity of Serpentine Belt Drives." Journal of Sound and Vibration 270 (2004): 15-38.

23. Abrate, S. "Vibrations of Belts and Belt Drives." Mechanism and Machine Theory 27 (1992): 645-659.

24. Beikmann, R.S., Perkins, N.C., Ulsoy, A.G. "Equilibrium Analysis of Automotive Serpentine Belt Drive Systems Under Steady Operating Conditions." The 22nd Midwestern Mechanics Conference 1991. 533-534.

25. Torok, J.S. "Formulation of Problems With Constraints in Lagrangian Dynamics." Pan American Conference of Applied Mechanics V 1997.

26. Ewins, D.J. Modal Testing: Theory and Practice. England: Research Studies Press Ltd., 1986.

27. Fox, R.W., McDonald, A.T. Introduction to Fluid Mechanics, Fifth Ed. New York: John Wiley & Sons, Inc., 1998.